Nanostructure Confinement of Ammonia Borane within Porous Silica and Carbon for Hydrogen Storage

Thesis submitted by

Tao Lu

In December 2010

For the degree of Doctor of Philosophy

In the School of Engineering and Physical Sciences

James Cook University

Contents

STATEMENT OF SOURCES

DECLARATION

I declare that this thesis is my own work and has not been submitted in any form for another degree or diploma at any university or other institution of tertiary education. Information derived from the published or unpublished work of others has been acknowledged in the text and a list of references is given.

8-12-2010

_____ _____

Signature Date

STATEMENT OF ACCESS

I, the undersigned, author of this work, understand that James Cook University will make this thesis available for use within the University Library and, via the Australian Digital Theses network, for use elsewhere.

I understand that, as an unpublished work, a thesis has significant protection under the Copyright Act and;

I do not wish to place any further restriction on access to this work. √

Or

I wish this work to be embargoed until:

Or

I wish the following restrictions to be placed on this work:

8-12-2010

_____ _____

Signature Date

Acknowledgments

I would like to express my appreciation to all those who helped me during my PhD study and the writing of my thesis.

First of all, I owe my deepest gratitude to my supervisors, Professor Yinghe He and Doctor Xiangdong Yao. Professor Yinghe is a respectable, responsible scholar, who has provided me with constant encouragement and valuable guidance in every stage of preparation of the thesis. He has spent a lot of time reading through each draft and provided me with insightful advice. Without his expert instruction, impressive kindness and patience, I could not have completed my thesis. Doctor Xiangdong who led me into the world of hydrogen storage, has offered me valuable suggestions in the academic studies. His keen and vigorous academic observation enlightens me not only in this thesis but also in my future work.

High tribute shall be paid to my research student monitor A/Prof. Siva Sivakugan, A/Prof Mohan Jacob, and Dr. Madoc Sheehan for their kindness and help. I shall extend my thanks to Ms Ruilan Liu, Ms Jihong Li, and A/Prof. Zhongxiao Peng for their support and encouragement. I am also deeply indebted to all the other staff in our school for their direct and indirect help to me.

Special thanks should go to my friends who have put considerable time and effort into their comments and assistance in helping me work out my problems.

Thanks to Professor Max Lu and the Australia Research Council for providing funding for this project.

Finally, I dedicate my thesis to my beloved family. My husband has always been helping me out of difficulties and supporting without a word of complaint. I owe my sincere gratitude to my family who gave me their loving considerations and great confidence in me all through these years.

Abstract

The development of hydrogen storage systems remains a grand technical challenge. The key issue is to find and synthesize materials with required physicochemical properties for hydrogen storage. Ammonia borane (AB) is considered to be one of the most promising candidates for a chemical method as it contains remarkable hydrogen content and is stable under normal storage conditions. This thesis focuses on synthesizing porous silica and carbon as nanoporous scaffolds for encapsulating AB and investigating the thermal decomposition performance of AB in the scaffolds with tunable pore structures and compositions.

A systematical investigation has been carried out on the influence of trifluoroacetic acid, acetic acid and their salts on the synthesis of helical mesoporous materials in the presence of a cationic surfactant cetyltrimethylammonium bromide (CTAB) as a template. Results show that helical mesostructures can be successfully synthesized when CF_3COO^- anions were used as additives with an additive/CATB molar ratio (R) range of 0.1-0.375 for the CF_3COOH/CTAB templating system and a relatively wider R range of 0.1-0.5 for the CF_3COONa/CTAB templating system. Our synthesis strategy can be used for the fabrication of helical mesostructured porous materials with adjustable pore and helical pitch sizes.

The influence of the time of 1,3,5-trimethylbenzene (TMB) addition on the self-assembled organic/inorganic composite structures in a nonionic block copolymer templating system has been investigated. By controlling the time at which TMB is added to the system, an evolution from multilamellar vesicle to ordered hexagonal mesostructure has been observed, providing a simple and novel approach for the synthesis of self-assembled porous silica materials with adjustable structures and tunable pore sizes.

In the development of porous carbon materials, a sol-gel polymerization induced colloid aggregation method is adopted with the use of a commercial polymeric melamine formaldehyde resin as nitrogen doped carbon precursor. The results show that the microstructure of porous carbon materials can be adjusted by polymerization of precursors and interposition of silica particles as a hard template. Moreover, the nitrogen content and functionality make the surface properties of the porous carbon unique and different from pure carbon materials. The presence of appropriate nitrogen functionalities can improve their behaviours and extend the application of porous carbon materials, such as electrode materials for double layer capacitors and catalytic materials for proton exchange membrane fuel cells.

The thermal decomposition behaviour of AB confined in nanoporous scaffolds with controlled pore structures and wall compositions is investigated. The nanoporous scaffolds tested include Silica-1 with a helical structure and a pore diameter of 1.8

nm, Silica-2 with a vesicular structure and a pore diameter of 18 nm, as well as a macroporous N-doped carbon sample synthesized using 250 nm silica particles as a hard template. It is shown that in the case of Silica-1 with a small pore diameter of 1.8 nm, AB cannot be efficiently impregnated into the nanopores and the thermal decomposition of AB is associated with the formation of volatile by-products. For Silica-2 with a large pore diameter of 18 nm, it is a relatively better candidate compared to small pore Silica-1 because the formation of most by-products is suppressed and the first hydrogen desorption peak is lowered by 13 °C compared to neat AB. However, a small amount of released ammonia is still observed. In the case of the macroporous N-doped carbon material, the total amount of hydrogen released is 6 wt%, while the formation of both ammonia and borazine are suppressed. More importantly, the first release peak of hydrogen is 90 °C, about 20 °C lower than that of neat AB, which is better than a pure carbon material CMK-3 and equivalent to a Li-CMK-3 material reported in the literature. Our results have shown that in addition to the influence of pore size, the composition of the host material is another important factor. It is anticipated that highly porous N-doped carbon materials with further optimized pore parameters will be ideal candidates for AB immobilization and hydrogen storage.

Publications

1 Tao Lu, Xiangdong Yao, Max Gao Qing Lu, and Yinghe He. Roles of trifluoroacetic acid, acetic acid and their salts in the synthesis of helical mesoporous materials. *Journal of Porous Materials* **17** (1), 123 (2010).

2 Tao Lu, Xiangdong Yao, Gao Qing Max Qing Max Lu, and Yinghe He. Controlled evolution from multilamellar vesicles to hexagonal mesostructures through the addition of 1,3,5-trimethylbenzene. *J Colloid Interface Sci* **336** (1), 368 (2009).

List of figures and tables

Chapter 2

Chapter 4

Chapter 5

Chapter 6

List of abbreviations and chemicals

Abbreviation	Name
XRD	X-ray diffraction
TEM	transmission electron microscopy
SEM	scanning electron microscopy
XPS	X-ray photoelectron spectroscopy
TG	thermogravimetric analysis
MS	mass spectrometry
p6m	2-D hexagonal plane group
BJH model	Barrett-Joyner-Halenda model
MCFs	mesostructured cellular foams

Abbreviation	Formula	Name
AB	NH_3BH_3	Ammonia borane
	NH_3	ammonia
	$N_3H_3B_3H_3$	borazine
	CF_3COOH	Trifluoroacetic Acid
	CH_3COOH	Acetic Acid
	CF_3COONa	Sodium Trifluoroacetate
	CH_3COONa	Sodium Acetate
CTAB	$C_{19}H_{42}N.Br$	cetyltrimethylammonium bromide
TEOS	$C_8H_2O_4Si$	tetraethyl orthosilicate
TMB	C_9H_{12}	1,3,5-trimethylbenzene
	CH_3OH	methanol
Pluronic P123	$(C_3H_6O.C_2H_4O)x$ $EO_{20}PO_{70}EO_{20}$	Poly(ethylene glycol) - B - Poly(propylene glycol) - B - Poly(ethylene glycol)
	HF	hydrofluoric acid
	$C_3H_6N_6$	melamine
	CH_2O	formaldehyde
MF		melamine-formaldehyde resin
PFOA	$C_8HF_{15}O_2$	perfluorooctanoic acid
Pluronic F127	$(C_3H_6O.C_2H_4O)x$ $EO_{106}PO_{70}EO_{106}$	Poly(ethylene glycol) - B - Poly(propylene glycol) - B - Poly(ethylene glycol)
	NaOH	sodium hydroxide
	KCl	potassium chloride
	HCl	hydrochloric acid

Chapter 1 Introduction

1.1 Background

Beyond dispute the rapid depletion of fossil fuel resources and environmental pollutions associated with their use have demanded for increased attention worldwide to the possibilities of a long-term solution for a secure energy future based on potentially renewable resources. Hydrogen, the most abundant element on Earth, has been considered to be one of the ideal alternative energy sources because it is clean, non-polluting, and natural.

Hydrogen can be produced in several ways. (1) Currently, the main method to produce hydrogen is decomposition of hydrocarbons. Very recently, great efforts have been devoted to produce hydrogen by water electrolysis using sunlight in combination with photovoltaic cells. (2) The chemical energy per mass of hydrogen is 142 MJ/kg, about three times higher than that of liquid hydrocarbons (petrol is 47 MJ/kg). (1) Furthermore, when hydrogen reacts with oxygen to produce energy, the only product is water.

Today, it is commonly regarded that the physical and chemical advantages of hydrogen will make it an important synthetic fuel in the future.(1) At the current stage, however, a major concern is the safe and efficient storage and transport of this highly flammable gas. Hydrogen is a molecular gas. At room temperature and

atmospheric pressure, 4 kg of hydrogen occupies a volume of 45 m^3. This corresponds to a balloon of 5 m in diameter. This is hardly practical for any mobile application. Therefore, hydrogen storage technology is one of the key issues to be overcome in hydrogen utilizations.

The Department of Energy (DOE) of the United States has set capacity benchmark levels of above 6.0 wt% by the year 2010 and a target of 9.0 wt% by the year 2015 under moderate pressure and temperature for an onboard hydrogen storage system.(3) These benchmarks have been proposed on the basis that onboard hydrogen systems of equal weight and volume to the current fuel tanks of a conventional passenger car may drive about 400-500 km before refilling. Moreover, the onboard hydrogen storage system needs to operate at an acceptable working efficiency and condition. Thus it is very important to explore new materials and technologies to overcome the current limitations and meet the DOE requirements for the future "hydrogen economy".

Hydrogen can be stored with or without a carrier medium. Various kinds of hydrogen storage materials and technologies have been developed such as high pressure cylinder, liquid hydrogen, and storage in solid media (metal hydrides, complex hydrides, inorganic and organic matters and materials with large surface area). Among them, storage in solid media proves to be the only feasible candidate to meet the benchmark requirements for mobile applications.

Some of the greatest challenges facing hydrogen storage are the discovery of suitable materials with required material properties and development of the materials into a new onboard system. A good storage system should exhibit: 1) high volumetric/gravimetric capacity, 2) fast sorption and desorption kinetics at ambient temperatures, and 3) high tolerance to recycling.(4) Recent investigations have shown that nanoscale materials may offer some advantages in hydrogen storage if certain physical and chemical effects related to nanoscale can be used efficiently.(5-9) Surface interactions, defects, phase transformations, abundance of grain boundary, and the formation of new and metastable phases also play important roles in improving hydrogen storage properties.

It is generally considered that two basic mechanisms principally control hydrogen storage in solid materials. One mechanism is physisorption of molecular hydrogen in materials, in particular nanoscale materials due to their very high specific surface areas. The other is chemisorption, consisting of dissociation of hydrogen molecules and chemical bonding of the hydrogen atoms with the host material atoms.

Chemisorption may provide high volumetric and gravimetric storage capacities through formation of hydrides, for example, metal hydrides. However, energy is always required to split or recombine the hydrogen molecules and form or break the chemical bonds between the host material and hydrogen atoms. This is a process that inherently involves large enthalpy changes, which poses some technical challenges in

its practical applications, such as high temperature of adsorption and desorption and large energy required for releasing hydrogen. In contrast, storing hydrogen by physisorption is not subject to this constraint because the hydrogen stays in its molecular form. The problem, however, is to find light materials with a sufficient amount of surface to adsorb hydrogen. Therefore, porous solids with large surface areas have received much attention as physisorption candidates.

Recent literature has shown that there are several broad classes of solid hydrogen storage materials that are currently being investigated as potential onboard storage materials. These include: 1) metal materials, hydrides such as MgH_2, (10) imides such as $LiNH_2$, (11) and organic frameworks such as Zn_4O(1,4-benezenedicarboxylate); (12) 2) complex hydrides such as $NaAlH_4$; (1) and 3) carbon materials such as carbon nanofibers, (13) single-wall carbon nanotubes (14). To date, few of these materials meet the long term gravimetric requirements and provide rapid hydrogen release at practically acceptable temperatures. Thus, new materials and novel approaches are needed.

Chemical hydrogen storage materials that release H_2 by thermolysis without generating CO_2 offers an attractive alternative to other systems studied. One material that has attracted much attention is ammonia borane, NH_3BH_3, also known in the community as AB or borazane. AB is a colorless, crystalline solid with a melting point in the range of 110-114°C. It is stable at room temperature and soluble in

relatively polar coordinating solvents. (15) The combination of low molecular weight (30.7 $gmol^{-1}$) and high gravimetric hydrogen capacity (19.6 wt%) of AB has made it a particularly attractive candidate for H_2 storage.

AB is a remarkable molecule that contains both hydridic B–H and protic N–H bonds and a strong B–N bond that under most conditions hydrogen loss is favored over dissociation to ammonia and borane. It releases hydrogen gas when heated, but the reaction rates and products formed depend strongly on the reaction conditions. (16-19) In order for AB to become a practical candidate for on board hydrogen storage, the system has to be able to release most of the available hydrogen at an appropriate dehydrogenation rate; produce minimum amount volatile by-products (trace borazine and ammonia).

Much research works have focused on solving these problems. Nanostructured materials may offer a solution because they often exhibit significantly different physical, chemical, and thermodynamic characteristics from their bulk counterparts. Confining hydrides inside nanoporous scaffolds has been demonstrated to be an effective approach to tune the hydrogen storage properties. In nanoscale materials, shorter diffusion distances can result in faster kinetics. In addition, changes in surface energies with decreasing particle size can change the thermodynamic stability of the reactants and alter the hydrogen release mechanisms.

Experimental results on nanoscale AB systems, such as AB/SBA-15, (20) AB/carbon cryogel, (21) and AB/CMK-3, (22) have clearly demonstrated improvements in the reaction kinetics and/or thermodynamics of hydrogenation or dehydrogenation. Moreover, the modified thermodynamics of the system by nanostructure confinement effect may benefit the reversibility of AB.

However, it is noteworthy that ammonia and borazine was observed from decomposition process for AB/CMK-3 system. This is clearly detrimental and needs to be prevented for the target applications.

In order to take the advantages of AB in practical H_2 storage applications and prevent the formation of unnecessary byproducts, it is important to find optimized porous materials that can be used to confine AB and improve their hydrogen release performance. This can be achieved by a fundamental understanding of the correlation between structural parameters of porous materials and the thermal decomposition behavior of AB confined in porous materials as absorbents. However, till now little has been done to systematically study the influence of pore size and composition of porous materials on the hydrogen release behavior of AB.

1.2 Objectives

The focus of this thesis is controllably synthesize and assemble of nanoporous materials as new candidates for hydrogen storage by confining ammonia borane in

porous silica and carbon materials with different pore size, composition, and nanostructure framework, through which the influence of pore size, wall composition on hydrogen release performance can be understood. Previously, the reports of hydrogen release from AB by a nanoconfinement effect were case-study and generally one material was chosen in one literature. To date, there has been little report on the systematic study and comparison of AB/nanostructure when the structure parameters are systematically investigated.

The objectives of this thesis are:

1. The controlled synthesis of porous silica and carbon materials as nano-scaffolds for AB loading with adjustable structures, morphologies, compositions and pore sizes.

2. The study of the influence of porous structural parameters on the hydrogen release behaviour of AB confined in the nanoporous scaffolds, especially the influence of pore diameters and the wall composition.

It is desirable to understand the correlation between the structure parameters of nano-scaffolds and the hydrogen release performance of AB confined in the nano-scaffolds from this study, through which an optimized nanoporous material can be designed in the future to achieve the DOE target.

1.3 Content of thesis

Chapter 2 reviews the relevant literatures on hydrogen storage. Existing methods and materials involved in hydrogen storage systems and recent progresses are examined in this chapter.

In the next three chapters, nanoporous materials with both silica and N-doped carbon compositions, tunable pore sizes (2 - 18 nm) and controlled morphologies have been synthesized and carefully characterized.

Chapter 3 reports the synthesis of small pore size helical mesoporous silica materials through the addition of perfluorinated molecules to tetraethyl orthosilicate in the presence of a cationic surfactant cetyltrimethylammonium bromide (CTAB) as a template MCM-41 system. Trifluoroacetic acid, which has the shortest fluorocarbon chain among all perfluorocarboxylic acid molecules, acetic acid, and their salts are chosen as additives with different additive/CTAB molar ratios. This part of the work has been published in Journal of Porous Materials (23).

In Chapter 4, the synthesis of large pore size silica materials with desired structures and pore diameters through the addition of organic cosolvent 1,3,5-trimethylbenzene (TMB) in a nonionic block copolymer templating SBA-15 system examined. The effect of time of TMB addition into the synthesis system after the formation of

embryonic SBA-15 mesostructure was systematically investigated. This part of work has been published in the Journal of Colloid and Interface Science (24).

Chapter 5 presents results on the synthesis of spherical silica materials with uniform particle size according to Stöber method, which is by means of hydrolysis of alkyl silicates and subsequent condensation of silicic acid in alcoholic solutions. These monodispersed silica particles with uniform shape and size can be used as a template to develop porous carbon materials. It also discusses the synthesis of a new type of porous carbon materials, featuring nitrogen surface chemistry, via a sol-gel polymerization induced colloid aggregation method using cheap commercial polymeric melamine formaldehyde resin as nitrogen doped carbon precursors.

In chapter 6, the thermal decomposition behaviour of AB confined in nanoporous scaffolds with controlled pore structures and wall compositions is investigated. The nanoporous scaffolds were tested including Silica-1 with a helical structure and a pore diameter of 1.8 nm, Silica-2 with a vesicular structure and a pore diameter of 18 nm, as well as a macroporous N-doped carbon sample synthesized using 250 nm silica particles as hard template. The correlation between the hydrogen release performance and the pore size, composition of the nano-scaffolds has been discussed and compared with literature.

Conclusions and recommendations for further study are presented in chapter 7.

References

1 L. Schlapbach and A. Zuttel, *Nature* **414** (6861), 353 (2001).

2 M. Grätzel, *Nature* **414** (6861), 338 (2001).

3 C. Liu and H. M. Cheng, *Journal Of Physics D-Applied Physics* **38** (14), R231 (2005).

4 A. M. Seayad and D. M. Antonelli, *Advanced Materials* **16** (9-10), 765 (2004).

5 X. He and D. Antonelli, *Angewandte Chemie-International Edition* **41** (2), 214 (2001).

6 H. Gleiter, *Scripta Materialia* **44** (8-9), 1161 (2001).

7 J. D. Aiken and R. G. Finke, *Journal Of Molecular Catalysis A-Chemical* **145** (1-2), 1 (1999).

8 A. S. Arico, P. Bruce, B. Scrosati, J. M. Tarascon, and W. Van Schalkwijk, *Nature Materials* **4** (5), 366 (2005).

9 L. Zhou, *Renewable & Sustainable Energy Reviews* **9** (4), 395 (2005).

10 J. Huot, J. F. Pelletier, G. Liang, M. Sutton, and R. Schulz, *Journal Of Alloys And Compounds* **330**, 727 (2002).

11 P. Chen, Z. T. Xiong, J. Z. Luo, J. Y. Lin, and K. L. Tan, *Nature* **420** (6913), 302 (2002).

12 N. L. Rosi, J. Eckert, M. Eddaoudi, D. T. Vodak, J. Kim, M. O'Keeffe, and O. M. Yaghi, *Science* **300** (5622), 1127 (2003).

13 D. J. Browning, M. L. Gerrard, J. B. Lakeman, I. M. Mellor, R. J. Mortimer, and M. C. Turpin, *Nano Letters* **2** (3), 201 (2002).

14 A. C. Dillon, K. M. Jones, T. A. Bekkedahl, C. H. Kiang, D. S. Bethune, and M. J. Heben, *Nature* **386** (6623), 377 (1997).

15 F. Baitalow, J. Baumann, G. Wolf, K. Jaenicke-Rossler, and G. Leitner, *Thermochimica Acta* **391** (1-2), 159 (2002).

16 M. G. Hu, R. A. Geanangel, and W. W. Wendlandt, *Thermochimica Acta* **23** (2), 249 (1978).

17 J. Baumann, E. Baitalow, and G. Wolf, *Thermochimica Acta* **430** (1-2), 9 (2005).

18 A. C. Stowe, W. J. Shaw, J. C. Linehan, B. Schmid, and T. Autrey, *Physical Chemistry Chemical Physics* **9** (15), 1831 (2007).

19 C. F. Hoon and E. C. Reynhardt, *Journal of Physics C-Solid State Physics* **16** (32), 6129 (1983).

20 A. Gutowska, L. Y. Li, Y. S. Shin, C. M. M. Wang, X. H. S. Li, J. C. Linehan, R. S. Smith, B. D. Kay, B. Schmid, W. Shaw, M. Gutowski, and T. Autrey, *Angewandte Chemie-International Edition* **44** (23), 3578 (2005).

21 A. Feaver, S. Sepehri, P. Shamberger, A. Stowe, T. Autrey, and G. Z. Cao, *Journal Of Physical Chemistry B* **111** (26), 7469 (2007).

22 L. Li, X. Yao, C. H. Sun, A. J. Du, L. N. Cheng, Z. H. Zhu, C. Z. Yu, J. Zou, S. C. Smith, P. Wang, H. M. Cheng, R. L. Frost, and G. Q. M. Lu, *Advanced Functional Materials* **19** (2), 265 (2009).

23 T. Lu, X. D. Yao, M. G. Q. Lu, and Y. H. He, *Journal of Porous Materials* **17** (1), 123 (2010).
24 T. Lu, X. D. Yao, M. G. Q. Lu, and Y. H. He, *J Colloid Interface Sci* **336** (1), 368 (2009).

Chapter 2 Literature review

Hydrogen is expected to be one of the best alternative fuels in the future. However, the present major challenges for practical mobile application are efficient storage, secure transport and acceptable working conditions of this highly flammable gas. In this chapter, previous research relating to hydrogen storage is reviewed. Based on the benefits and limitations of previous techniques and methods, a selection of efficient nanoscaffold media that have the potential for higher hydrogen storage capacity and improved the kinetics are proposed for investigation in this thesis.

2.1 Conventional hydrogen storage without a carrier medium

2.1.1 High pressure compression

For industry and laboratory applications, hydrogen gas is normally stored in high pressure cylinders. Classical high pressure tanks made of fairly cheap carbon steel are tested up to 30MPa and regularly filled up to 20MPa in most countries. However, hydrogen stored in high pressure cylinders is hardly practical for motor car applications because at 20 MPa 4 kg hydrogen occupies a volume of about 225 liters. To meet the volumetric requirement, the pressure must be over four times higher. Carbon-fiber-reinforced composite materials have been used to make novel high-pressure tanks. These containers are tested up to 60MPa for regular use, which need a special inert inner polymer coating to prevent the high pressure hydrogen from leaking.(1) In addition to the challenge this approach poses on the requirements of

high tensile stress materials and storage tank manufacture, the safety of pressurized cylinders is also a major concern, especially for family cars.

2.1.2 Low temperature condensation into liquid

The second possible approach to the storage of hydrogen without a carrier medium is low temperature refrigeration where it is cooled and stored as a liquid. However, this method faces two challenges: the efficiency of the liquefaction process and the boil-off of the liquid. The theoretical energy demand to liquefy hydrogen gas from room temperature is 3.23kWh/kg. (2) The density of liquid hydrogen is 70.8 kg/m^3. The condensation temperature of hydrogen at 1 bar is –252 °C and the vaporization enthalpy at the boiling point is 452kJ/kg. (3) Heat transfer through the insulated vessels leads to an inside pressure build-up. From safety consideration, liquid hydrogen containers are designed to be open systems to prevent strong overpressure. (1) This results direct in the loss of hydrogen.

The large amount of energy required for liquefaction and the continuous boil-off of liquid hydrogen make this storage system impractical for utilization in normal situations, except the cost of hydrogen is not a prime issue and the hydrogen is consumed in a short time, e.g. space travel applications.

2.2 Hydrogen storage with a solid medium

2.2.1 Hydrogen storage on carbon materials with large surface areas

The physical properties of materials are size dependent, significant changes of the properties can be observed when the particles or agglomerates are smaller than 10 nm, such as a large specific surface area which is beneficial to gas adsorption. The materials with large surface areas such as nanostructured carbon, nanostructured boron nitride, metal-organic framework, and mesoporous materials are widely investigated and reported in literature. (4-10) In the following sections, only the aspects of carbon materials relevant to hydrogen storage will be reviewed.

Carbon is the fourth most abundant chemical element by mass in the universe, after hydrogen, helium, and oxygen. It has different forms including the hardest naturally occurring substance (diamond) and one of the softest substances (graphite), and amorphous carbon, fullerenes, carbon nanotubes, carbon fibers, and porous carbon. These different carbons show their own characteristics of structures and properties.

Study on storing hydrogen in various forms of carbon has been very active. It is known that high surface area activated carbon can serve as a storage medium for the gas and physisorb molecular H_2 at a low temperature and high pressure due to the weak van der Waals interactions (1) . It is also reported that hydrogen can chemically bond to the C_{60} and C_{70} fullerenes. Electrochemically, C_{60} will absorb 6.3 wt% of hydrogen in the form as C_{60} H_{48}. (11) Unlike the purely physisorption with activated carbon, C_{60} carbon atoms form relatively strong covalent bonds with H atoms, with an enthalpy change (ΔH) of 285 kJ mol^{-1} H_2. This determines that a high temperature

of ~400°C is necessary for breaking the C-H bond to release the hydrogen. (12) Compared with chemisorption with other elements, this is clearly not favourable. Our focus in hydrogen storage in nanostructured carbons is therefore on physisorption.

2.2.1.1 Hydrogen adsorption in graphite

Graphite has a sheet-like structure where the atoms all lie in a plane and are only weakly bonded, via van der Waals forces, to the neighboring graphite sheets. Graphite can absorb hydrogen but the capacity is low due to its small interlayer distances and its low specific surface area. An increase of surface area of graphite can be achieved through ball milling as shown in Figure 2.1. After 4 hours milling, the specific surface area can be as high as 700m^2/g. When ball-milled in a hydrogen gas atmosphere, graphite powder showed considerable hydrogen storage capacity, but the desorption temperature is too high for it to be used practically.(13-15) It is reported that after 80h ball milling in a 1MPa hydrogen atmosphere graphite nanostructures contain up to 0.95 H atoms per carbon atom, or 7.4 wt%, from which 80% could be desorbed at temperatures >600K. (15,16)

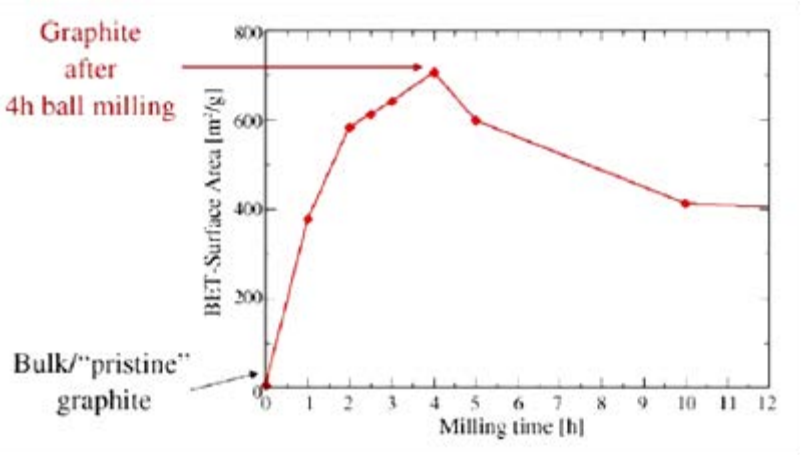

Figure 2.1 Specific surface area of milled samples. (15,16)

2.2.1.2 Hydrogen adsorption in activated carbon

Activated carbon (AC) is a synthetic carbon containing a small amount of graphite crystallites and amorphous carbon. The pore diameter is usually less than 1 nm and form a specific surface area up to 3000 m^2/g. AC has been investigated since the 1980s. A hydrogen storage capacity of 3–6 wt% was reproducibly obtained at cryo-temperatures although the capacity is below 1 wt% at room temperature. (17,18) It is believed that the reversible physisorption takes place and the amount of absorbed hydrogen is proportional to the specific surface area. Figure 2.2 shows that the high surface area is beneficial for hydrogen storage although the linear relationship between the surface area and the storage capacity is limited to the specific surface area up to ~1000 m^2/g after which it is no longer linear.

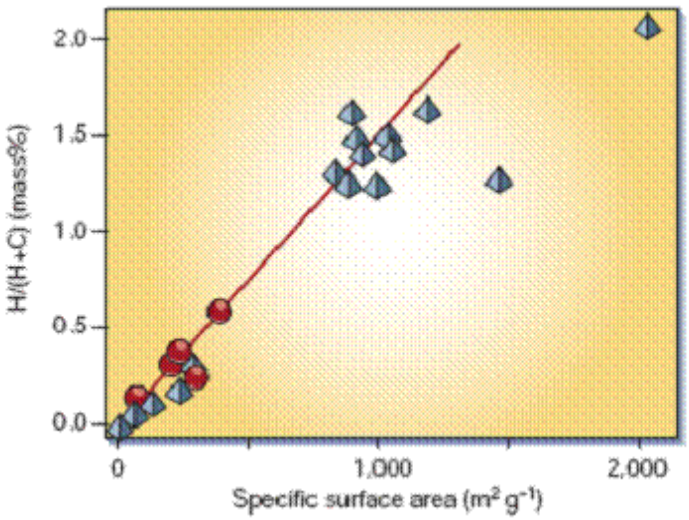

Figure 2.2 Reversibly stored amount of hydrogen on various carbon materials versus the specific surface area of the samples. Circles represent nanotube samples (best-fit line indicated), triangles represent other nanostructured carbon samples (1)

The density of adsorbed hydrogen is related to the volume of micropores which are believed to be the space for storing hydrogen molecules. Figure 2.3 shows the hydrogen adsorption isotherms of a variety of activated carbons and activated carbon fibers at 293 K and under hydrogen pressure of 10 and 70 MPa. It shows that the amount of adsorbed hydrogen (weight percent) increases with an increase in the volume of micropores (cc/g).

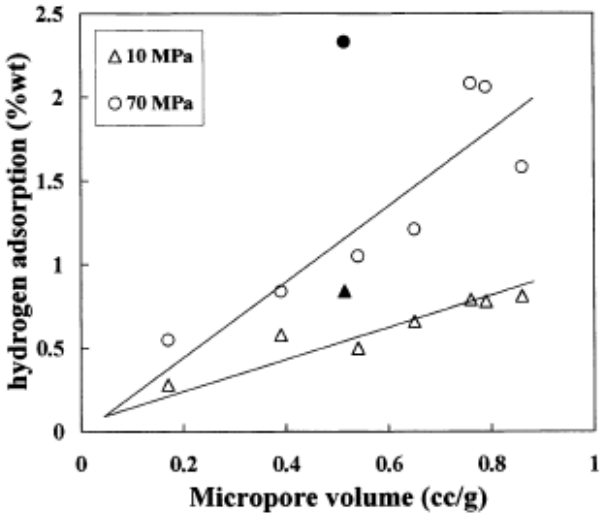

Figure 2.3: The amount of adsorbed hydrogen (wt %) versus micropore volume at 10 and 70 MPa (filled points correspond to sample KUA1).(19)

Activated carbon normally has a wide pore-size distribution.(16) Pores of different sizes exhibit different hydrogen sorption capacities. The pore diameter of activated carbon with micropores is in the region of the molecular diameter. The relationship between average pore diameter and hydrogen adsorption is shown in Figure 2.4. It can be seen that the hydrogen adsorption capacity decreased linearly with an increase in the pore size of the AC. Systematic research by Nijkamp *et al*.(20) confirmed that the pore size is a key to hydrogen storage in porous materials. He reported the storage capacities of a large number of different carbonaceous adsorbents for hydrogen at 77 K and 1 bar. They concluded that microporous adsorbents, for example zeolites and activated carbons, have appreciable sorption capacities for hydrogen.

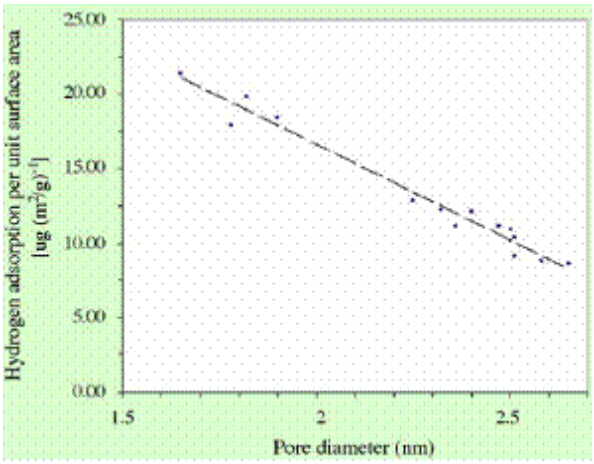

Figure 2.4: Hydrogen adsorption (μg of hydrogen per m^2 g^{-1}) vs. average pore diameter of activated PEEK carbons.(16)

2.2.1.3 Hydrogen adsorption in carbon nanotubes (CNTs)

Depending on the number of tube walls, CNTs can be classified into single-walled carbon nanotubes (SWNTs) (Figure 2.5), double-walled carbon nanotubes (DWNTs) and multi-walled carbon nanotubes (MWNTs) (Figure 2.6). SWNTs are usually 1–2 nm in diameter and tens of microns in length. The inner tube diameter of DWNTs and MWNTs are in the range of 2-3nm and 2-30nm, respectively. (21) Since it consists of a single layer of carbon, its theoretical maximum specific surface area can be as high as 2630m^2/g,(21) which equals to that of single-layer graphite. However, the experimentally demonstrated value is much smaller because SWNTs and MWNTs aggregate into bundles. Lawrence et al.(22) reported a specific surface area of SWNTs of 800 m^2/g and Gao et al.(23) accounted the surface area of open-tipped MWNTs of 840 m^2/g.

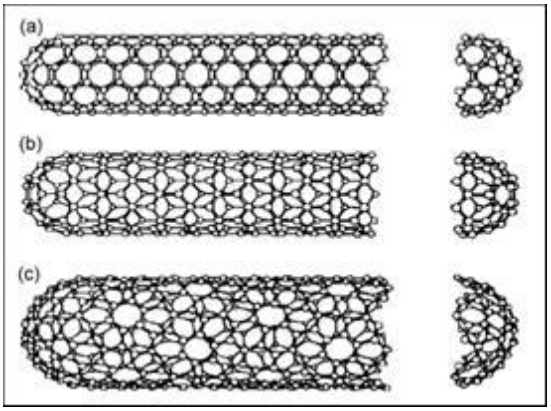

Figure 2.5: Scheme illustrating the different single-walled nanotube (SWNT) structures: (a) armchair, (b) zigzag, and (c) chiral (16)

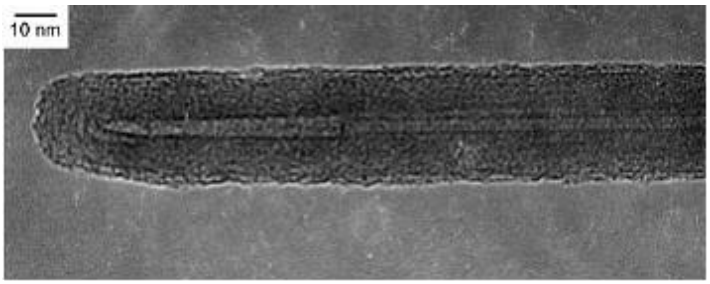

Figure 2.6: A typical TEM image of a closed, multi-walled carbon nanotube. The separation distance between the two graphite layers is 0.34 nm. (10)

In 1997, Dillon (24) first reported that SWNTs might possess excellent hydrogen storage capacity owing to their unique pore structure. They measured the hydrogen adsorption capacity of a small quantity of as-prepared SWNT-containing soot with an estimated amount of 0.1–0.2 wt% SWNTs at room temperature. Then they extrapolated a value for hydrogen adsorption capacity for pure SWNTs to be in the range of 5–10 wt%. (25)

However, the reported data for hydrogen storage capacity in CNTs is highly scattered and cannot be reproduced. (26) For example, Ye et al (27) reported a hydrogen storage capacity of 8 wt% for crystalline ropes of SWNTs at a cryogenic temperature of 80K and under a hydrogen pressure of 12MPa. Liu et al (28) reported that a hydrogen storage capacity of 4.2 wt% could be reached at room temperature and 10MPa hydrogen pressure. Chen et al (29) reported that a very high hydrogen uptake of 20 wt% and 14 wt% could be achieved in milligram quantities of Li-doped and K-doped MWNTs, respectively. Recently, it is believed that CNTs themselves can only adsorb ~ 2 wt% hydrogen, which is far below the DOE target.

Studies on hydrogen storage using Ni (23,30,31) and Pt (32) nanoparticle doped CNTs have also been carried out. In the case of CNT decorated with 6 wt.% Ni nanoparticles, 2.8 wt.% of hydrogen was reversibly chemisorbed.(31) Theoretical study by Yildirim and Ciraci claimed that each Ti atom doped on a CNT surface could feasibly bind up to four hydrogen molecules. The first molecule is bound dissociatively with no energy barrier and the remaining three with significantly elongated H-H bonds.(33) Such a material could store up to 8 wt.% H_2. However, this result is yet to be confirmed experimentally.(34)

2.2.1.4 Hydrogen adsorption in carbon with high microporosity

Both experimental and theoretical studies have shown that the presence of micropore (especially those of 0.6-0.7nm in diameter) was one of the key parameters which influence the hydrogen adsorption capacity.

Rzepka, Lamp and de la Casa-Lillo reported in 1998 (35) the hydrogen uptake calculated by a grand canonical ensemble Monte Carlo program (GCEMC). The simulations showed that the optimum pore size was below 1nm at room temperature for gaseous hydrogen adsorption. Figure 2.7 shows the results of calculations of the dependence of the hydrogen storage capacity on the pore size *d* of a carbon slitpore and a nanotube at room temperature and 10 MPa. There is a sharp maximum in the volumetric storage capacity at a pore size of about d = 7 Å for both pore geometries. The total gravimetric storage capacity of a carbon slitpore with d =7 Å is 1.3 wt %. For larger pore sizes the volumetric storage capacity decreases asymptotically to the density of the pure compressed gas (7.6 kg/m^3) while the gravimetric storage capacity, i.e., the total amount of stored hydrogen compared to the number of pores, increases almost linearly with *d* for both geometries. At a large *d*, the excess storage capacity is nearly independent of the pore size and pore geometry and amounts to about 0.6 wt %.

This theoretical result is in good agreement with experimental results. They also found that, at the temperature of liquid nitrogen, the best storage capacity was found

with slit pores having a width of 0.7nm. This configuration allows the adsorption of two layers of hydrogen molecules even at relatively low pressures such as 5MPa.

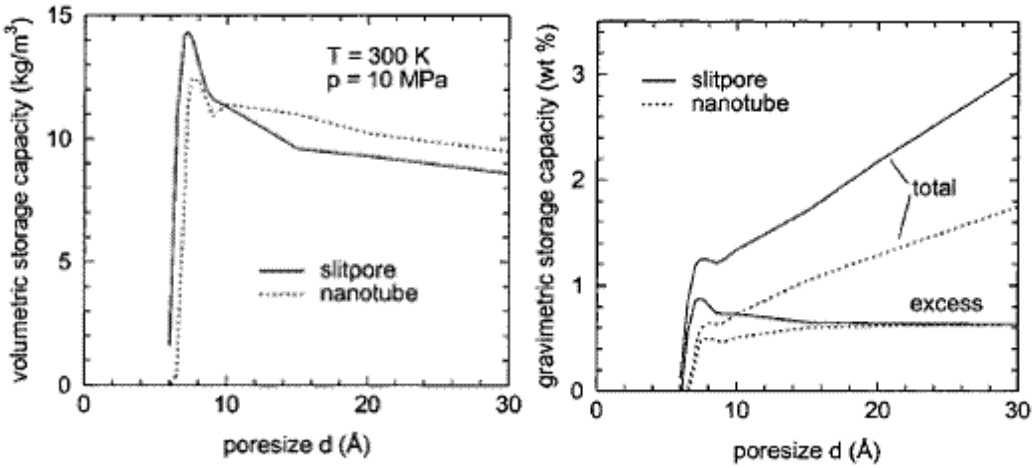

Figure 2.7: Calculated amount of adsorbed hydrogen as a function of pore size *d* for T = 300 K and p = 10 MPa for both pore geometries: (a, left) volumetric storage capacity, (b, right) gravimetric storage capacity.(35)

De la Casa-Lillo and co-workers (19) conducted experimental work on hydrogen adsorption in a large variety of activated carbons and activated carbon fibers at a wide range of pressure. The experimental results matched fairly well with theoretical calculations found in the literature and confirmed that the optimum pore size for hydrogen adsorption in porous carbons was that which can hold two layers of adsorbed hydrogen (i.e., pore size of about 0.6 nm). Figure 2.8 plots the hydrogen density inside the micropores measured experimentally (293 K and pressures of 10 and 70 MPa) versus the mean pore size of the samples. In the experimental results, the mean pore size has been determined from gas adsorption (N_2 and CO_2 at 77K and

273 K, respectively) at subatmospheric pressures. The experimental curve matches reasonably well with the theoretical calculations. In both cases, the maximum in the density of adsorbed hydrogen is found to be a function of the pore size. The optimum theoretical pore size to store hydrogen is 0.36 nm for single layer adsorption of H_2 and 0.56 nm for double layer adsorption of H_2. The experimentally measured adsorption results show that the optimum pore size is 0.66 nm, confirming the assumption of double layer adsorption.

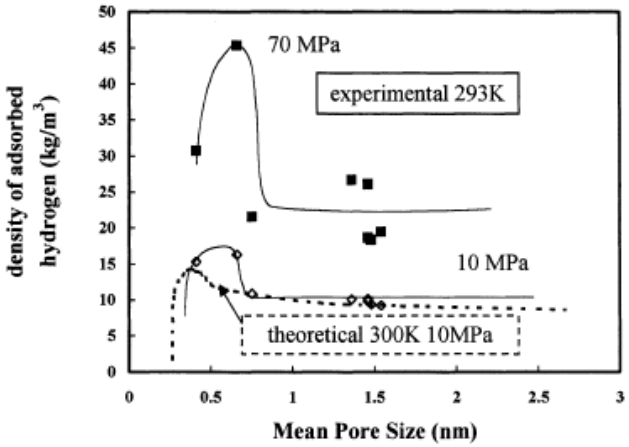

Figure 2.8： Density of adsorbed hydrogen inside the pores (kg/m^3) versus mean pore size (- - -：theoretical results).(19)

Wang and Johnson (36) studied the adsorption of hydrogen gas into single-walled carbon nanotubes and idealized carbon slit pores in their computer simulation. In their two studies (36,37), they reported hydrogen storage capacities around 5wt.% at 1 MPa in slit pores with a width of 0.6–0.7nm. Although the adsorption potential for hydrogen in SWNTs is enhanced compared to slit pores of the same size, their

calculations show that the storage capacity of an array of tubes is less than that for idealized slit pore geometry, except at very low pressures.(37)

There are different mechanisms of adsorption depending on the geometry of the adsorbent and the temperature of adsorption. Multilayer adsorption occurs if the adsorption takes place on an open surface and volume filling would happen in pores narrower than 2 nm. Capillary condensation could happen in a pore larger than 2 nm but smaller than 50 nm. A different mechanism of adsorption is monolayer surface coverage, which can be calculated by the BET theory. The total storage capacity in a porous solid is the sum of contributions due to adsorption on solid surface and in the void space.(38)

2.2.1.5 Hydrogen adsorption in ordered mesoporous carbon

Ordered mesoporous materials can be synthesized by a novel liquid crystal templating approach, with pore sizes from 2 to 50 nm and surface areas of up to 2100 m^2/g. Adsorption of hydrogen using such materials has attracted increasing interests. The ordered mesoporous carbons are characterized with several specific features that may be beneficial to hydrogen storage:(39-42)

1. Large microporous volume;
2. The presence of a three dimensional interconnected mesoporous network which enhances the dynamics of hydrogen diffusion in the material; (43,44)
3. The possibility to control the micro- and the meso-porosity.

Gadiou and colleagues (45) studied the influence of textural properties on the adsorption of hydrogen on ordered nanostructured carbons. Carbon materials were prepared by a template method from two mesoporous silica matrix and with three different carbon precursors (See Table 2.1). These materials were characterized by gas adsorption and shown that the mesoporous structure of the carbon is mainly related to the silica template, while the microporous volume is dependent on the nature of the carbon precursor and the carbon synthesis process. Liquid phase insertion of sucrose leads to the highest microporous volume, while chemical vapor insertion of propylene leads to the lowest. The adsorption of hydrogen on these carbon materials was tested at 77K between 0.1 and 1MPa. The results, presented in Figure 2.9, show that the carbon synthesis method has a great influence on the quantity of hydrogen adsorbed by the material.

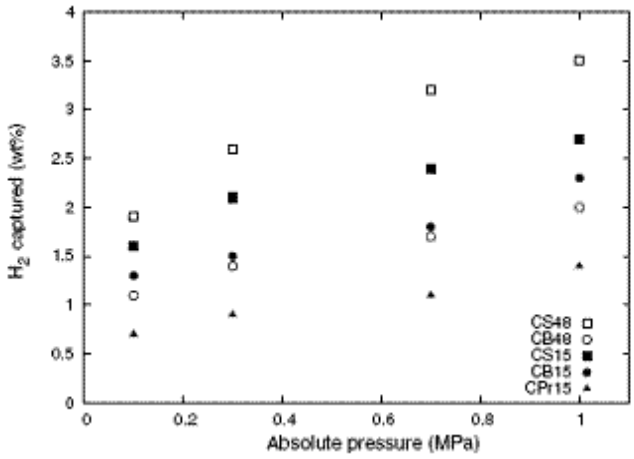

Figure 2.9: Hydrogen adsorption capacity of nanostructured carbon materials at 77K as a function of pressure. (45)

Table 2.1 Textural characteristics of the carbon materials

Sample	CB15	CS15	CPr15	CS48	CB48
Silica template	SBA-15	SBA-15	SBA-15	MCM-48	MCM-48
Carbon precursor	Pitch	Sucrose	Propylene	Sucrose	Pitch
Total surface area (m^2/g)	754	1200	711	2390	1130
Total porous volume Vp (cm^3/g)	0.50	0.90	0.76	1.22	0.64
Microporous volume VN_2 (cm^3/g)	0.23	0.41	0.20	0.68	0.33
Microporous volume VCO_2 (cm^3/g)	0.26	0.27	0.09	0.36	0.18
Pore diameter Dp, BJH (nm)	3.34	3.84	4.78	2.82	4.02

Furthermore, Gadiou (46) suggested that the characterization of microporous volume through CO_2 adsorption at 273K and Dubinin-Radushkevich (DR) analysis allowed a good evaluation of the hydrogen storage capacity of these mesoporous carbons with a high microporosity. Accordantly, Texier-Mandoki and coworkers (47) showed that the microporous volume determined by CO_2 adsorption at 273K is a better

correlation parameter than by N_2 adsorption at 77K for activated carbons with high microporous volumes.

It is reported that the pores with a size of 1-2 nm are important for storing hydrogen. Shao and coworkers (48) reported a 7wt% storage of hydrogen at 77K and under a hydrogen pressure of 1 MPa, with a highly microporous carbon material (mesocarbon microbeads) which had a BET surface area of 3180 m^2/g, average pore size of 2.47 nm, and a pore volume of 1.9 cm^3/g. Therefore, it is important to control the pore size and its distribution of such materials to achieve a high hydrogen storage capacity. Fang and coworkers controlled the pore size and wall thickness of silica templates through variation of HTAB (Hexadecyltrimethylammonium bromide) to $C_{16}EO_8$ ratio, the surfactants they used. Results shown in Table 2.2 demonstrate that pore sizes can be controlled to a very narrow range of 2.1-2.8 nm. (49)

Table 2.2 Structure properties of synthesized silica and silica-templated carbon obtained at various ratios of HTAB to $C_{16}EO_8$.

HTAB:$C_{16}EO_8$	Silica pore Diameter (nm)	Silica wall Thickness (nm)	Carbon pore Diameter (nm)
4:0	2.6	1.4	2.1
3:1	2.7	1.5	2.5
2:2	2.9	1.7	2.7
1:3	3.1	1.8	2.8

2.2.2 Hydrogen storage in ammonia borane

Ammonia borane (NH_3BH_3, AB) contains 19.6 wt% hydrogen was first synthesized in the middle of 1950s as part of the US government's program to develop fuels for jets and rockets. (50) AB is a colorless crystal at room temperature, with a calculated density of 0.74 g/cm^3. (50) It is stable in air and soluble in water and other relatively polar solvents. Pure AB melts in the temperature range 110-114 °C. (51,52) A melting point of 125 °C was also claimed for the ultra pure material. (53)

AB is a remarkable molecule which contains both hydridic B-H and protic N-H bonds and a strong B-H bond that under most conditions hydrogen loss is favored over dissociation to ammonia and borane. (54) The solid state structure of AB has been determined using both X-ray and neutron diffraction. AB has a staggered conformation with a B-N bond distance of 1.564 (6) Å in the solid state. (55) The gas phase structure of AB determined using microwave spectroscopy reveals a significantly longer B-N bond distance of 1.6722 (5) Å. (56) The solid state structure of neat AB exhibits short BH· · ·HN intermolecular contacts; the hydridic hydrogen atoms on boron are 2.02Å away from the protic hydrogen atoms on the nitrogen of an adjacent molecule, a distance less than the Van der Waals distance of 2.4 Å, (57) an interaction constituting a dihydrogen bond. (57-59)

The decomposition of AB has been investigated both theoretically and experimentally and is known to occur by a multistep process involving exothermic reactions as shown below. (60,61)

$H_3NBH_3 \rightarrow H_2NBH_2 + H_2$ (1)

$H_2NBH_2 \rightarrow HNBH + H_2$ (2)

$HBNH \rightarrow BN + H_2$ (3)

Probed by differential scanning calorimetry (DSC) and volumetric analyses, the first step of decomposition shown in reaction equation (1) initiates at about 100 °C and reaches a maximum upon melting of AB. During this step, AB melts and yields one equivalence of hydrogen and solid products consisting mostly of aminoborane (H_2NBH_2). The second decomposition step shown in reaction equation (2) releases another equivalence of hydrogen and occurs over a broad temperature range 150±40 °C. During the second step, an inorganic analog of benzene named borazine (NHBH) may also be obtained in gas form, which is toxic and poison to the proton exchange membrane fuel cells. To lose all hydrogen contained in AB in the form of reaction (3) requires a temperature above 500 °C, which is considered impractical for hydrogen storage. According to recent data, these reactions provide 7.2, 14.4 and 19.6 wt% hydrogen yield, respectively. (62)

The hydrogenation and dehydrogenation enthalpies of AB reactions have been explored theoretically. Dixon and Gutowski (60) used *ab initio* molecular orbital theory to show that the enthalpies of reaction at 298 K for equation (1) is -21.3

kJ/mol, equation (2) is 131.4 kJ/mol, and equation (3) is 562.3 kJ/mol. Himmel and Schnöckel(63) used Gaussian98 (B3LYP method) to calculate the gas phase reaction enthalpies at 298.2K. The results are slightly different for equation (1) (exothermic, -26.6 kJ/mol) and equation (2) (endothermic, 133.3 kJ/mol).

The fact that AB starts to release hydrogen at temperature below its melting point indicates a mechanism of hydrogen release from solid state AB. An in situ ^{11}BMAS-NMR study by Autrey et al. (64) described the first decomposition step of AB by an induction, nucleation and growth mechanistic pathway. It is essential to understand the chemical and physical processes occurring during the induction period which curtails the onset of hydrogen release from solid AB at temperature below 100°C. There could be a physical change, i.e. creation of defects in solid AB or some chemical change, such as the formation of a more reactive chemical species, the initial coupling product, a linear dimer, or formation of DADB (diammoniate of diborane). By labeling boron and nitrogen bonds with deuterium and following the reaction with analysis of the volatile products, Smith et al. suggested a bimolecular reaction pathway, wherein the initially formed mobile AB species isomerizes to yield reactive isomer DADB. The subsequent dimolecular reaction between DADB and AB initiates the hydrogen release and phase growth processes. This mechanistic understanding was partially supported by the computational study of Dixon et al., in which the formed ionic isomer DADB from two AB monomers was suggested to

play a dominant role in the hydrogen release from AB. Some important species related to ammonia borane dehydrogenation are represented in Figure 2.10.

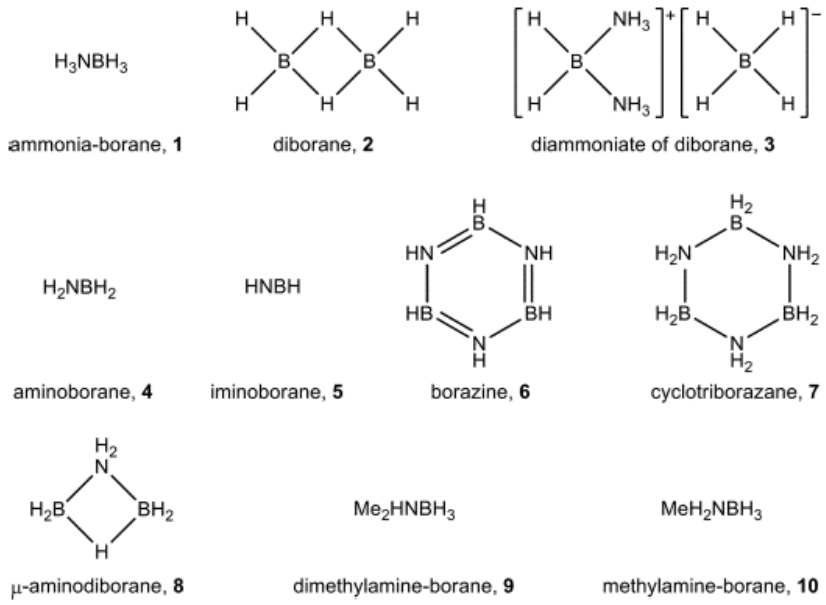

Figure 2.10: Scheme illustrating ammonia borane and some important species related to ammonia borane dehydrogenation (54)

While recent efforts show that there has been much progress on new promoters for the controlled release of hydrogen from AB under mild conditions, there remain economic and technical challenges for it to be a sustainable and environmentally friendly energy source, namely,

1) The system has to be able to release H_2 at an appropriate rate

2) The system has to be able to release most of the available H_2 to achieve the gravimetric requirements;

3) The system must produce a minimum of volatile by-products, such as borazine;

4) An economically viable method must be developed for the regeneration of AB.

Indeed, the third point may be the ultimate barrier to its use, and depends on what products the system produce.

For practical application of AB as a hydrogen storage material for a polymer electrolyte membrane (PEM) fuel cell, the optimum decomposition temperature should be around 85 °C, which is the working temperature of the PEM. (1) Recent researches focus on the use of catalysts and nanoscale agents to promote hydrogen release from AB under mild conditions, i.e. improving the kinetics of AB dehydrogenation reactions and decreasing its decomposition temperature.

The first example of transition metal catalyzed dehydrogenation of AB was reported by Roberts et al. in 1989, (65) using 10% palladium on charcoal. As part of their wider research program on metal catalyzed dehydrocoupling reactions, Manners et al. in 2003, (66) used 0.6 mol% of $\{Rh(1,5\text{-cod})(\mu\text{-Cl})\}_2$ (cod = cyclooctadiene) as catalyst precursor. Later, Manners et al. (67) reported the homogeneous titanocene catalyzed dehydrocoupling of Me_2HNBH_3. The mechanism of this process has also been studied theoretically by Luo and Ohno. (68) Heinekey, Goldberg et al. (69) reported that the iridium pincer complex catalyzes the release of one equivalent of hydrogen from AB in 14 minutes at room temperature at 0.5 mol% loading. Baker et al. (70) reported that in-situ treatment of $Ni(cod)_2$ with a suitable ligand N-heterocyclic carbine affords long-life catalysts which release 2.5 equivalence of

hydrogen from AB in diglyme solvent at 333K, giving a soluble cross linked borazine product. Kang et al. (71) found that mechanically milling AB with magnesium hydride can improve the dehydrogenation properties of AB on both kinetic and thermochemical aspects. For the mechanically milled AB/0.5MgH_2 material, over 8 wt% hydrogen can be released from AB within 4 hours at around 100°C without volatile products.

Nanostructured materials may offer a solution to hydrogen storage because they often exhibit significantly different physical, chemical, and thermodynamic characteristics from their bulk counterparts. Confining hydrides inside nanoporous scaffolds has been demonstrated to be an effective approach to tuning hydrogen storage properties. In nanoscale materials, introducing defects and vacancies and shorter diffusion distances can result in faster kinetics. In addition, changes in surface energies with decreasing particle size can change the thermodynamic stability of the reactants and further alter the hydrogen release mechanisms.

Over the last five years, there has been some promising research work focusing on hydrogen release from AB. Autrey and coworkers (72) reported their results on the thermolysis of AB contained within mesoporous silica scaffolds. In their work, AB was deposited into SBA-15 using a methanol carrier solvent, achieving a 1:1 weight ratio between AB and SBA-15. Mesoporous silica materials have an extremely high surface area and a highly ordered pore structure. SBA-15 which used in their work is

hexagonally ordered mesoporous silica with parallel channels and a 7.5 nm pore diameter. Because of the porous nature of the silica scaffold, the internal channels of SBA-15 were filled rapidly with a solution of AB through a capillary action. According to their results from temperature programmed desorption mass spectrometry (TPD/MS) (Figure 2.11), nanoporous silica depressed the thermolysis onset temperature by approximately 15°C compared to neat AB. Furthermore, they observed a suppression of formation of volatile borazine, an especially important feature for the use of this chemical in the current fuel cell technology.

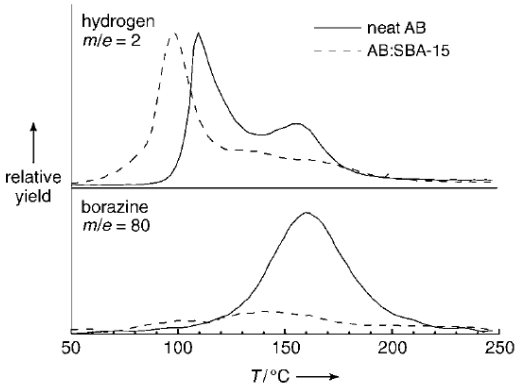

Figure 2.11 TPD/MS (1°C/min) of volatile products generated by heating neat AB (solid line) and AB:SBA-15 (dashed line); m/e = 2 (H_2) and m/e = 80 (borazine, c-$(NHBH)_3$). The value m/e =2 (H_2) is normalized to the area under the curve for neat AB (solid line). The corresponding scalar was used to normalize the m/e = 80 borazine data for AB:SBA-15. (72)

Nanoporous silica may accelerate H_2 release from AB by one of several possible mechanisms. Because the channels of the silica framework impart a microstructured

reaction environment, a templating effect or defect sites may be responsible for the rate increase. The molecular structure of the substrate walls includes SiOH groups that may participate in catalysis or control the product distribution. Whichever mechanism proceeds, the enthalpy of H_2 release from AB in nanoporous silica was measured approximately 20 kJ mol^{-1} less exothermic than H_2 loss from neat AB. Arrhenius treatment of temperature dependent rate data is shown in Figure 2.12. The activation energy of thermolysis of pure AB (Ea = 184 ± 5 kJ mol^{-1}) was significantly larger than that for the SBA-15–AB system (Ea = 67 ± 5 kJ mol^{-1}). Moderation of the reaction exothermicity indicates different products are formed from the thermolysis of neat AB, a result that may have consequences on energy efficiency in the regeneration of AB.

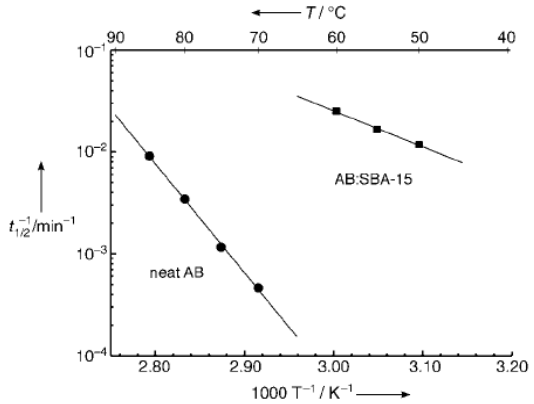

Figure 2.12 Arrhenius treatment of the temperature-dependent rate data yields a straight line with a gradient that is proportional to the apparent activation energy for hydrogen loss from neat AB (•; Ea ≈184 $kJmol^{-1}$) or AB in the scaffold (!; Ea ≈ 67 $kJmol^{-1}$). (72)

Infusing AB in mesoporous silica significantly improved the dehydrogenation kinetics and also suppressed borazine formation. However, silica is relatively heavy and has poor thermal conductivity. In contrast, the similar porous carbon material is lighter, has a tunable pore diameter, and can provide a thermal conduction pathway. Autrey et al. (73) investigated the performances of AB in carbon materials and found that, when AB was impregnated inside a nanoporous carbon, the same effect occurred.

Feaver and coworkers (73) introduced porous carbon cryogels which were derived from resorcinol formaldehyde hydrogels. These nanocomposites release two hydrogen molecules in a two-in-one reaction at reduced dehydrogenation temperatures ~90°C. A 9 wt% hydrogen release from AB was obtained, and the formation and/or release of borazine were suppressed. (Figure 2.13) Their results demonstrated that nanocrystallite AB captured inside the mesopores of the carbon crygel matrix possessed a huge surface to volume ratio, resulting in a significantly larger surface energy, and thus destabilizing the hydrogen bonding network of AB, thus lowered the energy barrier for hydrogen release.

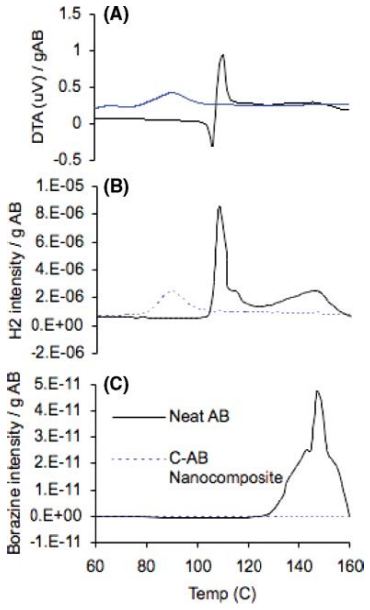

Figure 2.13 (A) DTA results of the C-AB nanocomposite and neat AB with a heating rate of 1 °C /min; (B) H_2 MS readings showing the H_2 release at ~90 °C in a C-AB nanocomposite and at 110 and 150 °C in neat AB; and (C) the borazine MS readings showing no release of borazine from the C-AB nanocomposite.(73)

Sepehri and coworkers (74) investigated the differences between the porous silica and porous carbon supports with spectroscopic studies. They reported findings from Fourier transform infrared spectroscopy (FTIR) and in situ ^{11}B nuclear magnetic resonance (NMR) results on the dehydrogenation pathways of CC-AB. The information identified an alternate competing pathway for hydrogen release from CC-AB that was consistent with the enhanced kinetics and greater reaction exothermicity relative to neat AB and AB supported on mesoporous silica. They found a lower temperature hydrogen release and a new product for carbon crygel AB nanocomposite relative to AB. The new product suggested a new mechanism: the destabilization of AB due to the formation of surface –O-B bonds. When the

temperature was increased from 85 to 150 °C, the reaction pathways did not change but the rate of dehydrogenation process increased (Figure 2.14). The suppression of borazine during the dehydrogenation process was also confirmed by this mechanism.

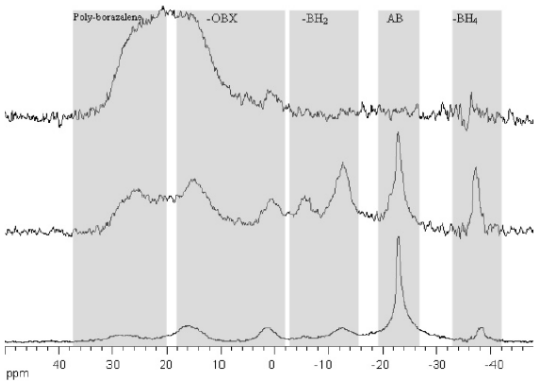

Figure 2.14 ^{11}B NMR of CC-AB before heating (bottom), after heating to 85 °C for 10 min (middle), and after heating to 150 °C for 10 min (top).(74)

Recently, Li and coworkers (62) reported a new catalytic strategy involving lithium catalysis and nanostructure confinement in mesoporous carbon CMK-3 for the thermal decomposition of AB. When loaded on a 5% Li/CMK-3 framework, AB releases ~7 wt% of hydrogen at a very low temperature of ~ 60 °C, and entirely suppresses borazine and ammonia emissions.

The hydrogenation of AB and AB/CMK-3 nanocomposite was measured by thermogravimetry combined with mass spectroscopy (TG/MS). In Figure 2.15, neat AB starts to decompose at above 100°C via a two-step process (around 110 °C and 145 °C) and the weight loss from neat AB reaches around 20 wt% below 150 °C. MS

characterization (Figure 2.16) demonstrated the gas released from neat AB contained not only hydrogen but also volatile products, namely, ammonia and borazine. Compared with neat AB, the decomposition of AB/CMK-3 nanocomposite occurs below 75 °C with only one step for the release of gaseous substance and approaches 27 wt% of weight loss below 150 °C. Figure 2.16 also demonstrated that AB/CMK-3 releases hydrogen at a lower temperature than neat AB with a desorption peak at 95 °C. The process of dehydrogenation is enhanced and borazine is suppressed when heating AB inside CMK-3. It needs to be noted that a large amount of ammonia was detected from the decomposition of AB/CMK-3. This is clearly detrimental and needs to be prevented for future applications.

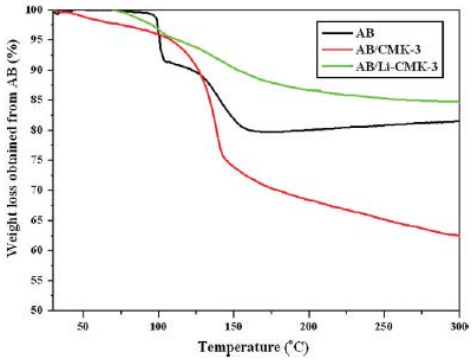

Figure 2.15 Hydrogen releasing from neat AB, AB/CMK-3, and AB/Li-CMK-3 measured by TG (62)

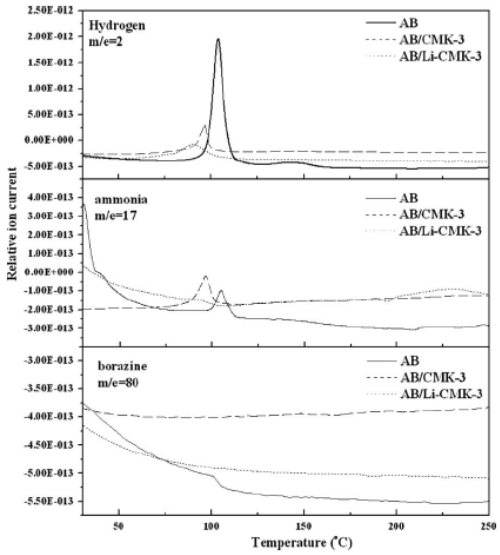

Figure 2.16 The MS results of AB, AB/CMK-3, and AB/Liþ-CMK-3 (62)

The first notable dehydrogenation property of AB/Li-CMK-3 is that only hydrogen gas was detected when heating up to 150°C. This phenomenon indicates a complete suppression of ammonia and borazine release from AB, and suggests that Li plays an important role in nitrogen immobilization during the AB thermal decomposition. Moreover, hydrogen release of AB/Li-CMK-3 initially occurred at very low temperature of around 55 °C with a broad peak at 90 °C and reached 11 wt% when heated to 150 °C. The catalytic effect of the Li based catalysts combined with the confinement of CMK-3 results in a further acceleration of dehydrogenation kinetics of AB within the Li-CMK-3 framework. These results suggest that a synergistic interaction between catalyst and nanostructure can provide a very effective strategy to significantly accelerate the dehydrogenation kinetics and suppress the emission of ammonia from AB.

From the above literature survey, it is found that a number of mesoporous materials have been used as scaffolds to support AB and the nano-confinement approach has shown unique advantages to tune the hydrogen release behavior of AB. However, in previous reports of hydrogen release from AB using nanoporous scaffolds, generally one nanoporous material was chosen in one case. A comprehensive study of AB/nanoscaffolds thermal decomposition behavior where the structural parameters such as pore diameter and wall composition are systematically adjusted has not been reported. It will be important to understand the influence of pore diameters and wall compositions of nanoporous scaffolds on the hydrogen release performance of AB, through which optimized porous materials can be used for advanced applications of AB in hydrogen storage.

References

1 L. Schlapbach and A. Zuttel, *Nature,* Hydrogen-storage materials for mobile applications, **414** (6861), 353 (2001).

2 M. Von Ardenne, *Effekte der Physik.,* EFFEKTE PHYS IHRE AN p. 712 (1990).

3 W. B. Leung, N. H. March, and H. Motz, *Physics Letters A,* Primitive Phase-Diagram For Hydrogen, **56** (6), 425 (1976).

4 M. Fichtner, *Advanced Engineering Materials,* Nanotechnological aspects in materials for hydrogen storage, **7** (6), 443 (2005).

5 M. Dinca, A. Dailly, Y. Liu, C. M. Brown, D. A. Neumann, and J. R. Long, *Journal Of The American Chemical Society,* Hydrogen storage in a microporous metal-organic framework with exposed Mn2+ coordination sites, **128** (51), 16876 (2006).

6 M. Conte, P. Prosini, and S. Passerini, *Materials Science And Engineering B-Solid State Materials For Advanced Technology,* Overview of energy/hydrogen storage: state-of-the-art of the technologies and prospects for nanomaterials, **108** (1-2), 2 (2004).

7 A. Zuttel, P. Wenger, P. Sudan, P. Mauron, and S. I. Orimo, *Materials Science And Engineering B-Solid State Materials For Advanced Technology,* Hydrogen density in nanostructured carbon, metals and complex materials, **108** (1-2), 9 (2004).

8 H. G. Schimmel, G. J. Kearley, M. G. Nijkamp, C. T. Visserl, K. P. de Jong, and F. M. Mulder, *Chemistry-A European Journal,* Hydrogen adsorption in carbon nanostructures: Comparison of nanotubes, fibers, and coals, **9** (19), 4764 (2003).

9 Y. Kojima, Y. Kawai, A. Koiwai, N. Suzuki, T. Haga, T. Hioki, and K. Tange, *Journal Of Alloys And Compounds,* Hydrogen adsorption and desorption by carbon materials, **421** (1-2), 204 (2006).

10 C. N. R. Rao and M. Nath, *Dalton Transactions,* Inorganic nanotubes, (1), 1 (2003).

11 A. Huczko, *Przemysl Chemiczny,* Storage of hydrogen in fullerenes and carbon nanotuhes, **81** (1), 19 (2002).

12 G. Sandrock, *Journal Of Alloys And Compounds,* A panoramic overview of hydrogen storage alloys from a gas reaction point of view, **295**, 877 (1999).

13 S. Orimo, G. Majer, T. Fukunaga, A. Zuttel, L. Schlapbach, and H. Fujii, *Applied Physics Letters,* Hydrogen in the mechanically prepared nanostructured graphite, **75** (20), 3093 (1999).

14 D. M. Chen, T. Ichikawa, H. Fujii, N. Ogita, M. Udagawa, Y. Kitano, and E. Tanabe, *Journal Of Alloys And Compounds,* Unusual hydrogen absorption properties in graphite mechanically milled under various hydrogen pressures up to 6 MPa, **354** (1-2), L5 (2003).

15 M. Francke, H. Hermann, R. Wenzel, G. Seifert, and K. Wetzig, *Carbon,* Modification of carbon nanostructures by high energy ball-milling under argon and hydrogen atmosphere, **43** (6), 1204 (2005).
16 R. Strobel, J. Garche, P. T. Moseley, L. Jorissen, and G. Wolf, *Journal Of Power Sources,* Hydrogen storage by carbon materials, **159** (2), 781 (2006).
17 C. Carpetis and W. Peschka, *International Journal Of Hydrogen Energy,* A Study On Hydrogen Storage By Use Of Cryoadsorbents, **5** (5), 539 (1980).
18 R. Chahine and T. K. Bose, *International Journal Of Hydrogen Energy,* Low-Pressure Adsorption Storage Of Hydrogen, **19** (2), 161 (1994).
19 M. A. de la Casa-Lillo, F. Lamari-Darkrim, D. Cazorla-Amoros, and A. Linares-Solano, *Journal Of Physical Chemistry B,* Hydrogen storage in activated carbons and activated carbon fibers, **106** (42), 10930 (2002).
20 M. G. Nijkamp, Jemj Raaymakers, A. J. van Dillen, and K. P. de Jong, *Applied Physics A-Materials Science & Processing,* Hydrogen storage using physisorption - materials demands, **72** (5), 619 (2001).
21 C. Liu and H. M. Cheng, *Journal Of Physics D-Applied Physics,* Carbon nanotubes for clean energy applications, **38** (14), R231 (2005).
22 J. Lawrence and G. Xu, *Applied Physics Letters,* High pressure saturation of hydrogen stored by single-wall carbon nanotubes, **84** (6), 918 (2004).
23 X. P. Gao, Y. Lan, G. L. Pan, F. Wu, J. Q. Qu, D. Y. Song, and P. W. Shen, *Electrochemical And Solid State Letters,* Electrochemical hydrogen storage by carbon nanotubes decorated with metallic nickel, **4** (10), A173 (2001).
24 A. C. Dillon, K. M. Jones, T. A. Bekkedahl, C. H. Kiang, D. S. Bethune, and M. J. Heben, *Nature,* Storage of hydrogen in single-walled carbon nanotubes, **386** (6623), 377 (1997).
25 A. C. Dillon and M. J. Heben, *Applied Physics A-Materials Science & Processing,* Hydrogen storage using carbon adsorbents: past, present and future, **72** (2), 133 (2001).
26 M. Ritschel, M. Uhlemann, O. Gutfleisch, A. Leonhardt, A. Graff, C. Taschner, and J. Fink, *Applied Physics Letters,* Hydrogen storage in different carbon nanostructures, **80** (16), 2985 (2002).
27 Y. Ye, C. C. Ahn, C. Witham, B. Fultz, J. Liu, A. G. Rinzler, D. Colbert, K. A. Smith, and R. E. Smalley, *Applied Physics Letters,* Hydrogen adsorption and cohesive energy of single-walled carbon nanotubes, **74** (16), 2307 (1999).
28 C. Liu, Y. Y. Fan, M. Liu, H. T. Cong, H. M. Cheng, and M. S. Dresselhaus, *Science,* Hydrogen storage in single-walled carbon nanotubes at room temperature, **286** (5442), 1127 (1999).
29 P. Chen, X. Wu, J. Lin, and K. L. Tan, *Science,* High H-2 uptake by alkali-doped carbon nanotubes under ambient pressure and moderate temperatures, **285** (5424), 91 (1999).
30 J. Y. Lee, H. Lee, and H. S. Kim, in *Pricm 5: The Fifth Pacific Rim International Conference On Advanced Materials And Processing, Pts 1-5* (2005), Vol. 475-479, pp. 2463.

31 H. S. Kim, H. Lee, K. S. Han, J. H. Kim, M. S. Song, M. S. Park, J. Y. Lee, and J. K. Kang, *Journal Of Physical Chemistry B,* Hydrogen storage in Ni nanoparticle-dispersed multiwalled carbon nanotubes, **109** (18), 8983 (2005).

32 S. C. Mu, H. L. Tang, M. Pan, and R. Z. Yuan, *Journal Of Wuhan University Of Technology-Materials Science Edition,* Synthesis and evaluation on performance of hydrogen storage of multi-walled carbon nanotubes decorated with platinum, **18** (3), 33 (2003).

33 T. Yildirim and S. Ciraci, *Physical Review Letters,* Titanium-decorated carbon nanotubes as a potential high-capacity hydrogen storage medium, **94** (17) (2005).

34 G. G. Wildgoose, C. E. Banks, and R. G. Compton, *Small,* Metal nanoparticles and related materials supported on carbon nanotubes: Methods and applications, **2** (2), 182 (2006).

35 M. Rzepka, P. Lamp, and M. A. de la Casa-Lillo, *Journal Of Physical Chemistry B,* Physisorption of hydrogen on microporous carbon and carbon nanotubes, **102** (52), 10894 (1998).

36 Q. Y. Wang and J. K. Johnson, *Journal Of Chemical Physics,* Molecular simulation of hydrogen adsorption in single-walled carbon nanotubes and idealized carbon slit pores, **110** (1), 577 (1999).

37 Q. Y. Wang and J. K. Johnson, *Journal of Physical Chemistry B,* Optimization of carbon nanotube arrays for hydrogen adsorption, **103** (23), 4809 (1999).

38 L. Zhou, *Renewable & Sustainable Energy Reviews,* Progress and problems in hydrogen storage methods, **9** (4), 395 (2005).

39 R. Ryoo, S. H. Joo, and S. Jun, *Journal Of Physical Chemistry B,* Synthesis of highly ordered carbon molecular sieves via template-mediated structural transformation, **103** (37), 7743 (1999).

40 C. Vix-Guterl, S. Saadallah, L. Vidal, M. Reda, J. Parmentier, and J. Patarin, *Journal Of Materials Chemistry,* Template synthesis of a new type of ordered carbon structure from pitch, **13** (10), 2535 (2003).

41 C. Vix-Guterl, S. Boulard, J. Parmentier, J. Werckmann, and J. Patarin, *Chemistry Letters,* Formation of ordered mesoporous carbon material from a silica template by a one-step chemical vapour infiltration process, (10), 1062 (2002).

42 J. Parmentier, S. Saadhallah, M. Reda, P. Gibot, M. Roux, L. Vidal, C. Vix-Guterl, and J. Patarin, *Journal Of Physics And Chemistry Of Solids,* New carbons with controlled nanoporosity obtained by nanocasting using a SBA-15 mesoporous silica host matrix and different preparation routes, **65** (2-3), 139 (2004).

43 M. Kruk, M. Jaroniec, C. H. Ko, and R. Ryoo, *Chemistry Of Materials,* Characterization of the porous structure of SBA-15, **12** (7), 1961 (2000).

44 R. Ryoo, C. H. Ko, M. Kruk, V. Antochshuk, and M. Jaroniec, *Journal of Physical Chemistry B,* Block-copolymer-templated ordered mesoporous silica: Array of uniform mesopores or mesopore-micropore network?, **104** (48), 11465 (2000).

45 R. Gadiou, S. E. Saadallah, T. Piquero, P. David, J. Parmentier, and C. Vix-Guterl, *Microporous And Mesoporous Materials,* The influence of textural properties on the adsorption of hydrogen on ordered nanostructured carbons, **79** (1-3), 121 (2005).

46 R. Gadiou, N. Texier-Mandoki, T. Piquero, S. E. Saadallah, J. Parmentier, J. Patarin, P. David, and C. Vix-Guterl, *Adsorption-Journal Of The International Adsorption Society,* The influence of microporosity on the hydrogen storage capacity of ordered mesoporous carbons, **11**, 823 (2005).

47 N. Texier-Mandoki, J. Dentzer, T. Piquero, S. Saadallah, P. David, and C. Vix-Guterl, *Carbon,* Hydrogen storage in activated carbon materials: Role of the nanoporous texture, **42** (12-13), 2744 (2004).

48 X. H. Shao, W. C. Wang, R. S. Xue, and Z. M. Shen, *Journal Of Physical Chemistry B,* Adsorption of methane and hydrogen on mesocarbon microbeads by experiment and molecular simulation, **108** (9), 2970 (2004).

49 B. Z. Fang, H. S. Zhou, and I. Honma, *Journal Of Physical Chemistry B,* Ordered porous carbon with tailored pore size for electrochemical hydrogen storage application, **110** (10), 4875 (2006).

50 P. Wang and X. D. Kang, *Dalton Transactions,* Hydrogen-rich boron-containing materials for hydrogen storage, (40), 5400 (2008).

51 E. Mayer, *Inorganic Chemistry,* Symmetrical Cleavage of Diborane by Ammonia in Solution, **11** (4), 866 (1972).

52 M. G. Hu, J. M. Vanpaasschen, and R. A. Geanangel, *Journal of Inorganic & Nuclear Chemistry,* New Synthetic Approaches to Ammonia-Borane and Its Deuterated Derivatives, **39** (12), 2147 (1977).

53 J. Beres, A. Dodds, A. J. Morabito, and R. M. Adams, *Inorganic Chemistry,* Dimethyl Sulfide-Borane as a Borane Carrier, **10** (9), 2072 (1971).

54 F. H. Stephens, V. Pons, and R. T. Baker, *Dalton Transactions,* Ammonia - borane: the hydrogen source par excellence?, (25), 2613 (2007).

55 R. D. Suenram and L. R. Thorne, *Chemical Physics Letters,* Microwave-Spectrum and Dipole-Moment of Bh3nh3, **78** (1), 157 (1981).

56 L. R. Thorne, R. D. Suenram, and F. J. Lovas, *Journal Of Chemical Physics,* Microwave-Spectrum, Torsional Barrier, and Structure of Bh3nh3, **78** (1), 167 (1983).

57 T. B. Richardson, S. deGala, R. H. Crabtree, and P. E. M. Siegbahn, *Journal Of The American Chemical Society,* Unconventional hydrogen bonds: Intermolecular B-H center dot center dot center dot H-N interactions, **117** (51), 12875 (1995).

58 W. T. Klooster, T. F. Koetzle, P. E. M. Siegbahn, T. B. Richardson, and R. H. Crabtree, *Journal Of The American Chemical Society,* Study of the N-H center dot center dot center dot H-B dihydrogen bond including the crystal structure of BH3NH3 by neutron diffraction, **121** (27), 6337 (1999).

59 J. S. Li, F. Zhao, and F. Q. Jing, *Journal Of Chemical Physics,* B-H delta-sigma bond as dihydrogen bond acceptor: Some theoretical observations and predictions, **116** (1), 25 (2002).

60 D. A. Dixon and M. Gutowski, *Journal of Physical Chemistry A,* Thermodynamic properties of molecular borane amines and the [BH4-][NH4+] salt for chemical hydrogen storage systems from ab initio electronic structure theory, **109** (23), 5129 (2005).

61 S. Sakai, *Chemical Physics Letters,* A New Mechanism of H2b=Nh2 Formation in the Reaction of B2h6 with Nh3, **217** (3), 288 (1994).

62 L. Li, X. Yao, C. H. Sun, A. J. Du, L. N. Cheng, Z. H. Zhu, C. Z. Yu, J. Zou, S. C. Smith, P. Wang, H. M. Cheng, R. L. Frost, and G. Q. M. Lu, *Advanced Functional Materials,* Lithium-Catalyzed Dehydrogenation of Ammonia Borane within Mesoporous Carbon Framework for Chemical Hydrogen Storage, **19** (2), 265 (2009).

63 H. J. Himmel and H. Schnockel, *Chemistry-A European Journal,* Heats of hydrogenation of compounds featuring main group elements and with the potential for multiply bonding, **8** (10), 2397 (2002).

64 D. J. Heldebrant, A. Karkamkar, N. J. Hess, M. Bowden, S. Rassat, F. Zheng, K. Rappe, and T. Autrey, *Chemistry Of Materials,* The Effects of Chemical Additives on the Induction Phase in Solid-State Thermal Decomposition of Ammonia Borane, **20** (16), 5332 (2008).

65 I. G. Green, K. M. Johnson, and B. P. Roberts, *Journal of the Chemical Society-Perkin Transactions 2,* Homolytic Reactions of Ligated Boranes .13. an Electron-Spin Resonance Study of Radical-Addition to Aminoboranes, (12), 1963 (1989).

66 C. A. Jaska, K. Temple, A. J. Lough, and I. Manners, *Journal Of The American Chemical Society,* Transition metal-catalyzed formation of boron-nitrogen bonds: Catalytic dehydrocoupling of amine-borane adducts to form aminoboranes and borazines, **125** (31), 9424 (2003).

67 T. J. Clark, C. A. Russell, and I. Manners, *Journal Of The American Chemical Society,* Homogeneous, titanocene-catalyzed dehydrocoupling of amine-borane adducts, **128** (30), 9582 (2006).

68 Y. Luo and K. Ohno, *Organometallics,* Computational study of titanocene-catalyzed dehydrocoupling of the adduct Me2NH center dot BH3: An intramolecular, stepwise mechanism, **26** (14), 3597 (2007).

69 M. C. Denney, V. Pons, T. J. Hebden, D. M. Heinekey, and K. I. Goldberg, *Journal Of The American Chemical Society,* Efficient catalysis of ammonia borane dehydrogenation, **128** (37), 12048 (2006).

70 R. J. Keaton, J. M. Blacquiere, and R. T. Baker, *Journal Of The American Chemical Society,* Base metal catalyzed dehydrogenation of ammonia-borane for chemical hydrogen storage, **129** (7), 1844 (2007).

71 X. D. Kang, L. P. Ma, Z. Z. Fang, L. L. Gao, J. H. Luo, S. C. Wang, and P. Wang, *Physical Chemistry Chemical Physics,* Promoted hydrogen release from ammonia borane by mechanically milling with magnesium hydride: a new destabilizing approach, **11** (14), 2507 (2009).

72 A. Gutowska, L. Y. Li, Y. S. Shin, C. M. M. Wang, X. H. S. Li, J. C. Linehan, R. S. Smith, B. D. Kay, B. Schmid, W. Shaw, M. Gutowski, and T. Autrey,

Angewandte Chemie-International Edition, Nanoscaffold mediates hydrogen release and the reactivity of ammonia borane, **44** (23), 3578 (2005).

73 A. Feaver, S. Sepehri, P. Shamberger, A. Stowe, T. Autrey, and G. Z. Cao, *Journal of Physical Chemistry B,* Coherent carbon cryogel-ammonia borane nanocomposites for H-2 storage, **111** (26), 7469 (2007).

74 S. Sepehri, A. Feaver, W. J. Shaw, C. J. Howard, Q. Zhang, T. Autrey, and G. Cao, *Journal Of Physical Chemistry B,* Spectroscopic studies of dehydrogenation of ammonia borane in carbon cryogel, **111** (51), 14285 (2007).

Chapter 3 Role of Trifluoroacetic Acid, Acetic Acid and Their Salts in the Synthesis of Helical Mesoporous Materials

3.1 Introduction

Helical structures are common in nature on both microscopic and macroscopic levels. Fabricating helical structures are increasingly attractive in physics and material science (1-3) because of their potential applications in chiral catalysis and chiral recognition (4-7). With recent developments, the synthesis of helical mesostructured materials has received considerable attention. Che and her co-workers firstly reported the synthesis of helical mesoporous silica materials with chiral channels using chiral anioic surfactants as templates (4), following which numerous helical mesostructures with controlled morphology and helicity have been successfully synthesized using either chiral or achiral surfactants as templates (3,8-21). In addition, the geometrically motivated model (2), the entropically driven model (22) and also the inherent chirality of the surfactant molecules (4) have been proposed to be the driving force for the formation of helical structures. For instance, inspired by the entropically driven model, the helical mesoporous silica has been prepared using achiral cationic surfactants as templates in a highly concentrated ammonia solution (13). Yang et al. have successfully prepared inner helical mesoporous silica nanofibers (23) and twisted mesoporous silica ribbons (24) using the self-assembly of chiral cationic gelators as templates. In this process, the use of chiral templates is the key to fabricating helical mesoporous materials.

The utilization of different additives is another approach to synthesize helical mesoporous materials. With the aid of ethyl acetate in the synthetic system, chiral mesostructured silica nanofibers with single- and double-axis have been successfully fabricated (11). Recently, employing cetyltrimethylammonium bromide (CTAB) as a template and perfluorooctanoic acid (PFOA) as an additive, helical mesoporous materials were synthesized. (25) The authors proposed an interfacial interaction mechanism to understand the origin of helical mesostructures. It was suggested that the PFOA molecules could reduce the surface tension and favor the formation of helical mesostructures by reducing surface free energy. However, the helical mesostructures were obtained only in a small range of PFOA/CTAB molar ratios (~0.05-0.1) (25), possibly due to the extreme surface activity of PFOA molecules. When the PFOA/CTAB molar ratio was further increased to 0.2, the helical structure was destroyed and a complex morphology was obtained. (26)

Perfluroalkanes are surface active (27) and their ability to lower surface tensions increases with increasing chain length (28). It is therefore expected that helical mesostructures may be obtained in a wider range of additive/CTAB molar ratios if short chain perfluorinated molecular additives are used. To our knowledge, there has been no report concerning the effect of short chain perfluroalkanes or their derivatives on the formation of helical mesostructures. Moreover, in the basic synthesis conditions (25), the PFOA molecules react with sodium hydroxides in the

form of anions (25), resulting in a change in the pH of the system. This influence upon the helical mesostructure was not considered (25) and should be further investigated. It is expected that a parallel study using a perfluorocarboxyl acid, its hydrocarbon counterpart, and their salts as additives will help understand the roles of such additives in the synthesis of helical mesoporous materials.

In this chapter, trifluoroacetic acid, which has the shortest fluorocarbon- chain among all perfluorocarboxylic acid molecules, was chosen as an additive in the synthesis of helical mesoporous materials. In order to understand the effect of perfluorocarboxylic acid, carboxylic acid and also the reaction pH, acetic acid, sodium trifluoroactate and sodium acetate were further chosen as additives for the synthesis.

3.2 Experimental section

3.2.1 Synthesis

Chemicals: All chemicals including CTAB (≥96.0%, purum), trifluoroacetic acid (CF_3COOH) (reagent grade,≥98%), acetic acid (CH_3COOH) (*ReagentPlus*®, ≥99%), sodium trifluoroacetate (CF_3COONa) (purum, ≥ 98.0%), sodium acetate (CH_3COONa) (ACS reagent, ≥99.0%), sodium hydroxide (NaOH) (reagent grade, 97%) and tetraethyl orthosilicate (TEOS) (*ReagentPlus*®, ≥99%) were purchased from SIGMA-ALDRICH and were used as received without further purification.

Synthesis process: Siliceous mesoporous materials were synthesized using CTAB as the template and four derivatives of acetic acid (CF_3COOH, CH_3COOH, CF_3COONa, or CH_3COONa) were used as additives with different additive/CTAB molar ratios (R, R = 0, 0.025, 0.05, 0.1, 0.2, 0.25, 0.375, 0.5, 0.75, 1). In a typical synthesis, 0.20 g of CTAB was dissolved in 96 g of deionized water under stirring at room temperature. Then, 0.70 mL of 2.0 M NaOH and desired amount of additives were added separately into the solution. The temperature of the solution was then raised and kept at 80 °C. In this solution, 1.34 mL of TEOS was added. The mixture was stirred and kept at 80°C for 2 h. The system was cooled down to room temperature, and then the powdery products were collected by filtration and air-dried at room temperature. The products were calcined at 550 °C for 5 h to remove the template.

3.2.2 Characterization

X-ray diffraction (XRD) was carried out using a German Bruker D4 X-ray diffractometer with Ni filtered Cu Kα radiation. Transmission electron microscopy (TEM) investigations were performed in a TECNAI 12 microscope operated at 120 kV. TEM specimens were prepared by dispersing the powder-like samples in ethanol by ultrasonic for 3 min and then deposited on perforated carbon films. Nitrogen adsorption/desorption isotherms were measured at -196 °C using a Micromeritics ASAP Tristar 3000 system. The samples were degassed at 180 °C overnight on a vacuum line.

3.3 Results

3.3.1 XRD pattens

Figure 3.1a-d shows the small angle XRD patterns of calcined mesostructured silica samples synthesized using CTAB as the template and CF_3COOH, CF_3COONa, CH_3COOH, CH_3COONa as the additives at different *R* values, respectively. For samples synthesized with the addition of perfluorinated molecules with *R* values smaller than 0.2 (Figure 3.1a and 3.1b), three characteristic diffraction peaks can be clearly observed in their XRD patterns, which can be indexed to the (10), (11) and (20) diffractions of a 2-D hexagonal plane group (p6m) (29). The d-spacing values calculated from the first diffraction peaks vary only in a very small range (3.5-3.6 nm, see Table 3.1).

Table 3.1 Physicochemical properties of mesostructured silica S0-S16 synthesized using CTAB as a template and CF_3COOH or CF_3COONa as additives at different molar ratios (*R*)

Sample I D	*A*	*R*	2θ (degree)	*d* (nm)	*p* (nm)	*S* (m^2/g)	*V* (cm^3/g)
S0	-	-	2.44	3.62	1.9	495	0.41
S1	CF_3COOH	0.025	2.52	3.50	1.8	846	0.47
S2		0.05	2.48	3.56	1.9	803	0.51
S3		0.1	2.39	3.69	1.9	641	0.56
S4		0.2	2.44	3.62	1.8	573	0.46
S5		0.375	2.31	3.82	2.1	551	0.50
S6		0.5	2.28	3.87	2.2	526	0.43
S7		0.75	1.90	4.64	2.3	351	0.45
S8		1	*	*	2.9	456	0.50
S9	CF_3COONa	0.025	2.47	3.57	2.1	645	0.40
S10		0.05	2.50	3.53	2.2	672	0.41
S11		0.1	2.51	3.52	1.8	526	0.36
S12		0.2	2.49	3.54	2.0	556	0.39
S13		0.375	2.54	3.47	1.7	338	0.33
S14		0.5	2.50	3.53	1.8	204	0.19
S15		0.75	2.25	3.92	2.0	419	0.50
S16		1	2.36	3.74	2.0	494	0.35

Note: * No diffraction peaks are observed in the XRD patterns. *A* is the additive used, *R* is the molar ratio of additive/CTAB, *d* is the d-spacing calculated form the first diffraction peak in XRD patterns; *p* is the pore size calculated from the adsorption branch by the Barrett-Joyner-Halenda (BJH) method; *S* is the BET surface area; and *V* is the total pore volume measured at a relative pressure of 0.99.

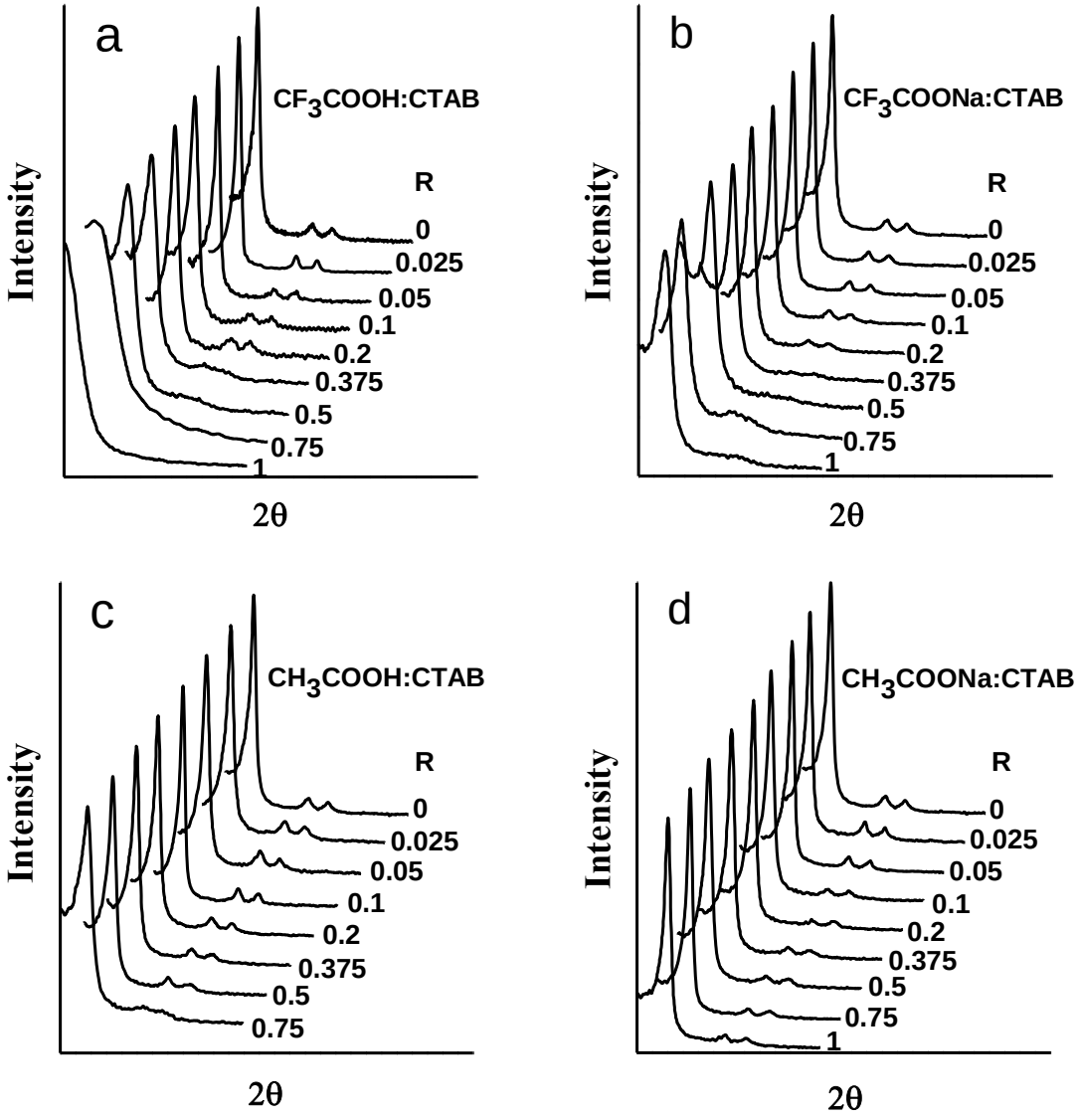

Figure 3.1 XRD patterns of calcined mesostructured silica synthesized by using CTAB as a template and (a) CF_3COOH, (b) CF_3COONa, (c) CH_3COOH and (d) CH_3COONa as additives at different molar ratios (*R*)

The difference between CF_3COOH and CF_3COONa can be seen when the additive/CTAB *R* values are increased. In the case of CF_3COOH, the (11) and (20) diffractions become broad and cannot be distinguished when *R*= 0.375 and 0.5.

When R = 0.75, even the first diffraction peak becomes broad, indicating a rather disordered mesostructure. When R is further increased to 1, no diffraction peaks can be observed, suggesting that the mesostructure is fully destroyed. In contrast, in the case of CF_3COONa, the sharp first diffraction peak still can be observed even when R = 1, however, the diffraction peaks at higher angles cannot be clearly distinguished. The above results suggest that, compared to CF_3COOH, CF_3COONa as the additive can better maintain the ordered mesostructure in the template synthesis.

When the XRD patterns of calcined silica materials synthesized by using CH_3COOH and CH_3COONa as the additives are compared (Figure 3.1c and 3.1d, respectively), it is clearly seen that all samples have highly ordered hexagonal mesostructures with three well-resolved peaks. It is noted that when the CH_3COOH/CTAB R is 1, no precipitation can be obtained. For comparison, when the CH_3COONa/CTAB R is 1, the ordered hexagonal mesostructure is still obtained (Figure 3.1d). Comparing the difference between the CF_3COOH and CH_3COOH system or CF_3COONa and CH_3COONa system, it is obvious that the fluorocarbon and hydrocarbon chain, although with difference in only three F and H atoms, have significant influence on the final self-assembled mesostructures. While the use of hydrocarbon additives such as CH_3COONa has little influence on the mesostructure in a wide range of additive/CTAB R values, the use of fluorinated additives such as CF_3COONa has a much stronger adverse influence on the mesostructure regularity at high R values (e.g., R =1)

3.3.2 TEM observations

The mesostructures of calcined silica samples templated by CTAB and different additives at various *R* values have been studied further by TEM observations. For *R* = 0 (in the absence of any additives), a MCM-41 type structure similar to that reported in literature was observed (29), which will not be discussed further in this study. For mesostructured materials synthesized with CF_3COOH/CTAB as co-templates at *R* = 0.025 and 0.05, large-area spherical and short cylindrical morphologies can be seen in Figure 3.2a and 3.2b, respectively. It is clear that increasing CF_3COOH/CTAB *R* values (from 0.025 to 0.05) leads to a transformation from spherical to rod-like morphology. The high-magnification TEM images for both samples (insets in Figure 3.2a and 3.2b) represent highly ordered hexagonal mesostructure with the straight 1-D channels viewed along the (11) directions, similar to traditional MCM-41 materials (29).

When the CF_3COOH/CTAB *R* values are further increased (*R*=0.1 and 0.2), a rod-like morphology with further increased length/diameter ratios can be obtained (Figure 3.2c and 3.2d, respectively). The helical structure can be clearly seen in all these rods and the pitch size is estimated to be ~75 and ~60 nm for the helical silica samples obtained at the CF_3COOH/CTAB *R* of 0.1 and 0.2, respectively. When the CF_3COOH/CTAB *R* is increased to 0.375, some spheres can be observed together with the rod-like morphology (Figure 3.2e). Further increasing *R* value to 0.5 results

in basically spherical particles with relatively disordered mesostructures (Figure 3.2f), consistent with the XRD observations.

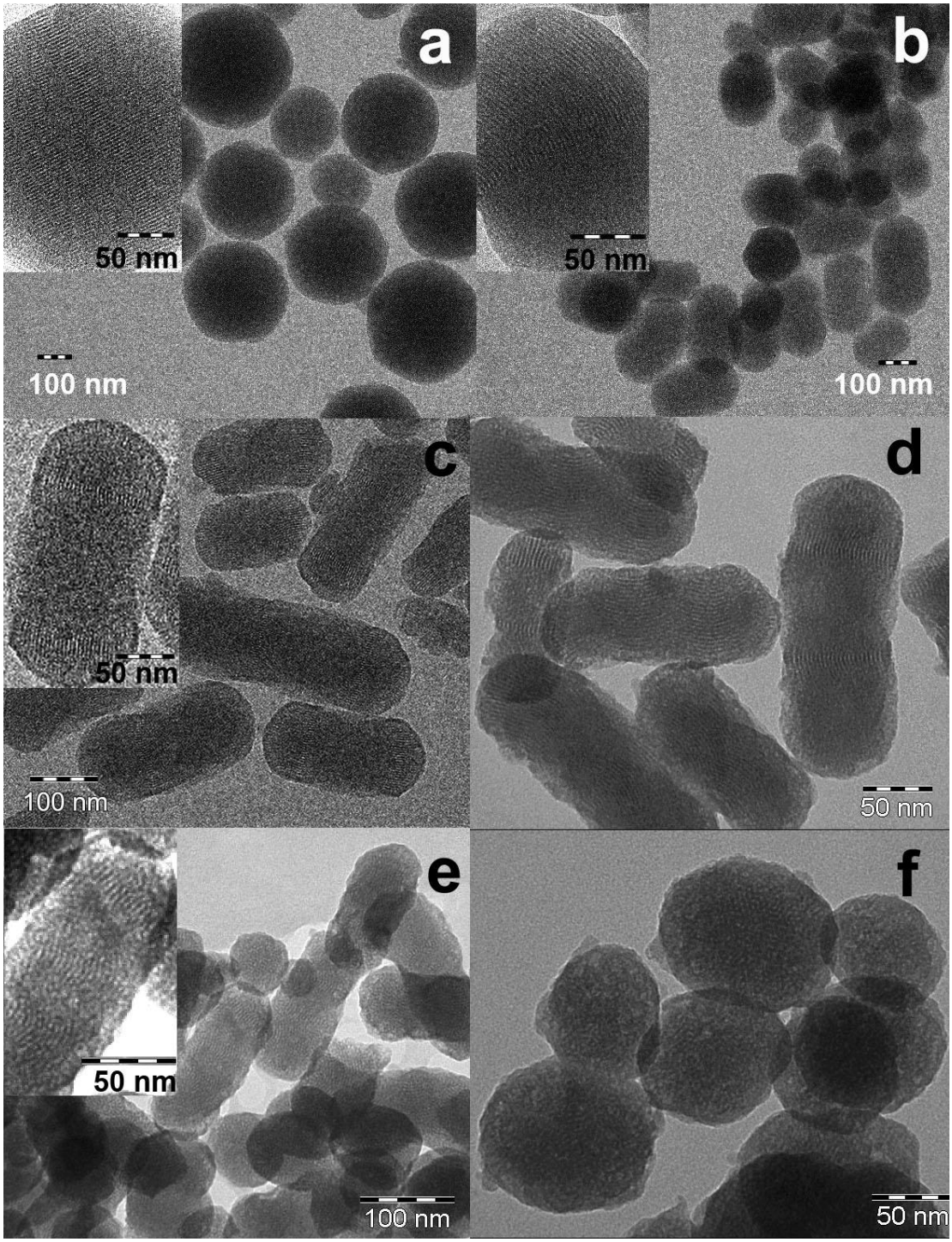

Figure 3.2 TEM images of mesostructured materials synthesized with CF_3COOH/CTAB as the co-templates at CF_3COOH/CTAB R = 0.025 (a), 0.05 (b), 0.1 (c), 0.2 (d), 0.375 (e), 0.5 (f), respectively

Typical TEM images of mesostructured materials templated by CF_3COONa/CTAB at different CF_3COONa/CTAB *R* values are shown in Figure 3.3. The spherical particles with the sizes of ~ 200 nm as well as the highly ordered hexagonal mesostructure viewed along the (01) direction can be clearly observed for the sample obtained at CF_3COONa/CTAB *R*=0.05 (Figure 3.3a). Similar to the finding in the CF_3COOH/CTAB system, increasing the CF_3COONa/CTAB *R* values leads to a morphology change from spherical particles to rods. When *R* = 0.1, 0.2, 0,375, and 0.5 (Figure 3.3b, 3.3c, 3,3d and 3.3e, respectively), it can be seen that the short cylinders are gradually getting much longer in length. The diameters of the rods decrease from ~ 100 nm (Figures 3.3b and 3.3c) to ~ 50 nm (Figures 3.3d and 3.3e) with increasing *R* values, while the length increases from ~ 300 to ~ 500 nm. Moreover, the helical structures can be obtained in a wider *R* range compared to the CF_3COOH/CTAB system. The pitch size has decreased from > 1000 nm (as judged from Figures 3.3b and 3.3c) to ~ 360 nm (Figure 3.3e) when the CF_3COONa/CTAB *R* values are increased from 0.1 to 0.5. However, when the degree of helicity is increased, less ordered hexagonal mesostructures are observed due to the symmetry breaking (e.g. *R* = 0.5, Figure 3.3e), in good agreement with the XRD results (Figure 3.1b, *R*=0.5, 0.75). When *R* is enlarged to 1, disordered domains are observed (Figure 3.3f), thus the helical mesostructure cannot be obtained at such a high CF_3COOH/CTAB *R* value.

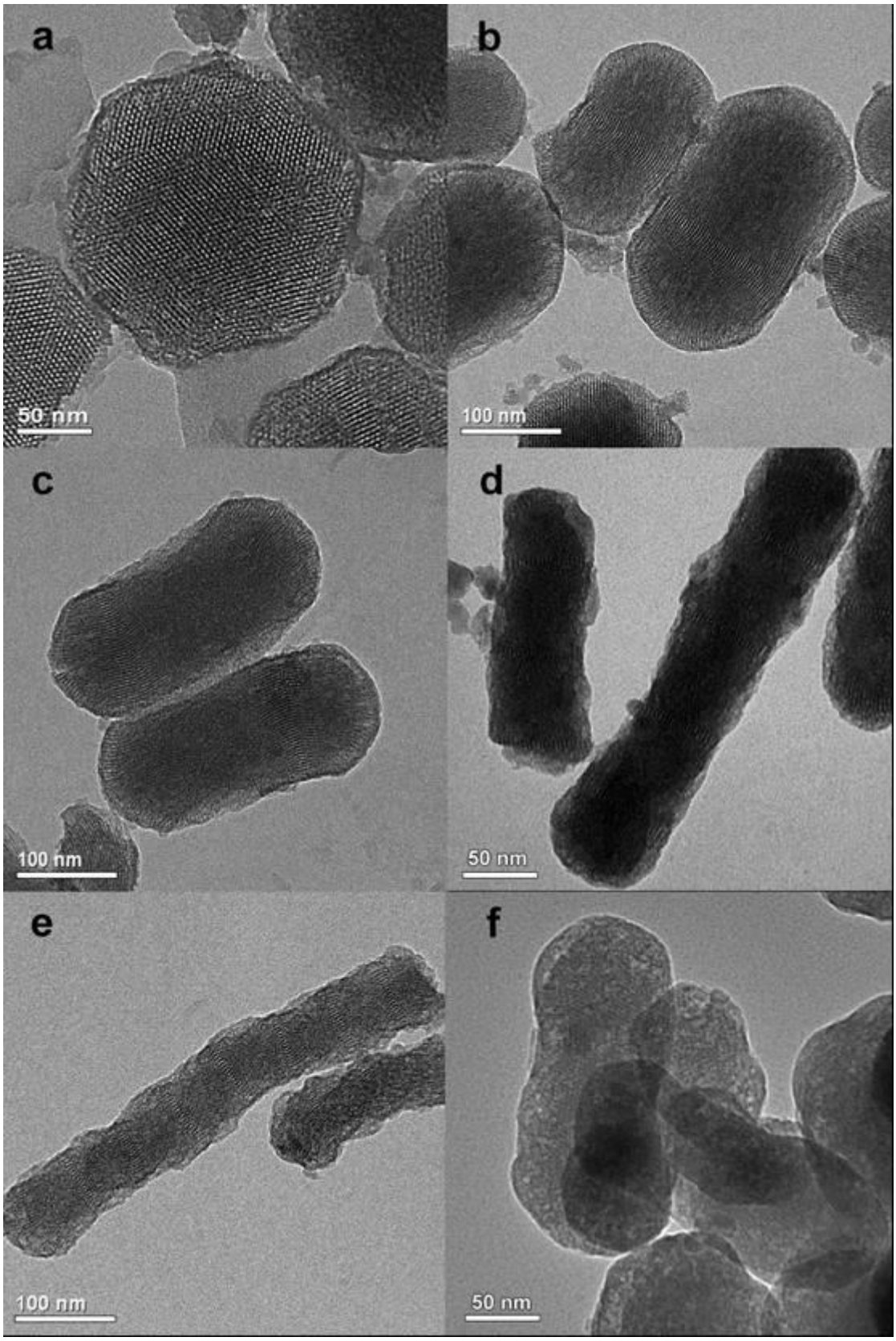

Figure 3.3 TEM images of mesostructured materials synthesized with CF_3COONa/CTAB as templates at different *R*, *R*=0.05 (a), 0.1 (b), 0.2 (c), 0.375 (d), 0.5 (e), 1 (f), respectively

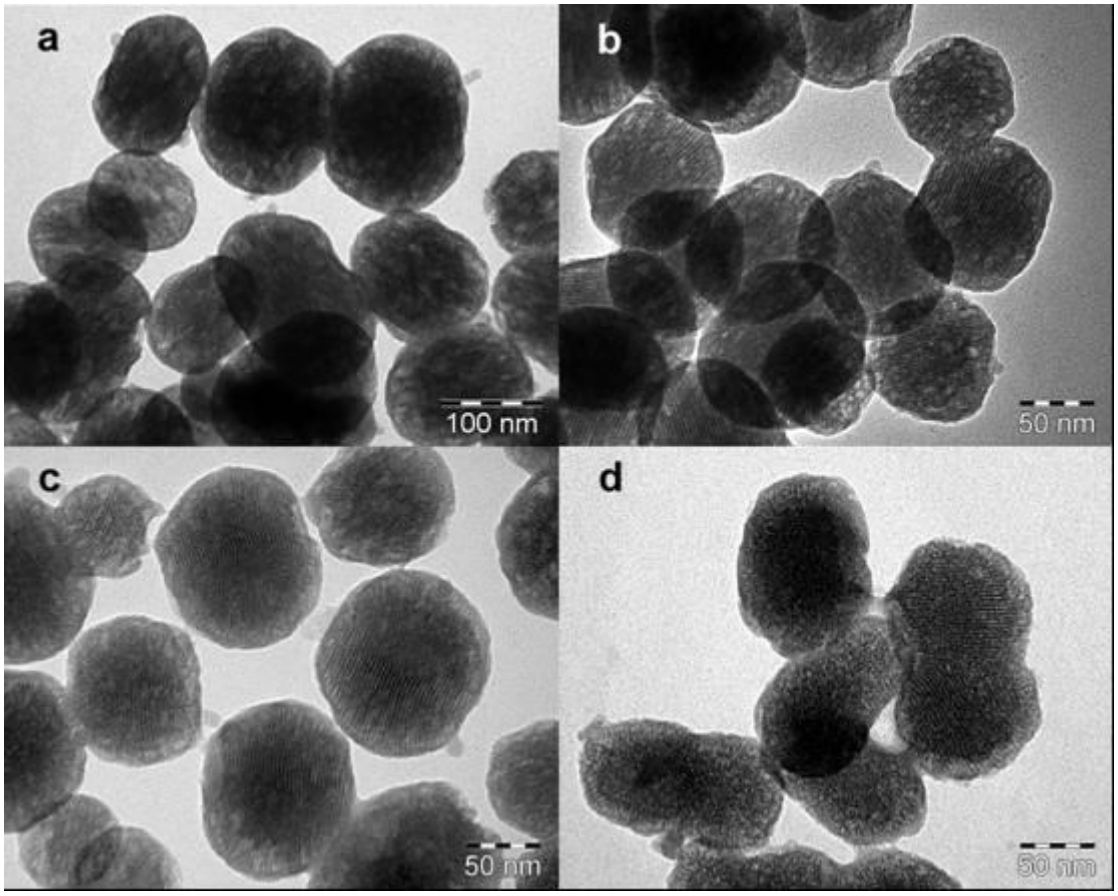

Figure 3.4 TEM images of mesostructured materials synthesized with CH_3COOH/CTAB as templates at different *R*, *R*=0.2 (a), 0.375 (b), 0.5 (c), 0.75 (d), respectively

In comparison, the samples synthesized by using CTAB as the template and CH_3COOH or CH_3COONa as the additive were also characterized by TEM and the representative images are shown in Figure 3.4 and Figure 3.5. Different from the results obtained from using CTAB/CF_3COOH or CTAB/CF_3COONa as co-templates, the morphologies, sizes and the mesostructures of siliceous materials obtained in these two systems at different additive/CTAB *R* values show little difference (Figure 3.4). The hexagonal structural regularity is reduced only slightly at a high CH_3COOH/CTAB *R* value of 0.75 (Figure 3.4d). Even when the CH_3COONa/CTAB

R value is up to 1, the highly ordered hexagonal mesostructure is still maintained, as reflected by the clearly distinguished TEM images viewed from the (11) and (01) directions (Figure 3.5), which is also consistent with the XRD pattern (Figure 3.1d). However, it is noted that no helical mesostructure can be obtained using either CH_3COOH or CH_3COONa as the additive in our studies.

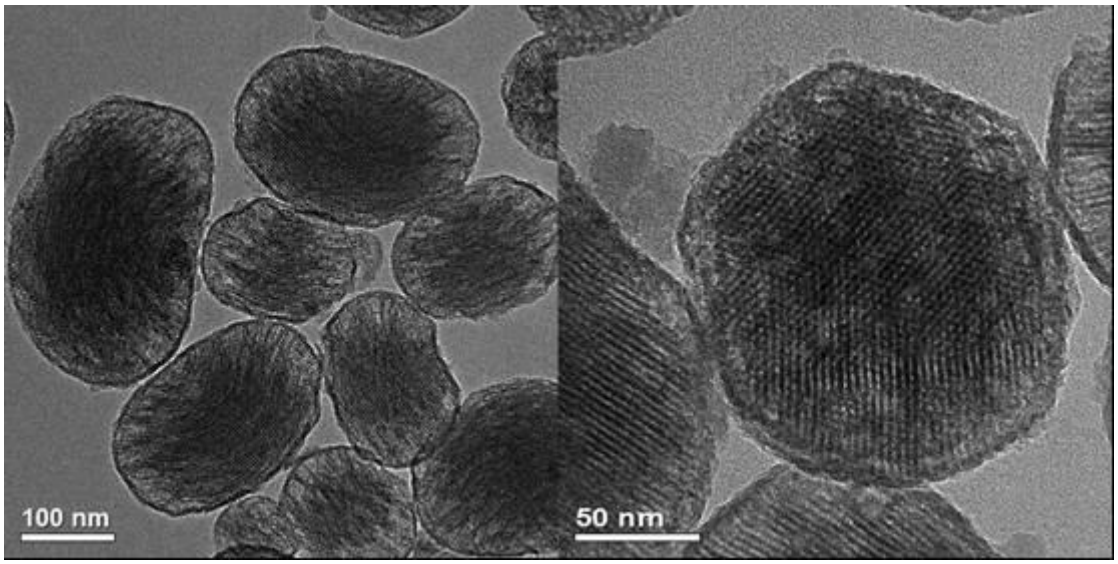

Figure 3.5 TEM images of mesostructured materials synthesized with CH_3COONa/CTAB as templates at *R*=1

The N_2 adsorption/desorption analysis was carried out to characterize the textural properties of mesoporous materials synthesized by our approach. The focus of this work is to study the formation of helical mesostructures, thus only the CF_3COOH/CTAB and CF_3COONa/CTAB templating systems are discussed and the physicochemical properties of calcined silica samples synthesized at different additive/CTAB *R* values are summarized in Table 3.1. In the CF_3COOH/CTAB

templating system, the pore sizes (calculated from the adsorption branch using the Barrett-Joyner-Halenda, BJH model (30,31)) of calcined samples with *R* values in the range of 0 - 0.375 have only a slight variation (1.8 – 2.1 nm), while when the *R* values are increased from 0.375 to 1, the gradual pore size enlargement from 2.1 to 2.9 nm is observed. However, in the CF_3COONa/CTAB templating system, the pore sizes are changed only in a small range (1.7-2.2 nm) when the CF_3COONa/CTAB *R* values are adjusted from 0 to 1. Such results are in good agreement with the XRD characterizations as discussed in the previous section.

3.4 Discussion

3.4.1 The Influence of fluorocarbon and hydrocarbon additives

In our study, all the samples were synthesized at the same conditions except that different types and amounts of additives were employed. Thus, the distinctions in the mesostructures should be induced directly by the additives. Fluorocarbon molecules are more hydrophobic and more surface active than their hydrocarbon counterparts, and can greatly reduce the surface tension of aqueous solutions (27). Moreover, a fluorocarbon chain is stiffer than a hydrocarbon chain and the van der Waals attraction between fluorocarbon chains is much stronger than that between hydrocarbon chains (32-37). In our study when the CF_3COOH and CH_3COOH system or CF_3COONa and CH_3COONa system are compared, the difference is only one CF_3 and CH_3 group. However, the additive molecular structure has distinguishable influence on the mesostructure of the self-assemblies. For example,

as can be clearly seen from the TEM images (Figure 3.2 and Figure 3.3), there is a distinct trend in the presence of fluorocarbon molecules as additives: the particle sizes generally decrease and they become longer rod-like morphologies with helical mesostrcutures with increasing additive/CTAB *R* values. Nevertheless, in the presence of CH_3COOH or CH_3COONa additives, no obvious changes either in morphologies or structures can be observed (Figure 3.4). Highly ordered hexagonal mesostructure can be obtained in a wide range of CH_3COONa/CTAB *R* values (R= 0 – 1, see Figure 3.1 and Figure 3.5), while the use of CF_3COONa as additives may decrease the mesostructure regularity beyond a certain CF_3COONa/CTAB *R* values ($R > 0.5$).

It should be noted that in the basic systems (NaOH), CF_3COOH and CH_3COOH are all ionized and exist as anions in solution. Therefore, the existed forms of the additives in solution from both the acids and their corresponding salts as precursors are the same except for a small difference in the pH of the systems (the pH influence will be discussed later). In our synthesis system, the additive anions may have electrostatic interaction with CTA^+, which will certainly affect the surfactant micelles aggregation behaviors and the micelle-templated mesostructures. It has been reported that the micelle elongation can be induced by increasing concentrations of salt and surfactant and the transition from spherical to rod-like micelles depends strongly on the nature of the counterion (38-41). The introduction of CH_3COO^- or CF_3COO^- into the CTA^+ solution will have different influences on the form of

micelles. Micellar elongation observed in the presence of CF_3COO^- anions should be attributed to the larger cross-sectional area, the higher hydrophobicity and higher stiffness of the CF_3 group compared to the CH_3 group. As a consequence, the fabrication of helical mesostructure with a rod-like morphology is facilitated in the presence of CF_3COO^- additives, rather than CH_3COO^- .

It is noted that the helical mesostructures can be obtained when CF_3COO^- anions were used as additives with an *R* range of 0.1-0.375 for CF_3COOH/CTAB and a relatively wider *R* range of 0.1-0.5 for CF_3COONa/CTAB. Recently, Yang et al. (25) proposed that the reduction in surface free energy is the driving force for the spontaneous formation of the spiral morphology. In their reports, the helical mesostructure was observed only in a very small PFOA/CTAB molar ratio of 0.05-0.1, (25,26) In our work, similar perfluorinated molecules but with the shortest fluorocarbon chains were used as additives and helical mesostructures can be successfully synthesized in a much broaden additive/CTAB molar ratio range, which offers a facilitated synthesis window and a fine control over the helical structures. It is suggested that CF_3COO^- has lower ability in the reduction of surface tension compared to PFO^- with longer flurocarbon chains, (28) thus higher amount of CF_3COO^- should be added in order to obtain the helical structures.

3.4.2 The influence of pH

The influence of the pH change caused by the addition of acid or salt additives upon the mesostructure is also investigated in our experiments. As above mentioned, the acid additives (CF_3COOH and CH_3COOH) are all ionized in basic systems and the pH decreases with increasing the amount of acid additives. In our experiments, the pH of the initial CTAB/H_2O/NaOH solution was 11.43. After the addition of CF_3COOH or CH_3COOH (additive/CTAB R = 1), the pH of both solutions decreased to 10.40. However, when CF_3COONa or CH_3COONa was added at the same additive/CTAB ratio of 1, the pH of the solutions remained nearly constant at 11.46. The pH value is one of the important factors for the cooperative self-assembly of organic–inorganic composites (42-44). The ordered hexagonal mesostructure cannot be obtained at a high acid additive/CTAB R values. For example, when the CH_3COOH/CTAB R = 1, there is no precipitation in the solution, which may be attributed to the low condensation rate of silica and relatively weaker interaction between silica oligomers and surfactants under this decreased pH. However, when the CH_3COONa/CTAB R = 1, highly ordered hexagonal structure can still be obtained (Figure 3.1 and Figure 3.5) because the use of salt-form additives does not change the solution pH. The influence of solution pH on the mesostructure is also reflected in the CF_3COOH/CTAB and CF_3COONa/CTAB templating system, where the helical mesostructure can be synthesized in a relatively smaller range (R = 0.1-0.375) for the former system, but a relatively larger range (R = 0.1-0.5) for the latter because the pH influence on the mesostructure is insignificant for this system.

When CF_3COOH is used as the additive, white precipitations can be obtained when R = 1, different from the CH_3COOH/CTAB=1 system, although the product does not have ordered mesostrucrture (Figure 3.1). At the similar additive/CTAB R, CF_3COOH and CH_3COOH should have the same influence on the reaction pH. Thus the difference should be attributed to the nature of additive molecules rather than the reaction pH. It is proposed that perfluorinated molecules have catalysis effect on the hydrolysis and condensation of silica species and further assist the cooperative self-assembly of composite mesostructures.

3.5 Conclusion

The influence of trifluoroacetic acid, acetic acid and their salts in the synthesis of helical mesoporous materials has been systematically investigated in this chapter. Helical mesostructures have been successfully obtained when CF_3COO^- anions were used as additives with an R range of 0.1-0.375 for the CF_3COOH/CTAB templating system and a relatively wider R range of 0.1-0.5 for the CF_3COONa/CTAB system. The pitch sizes of the helical mesostructures can be finely controlled by varying the additive/CTAB ratio. The results further indicate that in order to synthesize helical mesostructures in a wide window of additive/CTAB ratios, the perfluorinated salt with a short fluorocarbon chain should be used. This synthesis strategy is useful for the fabrication of helical mesostructured porous materials with adjustable pore and helical pitch sizes, which is important for their potential applications.

References

1 S. M. Yang, I. Sokolov, N. Coombs, C. T. Kresge, and G. A. Ozin, *Advanced Materials,* Formation of hollow helicoids in mesoporous silica: Supramolecular Origami, **11** (17), 1427 (1999).

2 A. Maritan, C. Micheletti, A. Trovato, and J. R. Banavar, *Nature,* Optimal shapes of compact strings, **406** (6793), 287 (2000).

3 Y. Y. Wu, G. S. Cheng, K. Katsov, S. W. Sides, J. F. Wang, J. Tang, G. H. Fredrickson, M. Moskovits, and G. D. Stucky, *Nature Materials,* Composite mesostructures by nano-confinement, **3** (11), 816 (2004).

4 S. Che, Z. Liu, T. Ohsuna, K. Sakamoto, O. Terasaki, and T. Tatsumi, *Nature,* Synthesis and characterization of chiral mesoporous silica, **429** (6989), 281 (2004).

5 T. E. Gier, X. H. Bu, P. Y. Feng, and G. D. Stucky, *Nature,* Synthesis and organization of zeolite-like materials with three-dimensional helical pores, **395** (6698), 154 (1998).

6 D. Bradshaw, T. J. Prior, E. J. Cussen, J. B. Claridge, and M. J. Rosseinsky, *Journal of the American Chemical Society,* Permanent microporosity and enantioselective sorption in a chiral open framework, **126** (19), 6106 (2004).

7 X. Yan, F. Wei, S. P. Elangovan, M. Ogura, and T. Okubo, *European Journal of Inorganic Chemistry,* [Ge9O14(OH)(12)](C6N2H16)(2)center dot H2O: A novel germanate with Ge-O helical chains formed by hydrothermal synthesis that can separate trans and cis isomers in situ, **2004** (23), 4547 (2004).

8 Y. G. Yang, M. Suzuki, H. Fukui, H. Shirai, and K. Hanabusa, *Chemistry of Materials,* Preparation of helical mesoporous silica and hybrid silica nanofibers using hydrogelator, **18** (5), 1324 (2006).

9 Y. G. Yang, M. Suzuki, S. Owa, H. Shirai, and K. Hanabusa, *Journal of the American Chemical Society,* Control of mesoporous silica nanostructures and pore-architectures using a thickener and a gelator, **129** (3), 581 (2007).

10 Y. G. Yang, M. Nakazawa, M. Suzuki, H. Shirai, and K. Hanabusa, *Journal of Materials Chemistry,* Fabrication of helical hybrid silica bundles, **17** (28), 2936 (2007).

11 B. Wang, C. Chi, W. Shan, Y. H. Zhang, N. Ren, W. L. Yang, and Y. Tang, *Angewandte Chemie-International Edition,* Chiral mesostructured silica nanofibers of MCM-41, **45** (13), 2088 (2006).

12 J. G. Wang, W. Q. Wang, P. C. Sun, Z. Y. Yuan, B. H. Li, Q. H. Jin, D. T. Ding, and T. H. Chen, *Journal of Materials Chemistry,* Hierarchically helical mesostructured silica nanofibers templated by achiral cationic surfactant, **16** (42), 4117 (2006).

13 Y. Han, L. Zhao, and J. Y. Ying, *Advanced Materials,* Entropy-driven helical mesostructure formation with achiral cationic surfactant templates, **19** (18), 2454 (2007).

14 G. L. Lin, Y. H. Tsai, H. P. Lin, C. Y. Tang, and C. Y. Lin, *Langmuir,* Synthesis of mesoporous silica helical fibers using a catanionic-neutral ternary surfactant in a highly dilute silica solution: Biomimetic silicification, **23** (8), 4115 (2007).

15 K. U. Jeong, S. Jin, J. J. Ge, B. S. Knapp, M. J. Graham, J. J. Ruan, M. M. Guo, H. M. Xiong, F. W. Harris, and S. Z. D. Cheng, *Chemistry of Materials,* Phase structures and self-assembled helical suprastructures via hydrogen bonding in a series of achiral 4-biphenyl carboxylic acid compounds, **17** (11), 2852 (2005).

16 J. G. Wang, W. Q. Wang, P. C. Sun, Z. Y. Yuan, Q. H. Jin, D. T. Ding, and T. H. Chen, *Materials Letters,* Observation of hollow helical fibers of MCM-41, **61** (23-24), 4492 (2007).

17 X. W. Wu, J. F. Ruan, T. Ohsuna, O. Terasaki, and S. N. Che, *Chemistry of Materials,* A novel route for synthesizing silica nanotubes with chiral mesoporous wall structures, **19** (7), 1577 (2007).

18 Y. G. Yang, M. Nakazawa, M. Suzuki, M. Kimura, H. Shirai, and K. Hanabusa, *Chemistry of Materials,* Formation of helical hybrid silica bundles, **16** (20), 3791 (2004).

19 X. W. Wu, H. Y. Jin, Z. Liu, T. Ohsuna, O. Terasaki, K. Sakamoto, and S. N. Che, *Chemistry of Materials,* Racemic helical mesoporous silica formation by achiral anionic surfactant, **18** (2), 241 (2006).

20 S. M. Yang and W. J. Kim, *Advanced Materials,* Helical mesostructured tubules from Taylor vortex-assisted surfactant templates, **13** (15), 1191 (2001).

21 T. Yokoi, Y. Yamataka, Y. Ara, S. Sato, Y. Kubota, and T. Tatsumi, *Microporous and Mesoporous Materials,* Synthesis of chiral mesoporous silica by using chiral anionic surfactants, **103** (1-3), 20 (2007).

22 Y. Snir and R. D. Kamien, *Science,* Entropically driven helix formation, **307** (5712), 1067 (2005).

23 Y. G. Yang, M. Suzuki, H. Shirai, A. Kurose, and K. Hanabusa, *Chemical Communications,* Nanofiberization of inner helical mesoporous silica using chiral gelator as template under a shear flow, (15), 2032 (2005).

24 Y. G. Yang, M. Suzuki, S. Owa, H. Shirai, and K. Hanabusa, *Chemical Communications,* Preparation of helical nanostructures using chiral cationic surfactants, (35), 4462 (2005).

25 S. Yang, L. Z. Zhao, C. Z. Yu, X. F. Zhou, J. W. Tang, P. Yuan, D. Y. Chen, and D. Y. Zhao, *Journal of the American Chemical Society,* On the origin of helical mesostructures, **128** (32), 10460 (2006).

26 S. Yang, X. F. Zhou, P. Yuan, M. H. Yu, S. G. Xie, J. Zou, G. Q. Lu, and C. Z. Yu, *Angewandte Chemie-International Edition,* Siliceous nanopods from a compromised dual-templating approach, **46** (45), 8579 (2007).

27 K. Wang, G. Karlsson, M. Almgren, and T. Asakawa, *Journal of Physical Chemistry B,* Aggregation behavior of cationic fluorosurfactants in water and salt solutions. A cryoTEM survey, **103** (43), 9237 (1999).

28 A. F. Thunemann, *Langmuir,* Complexes of polyethyleneimine with perfluorinated carboxylic acids: Wettability of lamellar structured mesophases, **16** (2), 824 (2000).

29 C. T. Kresge, M. E. Leonowicz, W. J. Roth, J. C. Vartuli, and J. S. Beck, *Nature,* Ordered Mesoporous Molecular-Sieves Synthesized by a Liquid-Crystal Template Mechanism, **359** (6397), 710 (1992).

30 P. J. Branton, P. G. Hall, K. S. W. Sing, H. Reichert, F. Schuth, and K. K. Unger, *Journal of the Chemical Society-Faraday Transactions,* PHYSISORPTION OF ARGON, NITROGEN AND OXYGEN BY MCM-41, A MODEL MESOPOROUS ADSORBENT, **90** (19), 2965 (1994).

31 R. Schmidt, E. W. Hansen, M. Stocker, D. Akporiaye, and O. H. Ellestad, *Journal of the American Chemical Society,* PORE-SIZE DETERMINATION OF MCM-41 MESOPOROUS MATERIALS BY MEANS OF H-1-NMR SPECTROSCOPY, N-2 ADSORPTION, AND HREM - A PRELIMINARY-STUDY, **117** (14), 4049 (1995).

32 S. L. Hsu, N. Reynolds, S. P. Bohan, H. L. Strauss, and R. G. Snyder, *Macromolecules,* STRUCTURE, CRYSTALLIZATION, AND INFRARED-SPECTRA OF AMORPHOUS PERFLUORO-NORMAL-ALKANE FILMS PREPARED BY VAPOR CONDENSATION, **23** (21), 4565 (1990).

33 D. Jacquemain, S. G. Wolf, F. Leveiller, F. Frolow, M. Eisenstein, M. Lahav, and L. Leiserowitz, *Journal of the American Chemical Society,* CORRELATION BETWEEN OBSERVED CRYSTALLINE SELF-ASSEMBLY OF FLUOROCARBON AND HYDROCARBON AMPHIPHILES AT THE AIR-WATER-INTERFACE AND CALCULATED LATTICE ENERGY - DETERMINATION OF ELECTROSTATIC PROPERTIES OF THE CF2 GROUP FROM A LOW-TEMPERATURE X-RAY-DIFFRACTION STUDY OF PERFLUOROGLUTARAMIDE, **114** (25), 9983 (1992).

34 S. Shin, N. Collazo, and S. A. Rice, *Journal of Chemical Physics,* A MOLECULAR-DYNAMICS STUDY OF THE PACKING STRUCTURES IN MONOLAYERS OF PARTIALLY FLUORINATED AMPHIPHILES, **96** (2), 1352 (1992).

35 S. W. Barton, A. Goudot, O. Bouloussa, F. Rondelez, B. H. Lin, F. Novak, A. Acero, and S. A. Rice, *Journal of Chemical Physics,* STRUCTURAL TRANSITIONS IN A MONOLAYER OF FLUORINATED AMPHIPHILE MOLECULES, **96** (2), 1343 (1992).

36 H. G. Cho, H. L. Strauss, and R. G. Snyder, *Journal of Physical Chemistry,* Infrared-Spectra and Structure of Perfluoro-Normal-Alkanes Isolated in Normal-Alkane Matrices Prepared by Vapor-Deposition, **96** (13), 5290 (1992).

37 C. Chothia, *Nature,* Hydrophobic Bonding and Accessible Surface-Area in Proteins, **248** (5446), 338 (1974).

38 E. W. Anacker and H. M. Ghose, *Journal of the American Chemical Society,* COUNTERIONS AND MICELLE SIZE .2. LIGHT SCATTERING BY SOLUTIONS OF CETYLPYRIDINIUM SALTS, **90** (12), 3161 (1968).

39 G. Porte, J. Appell, and Y. Poggl, *Journal of Physical Chemistry,* EXPERIMENTAL INVESTIGATIONS ON THE FLEXIBILITY OF

ELONGATED CETYLPYRIDINIUM BROMIDE MICELLES, **84** (23), 3105 (1980).

40 A. L. Underwood and E. W. Anacker, *Journal of Colloid and Interface Science,* COUNTERION LYOTROPY AND MICELLE FORMATION, **117** (1), 242 (1987).

41 A. L. Underwood and E. W. Anacker, *Journal of Colloid and Interface Science,* ORGANIC COUNTERIONS AS PROBES OF THE MICELLAR SURFACE, **117** (1), 296 (1987).

42 C. J. Brinker and G. W. Scherer, *Sol–gel Science*. (Academic Press, London, 1990).

43 H. P. Lin and C. Y. Mou, *Accounts of Chemical Research,* Structural and morphological control of cationic surfactant-templated mesoporous silica, **35** (11), 927 (2002).

44 X. G. Cui, W. C. Zin, W. J. Cho, and C. S. Ha, *Materials Letters,* Nonionic triblock copolymer synthesis of SBA-15 above the isoelectric point of silica (pH=2-5), **59** (18), 2257 (2005).

Chapter 4 Controlled Evolution from Multilamellar Vesicles to Hexagonal Mesostructures through the Addition of 1,3,5-trimethylbenzene

4.1 Introduction

Mesoporous materials have opened many new possibilities for applications in catalysis, separation, and nanoscience due to their large, controllable pore sizes and high surface areas (1-9). The pore structure, such as channel connectivity and pore symmetry, of mesoporous materials is one of the most important physical parameters for practical applications, and must be designed depending on their desired applications (10-12). Therefore, the adjustable assembly of porous silica materials with different structures and tunable pore sizes has attracted increasingly scientific attention in this field (13).

Controlling the cooperative self-assembly of organic–inorganic composites is one key factor in the preparation of mesoporous materials. Generally, the inorganic/surfactant mesophase can be explained and predicted by the effective hydrophilic-hydrophobic volume balance in the context of the classical micellar packing parameter (g), $g = V/a_0 l$, where V is the total volume of the hydrophobic surfactant chain, a_0 is the effective hydrophilic headgroup area at the aqueous-micellar surface, and l is the kinetic surfactant tail length (14,15). According to this model, various methods have been used to control the organization of mesostructures and achieve structural transitions, such as varying reaction temperatures (16,17), pH value (18-21), compositions of reaction mixtures (13), and use of different kinds of

templates from ionic surfactants to block copolymers to mixtures of surfactants (10,22,23).

The introduction of organic cosolvents into a synthesis system has been shown to form 3D architectures of mesostructured materials (24-27). Through adjusting the amount of an anionic co-template and the volume of a swelling agent such as 1,3,5-trimethylbenzene (TMB) in a triblock copolymer $EO_{106}PO_{70}EO_{106}$ (denoted Pluronic F127, where EO is polyethylene oxide and PO is polypropylene oxide) templating system, highly ordered mesostructured silica with 2-D hexagonal *p6m* or cubic *Im-3m*, *Fm-3m,* and *Ia-3d* structures in high purity can be easily obtained (22). However, TMB can not only behave as a swelling agent to enlarge the pore sizes of ordered mesoporous materials, but also induce a phase transformation from the highly ordered *p6m* mesostructure to remarkable mesostructured cellular foams (MCFs) when a large amount of TMB was added before the addition of silica source (28). The formation of microemulsion has been experimentally confirmed (28-30). Therein, an oil-in-water microemulsion consisted of TMB droplets coated by $EO_{20}PO_{70}EO_{20}$ (denoted Pluronic P123) is formed in aqueous HCl solution. When the silica source is added to this system, it will hydrolyze and condense at the surface of microemulsion droplets to give MCFs.

It should be noted that the time to add organic cosolvents during the synthesis has shown to bring diverse results. Fan and co-workers reported the synthesis of a 3D-

SBA-15 in the presence of Pluronic P123 as a template with the average mesostructure of hexagonal plane group *p6m*, which was produced by a high-temperature hydrothermal process after the introduction of TMB into "embryonic" mesostructured materials (31). In their method, TMB was added after the embryonic mesostructure had been formed. The best time for the addition of TMB was 65 min after the reaction started (31). However, after the formation of "embryonic" mesostructure, the influence of the time of TMB addition into the system upon the final composite structure has not been reported. Understanding the effect of the time of organic cosolvents addition on the embryonic mesostructure may provide a simple method for the designable synthesis of novel porous materials.

Recently, the synthesis of siliceous vesicular materials has also attracted much attention. By combining the vesicle templating (using organic vesicles as templates for silica deposition) (32) with liquid crystal templating (using the liquid crystalline phases of surfactants to develop mesostructured silica networks) (33-37), other novel pore structure are expected to form (38). However, the transition from uni- or multilamellar vesicles to highly ordered mesostructures is yet to be fully understood. Yuan et al. (23) reported a structure evolution from a highly ordered 2-D hexagonal mesostructure to multilamellar vesicles with sharp edges by increasing the molar ratio of PFOA/P123 (where PFOA is perfluorooctanoic acid). Therein, different amounts of PFOA were introduced before the addition of tetraethyl orthosilicate (TEOS) as a silica source. It was proposed that, before the presence of TEOS in the

system, PFOA interacted with PEO moiety to adjust the hydrophilic/hydrophobic volume ratio (V_H/V_L), leading to mesostructures with increased packing parameter values.

In this chapter, the effect of addition time of TMB into the synthesis system after embryonic SBA-15 mesostructure formed has been systematically studied. Previously, the time that TMB was added was measured immediately after the addition of TEOS into nonionic block copolymer (Pluronic P123) solution (31). However, a slight variation in acidity, temperature and the concentration of silica source or P123 will change the precipitation time (the precipitation is regarded as the formation of SBA-15 embryonic mesostructure). Therefore, in our study, the addition time of TMB was measured from the time precipitation was observed. Using the same amount of TMB but added at different times (t = 2, 10, 15, 20, 25, and 30 min, respectively), a structure evolution from multilamellar vesicles to a highly ordered 2-D hexagonal mesostructure was observed. The formation of multilamellar vesicles from the addition of TMB in this system has not been reported. Our results suggest that a change in the TMB addition time could induce a change in the reaction mechanism and templating pathways, which provides valuable supplements to the current understandings. The resultant siliceous materials with various pore structures can be useful candidates for catalysis, separation and as microcapsules for controlled release/delivery carriers.

4.2 Experimental

4.2.1. Synthesis

All chemicals are commercially available and were purchased from Sigma-Aldrich and used as received without further purification. The chemicals include nonionic triblock copolymer Pluronic P123 (average molar weight ~5800), TEOS (*ReagentPlus*®, ≥ 99%), TMB (puriss., ≥ 99.0%), potassium chloride (KCl) (SigmaUltra ≥99.0%), and hydrochloric acid (HCl) (ACS reagent 37%). Deionized water was used in all experiments.

In a typical synthesis, 2.0 g of P123 and 2.2 g of KCl were dissolved in 60 mL of 2.0 M HCl at 38 °C. To this solution, 4.2 g of TEOS was added under vigorous stirring. Subsequently, 1.0 g of TMB was added at different times (t) after white precipitates were observed in the solution. The mixture was stirred at the same temperature for 24 h, followed by a hydrothermal treatment at 130°C for an additional 24 h. The solid products were collected by filtration, washed with deionized water, and dried in air at room temperature. The templates were removed by calcination at 550°C for 5 h in air. The final samples obtained at t = 2, 10, 15, 20, 25, 30 min were denoted S1 - S6, respectively.

4.2.2. Characterization

X-ray diffraction (XRD) measurements were performed on a Bruker D4 ENDEAVOR diffractometer, using Ni-filtered with Cu Kα radiation (40 mA, 40 kV,

1° (2θ) min^{-1}). Nitrogen adsorption/desorption isotherms were recorded on a Micromeritics Tristar ASAP 3000 system. The calcined samples were degassed at -196°C overnight on a vacuum line prior to analysis. Transmission electron microscopy (TEM) measurements were recorded on a TECNAI 12 microscope operated at 120 kV. The sample particles were suspended in ethanol by ultrasonic for 3 min in the ultrasonic machine (type: FXP10DH) and the suspension was deposited on a copper grid coated with a polymer supported film and carbon. A JEOL 6400 microscope operated at 5 kV was used for scanning electron microscopy (SEM).

4.3. Results

4.3.1. XRD patterns- structural transition with the different addition time of TMB

The small angle XRD patterns of calcined samples S1-S6 are shown in Figure 4. 1. When TMB was added soon after the precipitates occurred in solution (S1, S2, t = 2, 10 min), no diffraction peaks can be observed in the XRD patterns, indicating the lack of ordered mesostructures in these samples. When t is ≥ 15 min (S3-S6), three characteristic diffraction peaks are observed in the XRD pattern, which can be indexed as (10), (11) and (20) diffractions of a 2-D hexagonal plane group (*p6m*) (2). The diffraction peaks are more well-defined in sample S6. The *d*-spacing of the first diffraction peak d(10) of S3-S6 can be determined from the XRD patterns and is listed in Table 4.1. The lattice parameter *a* based on the *p6m* plane group for S3-S6 can be calculated as 15.0, 13.2, 12.7, 11.5 nm, respectively. A general trend in XRD patterns reveals that when the time delay for TMB addition is increased, the structure

changes from disordered (t = 2, 10 min) to ordered hexagonal mesostructure (t =15 - 30 min). Furthermore, the lattice parameter in S3-S6 continuously decreases from 15.0 to 11.5 nm as t increases from 15 to 30 min.

Table 4.1 Structure characteristics of mesostructured silica S1-S6 synthesized at different conditions

Sample I D	t (min)	d (nm)	p (nm)	S (m^2/g)	V (cm^3/g)
S1	2	-*	-	293	1.09
S2	10	-	-	231	1.27
S3	15	12.9	18.1	284	1.07
S4	20	11.4	18.0	321	1.12
S5	25	11.0	18.1	326	1.12
S6	30	10.0	18.2	337	1.23

* No diffraction peaks are observed in the XRD patterns; t is the time at which TMB was added since the precipitates occurred in solution; d is the d-spacing calculated form the first diffraction peak in XRD patterns; p is the pore size calculated from the adsorption branch by the Barrett–Joyner–Halenda (BJH) method; S is the BET surface area; and V is the total pore volume measured at a relative pressure of 0.99.

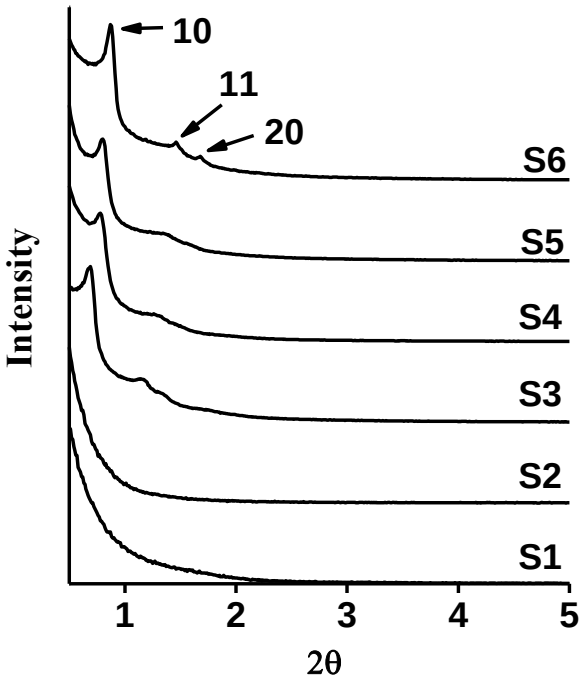

Figure 4.1: XRD patterns of the calcined mesostructured silica S1-S6.

4.3.2. Structural and morphological evolution

TEM images of S1-S6 (Figures 4.2 and 4.3) further elucidate the structural transition in S1- S6. As can be seen from Figures 4.2a and 4.2b, S1 and S2 have a multilamellar and multilamellar vesicular structure, respectively. The sizes of multilamellars in S2 are not uniform and the distance between two adjacent layers ranges from 20 to 40 nm (Figure 4.2b), similar to that in multilamellar structure of S1. The TEM image of S3 exhibits a mixture of multilamellar vesicle and hexagonal mesostructure (Figure 4.2c). The white arrow indicates the multilamellar vesicle structure and the distance between two adjacent layers is relatively smaller and more uniform (~ 20 nm) compared with S1 and S2. The black arrows show the hexagonal mesostructure and the d-spacing measured from the TEM image is 13 nm, which is

consistent with the value calculated from the XRD data. When increasing *t* to 20 min, large area of ordered hexagonal mesostructure can be seen along (01) zone axis. The lattice parameter *a* is measured to be 13 nm, which is also in good agreement with XRD results. However, a small amount of multilamellar vesicle structures can still be seen along side with the hexagonal structure, as indicated by the black arrow in Figure 4.2d.

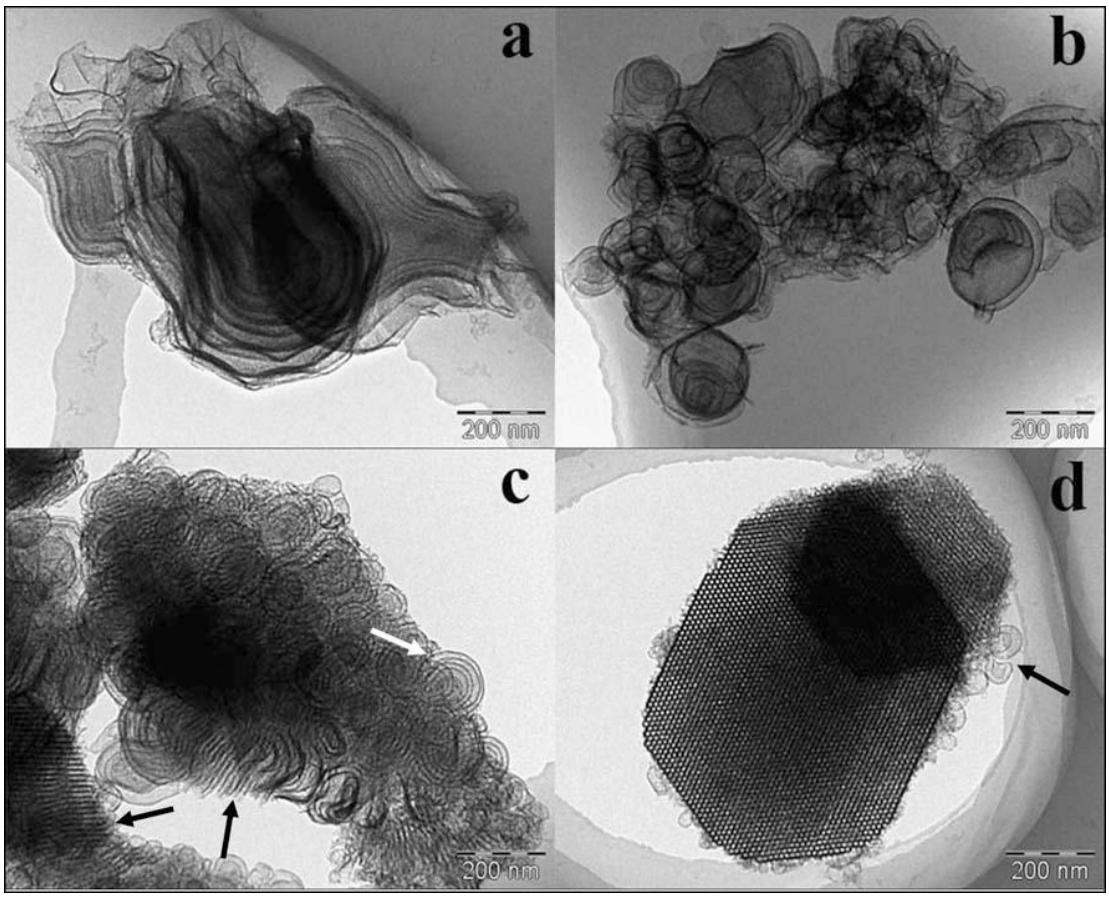

Figure 4.2: TEM images (a, b, c, d) of the calcined products S1-S4.

When t is further increased (t = 25, 30 min), the multilamellar vesicle structure gradually disappears while the hexagonal structure is maintained. For S5, TEM observations at a relatively low magnification show that only a small amount of multilamellar vesicle structures exist, while the majority of samples have an ordered hexagonal mesostructure (Figure 4.3a). Figure 4.3b is a large-area TEM image of calcined sample S6 showing the general information and Figures 4.3c and 4.3d are the high-magnification TEM images taken from (01) and (10) axis, respectively, demonstrating the representative structures. The measured d-spacing is ~ 10 nm, which is also in accordance with XRD observation. It is noted that no multilamellar vesicle structure can be found in S6. The TEM images clearly demonstrate the gradual structural transition from a multilamellar vesicle to hexagonal structure induced by the different time of TMB addition to embryonic SBA-15 materials.

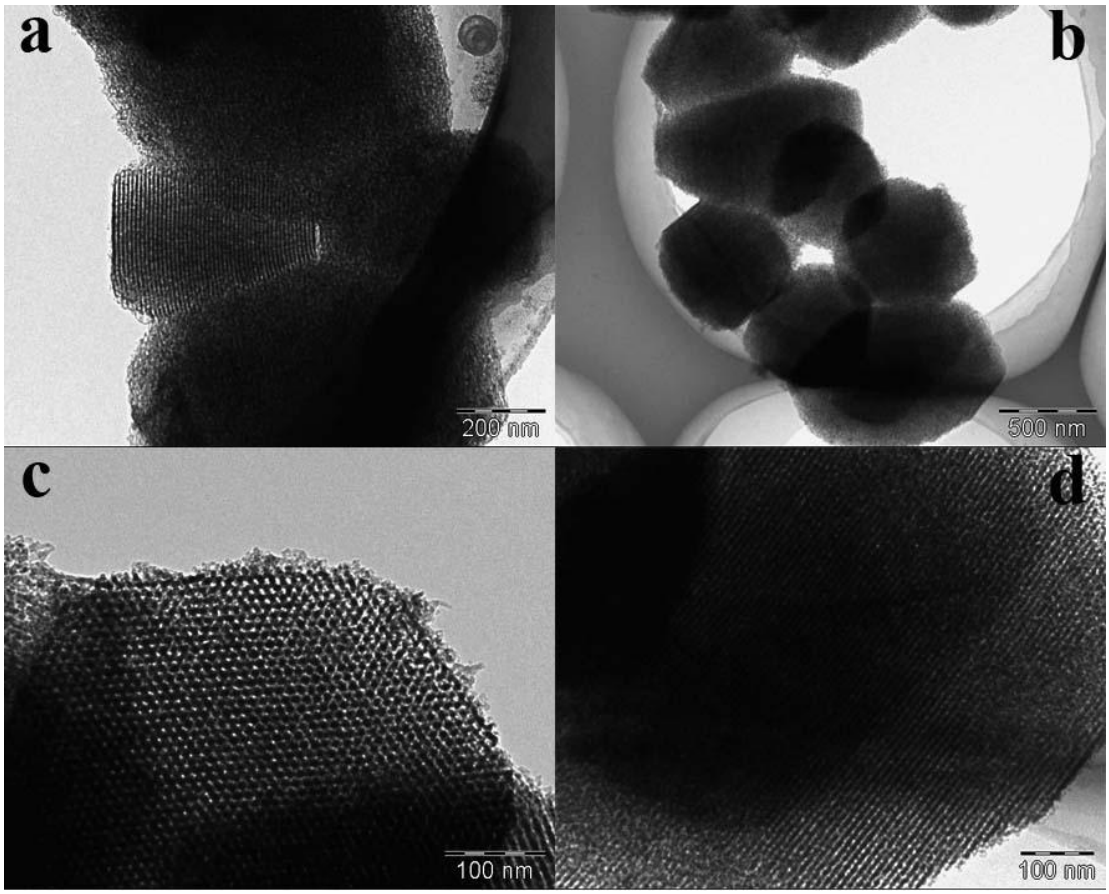

Figure 4.3: TEM images (a) and (b - d) of the calcined products S5 and S6.

SEM images displaying typical morphologies of S1-S6 are shown in Figure 4.4. With increasing *t*, the morphology changes from irregular shapes (Figure 4.4a) to hollow spheres (Figure 4.4b) and then to aggregates of small nanoparticles (Figure 4.4c), finally to solid particles with regular shapes and some facets (Figure 4.4d-f). It should be noted that the morphology of S4-S6 is similar and the particle sizes are ranging from 500 nm to 1μm (Figures 4.4d-f), which indicates that when *t* is longer than 20 min, the morphology of resultant materials will not be greatly affected.

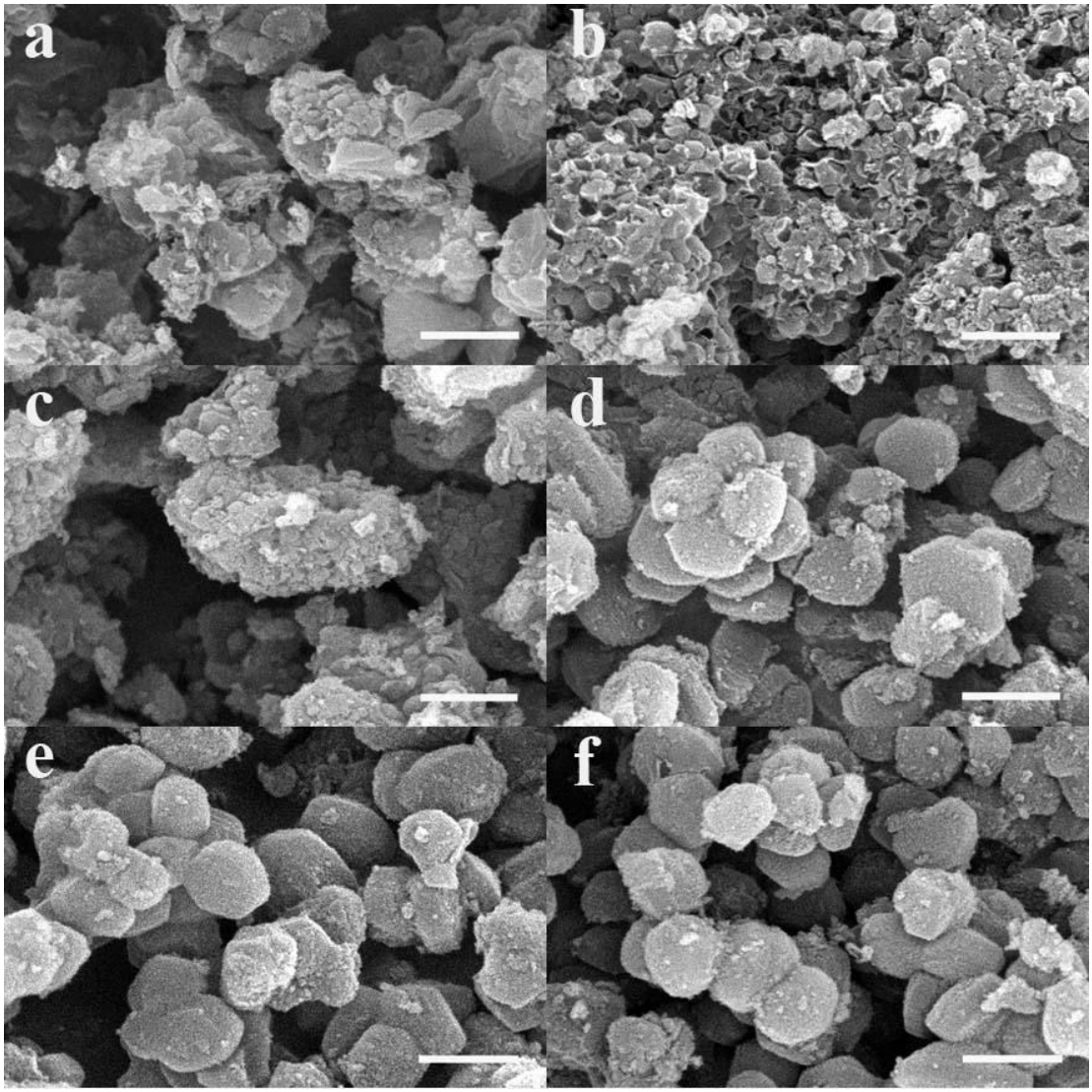

Figure 4.4: SEM images (a, b, c, d, e, f) of the calcined products S1-S6. Scale bar is 1μm in all the images.

4.3.3. N_2 Adsorption/Desorption Isotherms - Texture Properties

Figures 4.5a and 4.5b show the N_2 adsorption/desorption isotherms and the pore size distribution curves calculated from the adsorption branch using the Barrett-Joyner-Halenda (BJH) model (39) of calcined samples S1-S6, respectively. The values of the surface area, pore size, and pore volume of siliceous samples can be determined

based on the N_2 adsorption/desorption data, which are also listed in Table 4.1 for comparison. S1 and S2 exhibit Type II isotherms and the capillary condensation steps occur at a high relative pressure (P/P_0 > 0.9), indicative of porous materials consisting large voids surrounded by a mesoporous matrix (40) or hollow particles with mesoporous walls (41-43). In fact, TEM images (Figures 4.2a, 4.2b) confirm that S1 and S2 have multilamellar and multilamellar vesicle structure, respectively, which agrees with the results obtained from N_2 adsorption/desorption isotherms. Moreover, the broad pore size distribution curves of S1 and S2 are also in agreement with the structures as shown in Figures 4.2a and 4.2b. S4-S6 exhibit Type IV isotherms with Type H1 hysteresis loops. The steep capillary condensation step occurs at approximately the same position (P/P_0=0.83-0.92) and the pore diameters of S4-S6 can be calculated to be ~ 18.1 nm in the three samples. The isotherm of S3 is intervenient between Type II and Type IV. The steep capillary condensation of S3 started at P/P_0=0.83, which is similar to those observed in S4-S6. The adsorption and desorption branches cross at ~ P/P_0=1, showing the similar feature to that of S1-S2. The pore size distribution curve of S3 is slightly broader than that of S4-S6. The above observation is consistent with the TEM results: S3 is in the middle of the structural transition from multilamellar vesicle to hexagonal and thus a mixture of two structures.

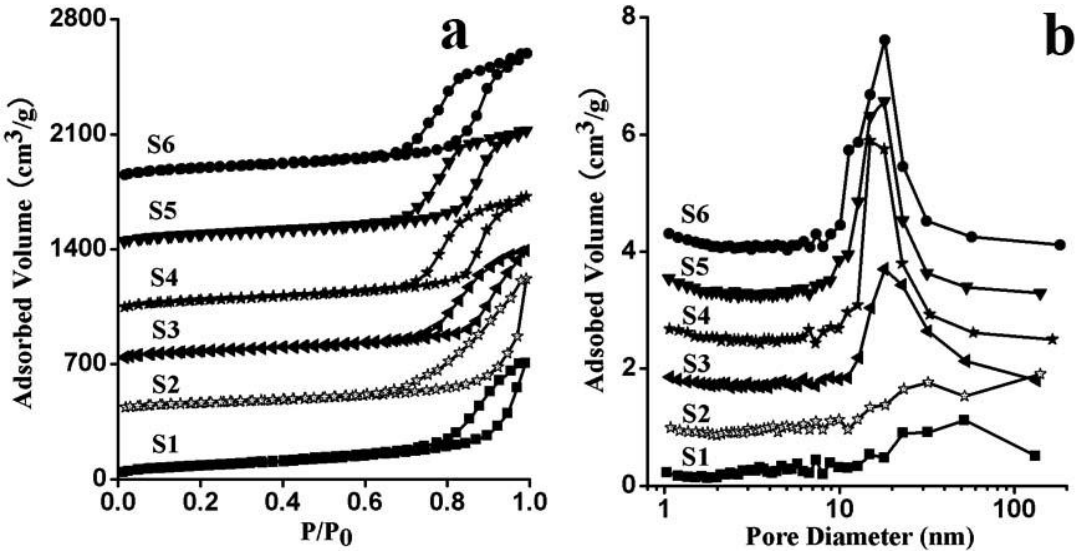

Figure 4.5: (a) Nitrogen adsorption and desorption isotherm plots, (b) the pore size distribution curves of the calcined products S1-S6. The Y-axes value of sample S2 - S6 is raised 400, 700, 1000, 1400, and 1800 cm^3/g, respectively (a), and 0.6, 1.2, 1.8, 2.4, 3.0 cm^3/g, respectively (b).

4.4. Discussion

MCFs were demonstrated to form through an oil-in-water microemulsion templating approach (28-30). Our synthesis system is similar to that for the preparation of MCFs. The only difference is that the TMB is added after the silica source is added and the embryonic SBA-15 is formed. As no MCFs can be seen in any of our samples S1- S6, it suggests that this simple change of TMB addition sequence has prevented the formation of microemulsions. Instead, multilamellar vesicle and hexagonal structures observed in these samples signify a vesicular templating and liquid crystal templating mechanism in our study.

Highly ordered mesoporous materials can be synthesized by liquid crystal templating approach where preformed liquid crystal phases in very concentrated surfactant solutions direct the inorganic-organic composite structure (33). They can also be obtained in dilute surfactant solutions, where cooperative interactions between polymer moieties and siliceous species leads to ordered mesostructures with liquid-crystal-like arrays (36). In this approach, the existence of a liquid crystal phase is not necessary. This is also the case in the cooperative vesicular templating process (44).

From a different angle, all our samples S1-S6 were synthesized at conditions similar to those used for the preparation of traditional SBA-15 (37) except that TMB was added into the embryonic SBA-15 at different times. The starting surfactant concentration is ~ 3% wt. No surfactant liquid crystalline phases exist in the system. In the absence of TMB, PEO moieties of P123 interact with siliceous species through hydrogen bonding and P123/silica composites are inclined to cooperatively self-assemble into hexagonal mesostructure, which is the accepted formation mechanism of SBA-15 (37). However, at the time the embryonic SBA-15 is formed, siliceous species with low degree of condensation at the initial stage of aggregation are soft and susceptible to structural changes (45-47). Therefore, TMB can still penetrate through the soft silica wall and enter into the PPO moieties to increase packing parameter of the composite material, leading to lamellar structures rather than conventional hexagonal SBA-15 materials. Moreover, the interaction between

siliceous species and PEO moieties in embryonic SBA-15 may prevent the formation of P123/TMB microemulsions and MCF materials at this stage. The formation of multilamellar vesicle structures can be viewed as a result of bending of lamellar structures to closed vesicles to decrease the line tension (48). The above explanation fits well with the multilamellar and multilamellar vesicle structures observed in S1 and S2 samples (Figures 4.2a and 4.2b).

When TMB is added at $t \geq 15$ min, the extended time of condensation of siliceous species leads to a relatively rigid silica wall, which makes it more and more difficult for the TMB to enter into the PPO moieties. As a result, the d-spacing determined from the first diffraction peak in S3-S6 continuously decreases with increasing delay time in TMB addition (see Table 4.1). Further, a structural transition from multilamellar vesicle to hexagonal structure can be seen in samples S3-S6. While S3 is still a mixture of multilamellar vesicle and hexagonal structures, less and less multilamellar vesicle phase is observed in S4 and S5. When *t* reaches 30 minutes, only hexagonal mesostructure is observed (S6), indicating that the addition of TMB at this time has no effect on structural transition from hexagonal to multilamellar vesicle structures. From Table 4.1, it is also noted that samples S3-S6 have a similar pore size of ~ 18 nm, which is larger than the cell parameter of hexagonal mesostructure. Such phenomenon has been observed before by Fan and co-workers (31), indicating that the calculated pore size by BJH method does not correspond to

the diameter of the cylindrical channel, but a reflection of the 3D-SBA-15 complex pore structures.

The results show that the time to add TMB is a key factor for the structure evolution from multilamellar vesicle to hexagonal mesostructures. Through this work, it is shown that the cooperative templating approaches are very sensitive. Not only the surfactant templates and inorganic species are important in determining the self-assembled structure, but also the addition of organic cosolvent and the addition time can significantly influence the reaction mechanism and the final structure of the product materials.

4.5. Conclusions

The work presented in this chapter demonstrates that a change in TMB addition time to a nonionic block copolymer templating system has caused a phase transformation from multilamellar vesicles to an ordered hexagonal mesostructure in the synthesis of mesoporous materials. While TMB has been used to facilitate the formation of a microemulsion template and as a swelling agent for mesostructured materials, it is used in our work as an agent to change the packing parameter of cooperatively self-assembled mesostructured or vesicular materials. A significant implication of our work is that, through simple manipulation of the addition sequence as well as the addition time of organic cosolvents, the self-assembly processes can be tuned among microemulsion templating, cooperative vesicular templating and cooperative liquid

crystal templating, from which complex inorganic materials with different but tunable pore structures can be obtained with the same synthesis system. The findings may pave the way for a facile approach to the synthesis of versatile porous materials of different structures, which have potential applications in catalysis, immobilization and controlled release of large biomolecules.

References

1 J. S. Beck, J. C. Vartuli, W. J. Roth, M. E. Leonowicz, C. T. Kresge, K. D. Schmitt, C. T. W. Chu, D. H. Olson, E. W. Sheppard, S. B. McCullen, J. B. Higgins, and J. L. Schlenker, *Journal of the American Chemical Society,* A New Family of Mesoporous Molecular-Sieves Prepared with Liquid-Crystal Templates, **114** (27), 10834 (1992).

2 C. T. Kresge, M. E. Leonowicz, W. J. Roth, J. C. Vartuli, and J. S. Beck, *Nature,* Ordered Mesoporous Molecular-Sieves Synthesized by a Liquid-Crystal Template Mechanism, **359** (6397), 710 (1992).

3 J. Y. Ying, C. P. Mehnert, and M. S. Wong, *Angewandte Chemie-International Edition,* Synthesis and applications of supramolecular-templated mesoporous materials, **38** (1-2), 56 (1999).

4 N. K. Mal, M. Fujiwara, and Y. Tanaka, *Nature,* Photocontrolled reversible release of guest molecules from coumarin-modified mesoporous silica, **421** (6921), 350 (2003).

5 A. Vinu, V. Murugesan, and M. Hartmann, *Chemistry of Materials,* Pore size engineering and mechanical stability of the cubic mesoporous molecular sieve SBA-1, **15** (6), 1385 (2003).

6 B. G. Trewyn, C. M. Whitman, and V. S. Y. Lin, *Nano Letters,* Morphological control of room-temperature ionic liquid templated mesoporous silica nanoparticles for controlled release of antibacterial agents, **4** (11), 2139 (2004).

7 A. Okabe, T. Fukushima, K. Ariga, M. Niki, and T. Aida, *Journal of the American Chemical Society,* Tetrafluoroborate salts as site-selective promoters for sol-gel synthesis of mesoporous silica, **126** (29), 9013 (2004).

8 A. Vinu, T. Mori, and K. Ariga, *Science and Technology of Advanced Materials,* New families of mesoporous materials, **7** (8), 753 (2006).

9 Slowing, II, B. G. Trewyn, S. Giri, and V. S. Y. Lin, *Advanced Functional Materials,* Mesoporous silica nanoparticles for drug delivery and biosensing applications, **17** (8), 1225 (2007).

10 J. M. Kim, Y. Sakamoto, Y. K. Hwang, Y. U. Kwon, O. Terasaki, S. E. Park, and G. D. Stucky, *Journal of Physical Chemistry B,* Structural design of mesoporous silica by micelle-packing control using blends of amphiphilic block copolymers, **106** (10), 2552 (2002).

11 W. J. J. Stevens, K. Lebeau, M. Mertens, G. Van Tendeloo, P. Cool, and E. F. Vansant, *Journal of Physical Chemistry B,* Investigation of the morphology of the mesoporous SBA-16 and SBA-15 materials, **110** (18), 9183 (2006).

12 H. Zhang, J. M. Sun, D. Ma, G. Weinberg, D. S. Su, and X. H. Bao, *Journal of Physical Chemistry B,* Engineered complex emulsion system:

Toward modulating the pore length and morphological architecture of mesoporous silicas, **110** (51), 25908 (2006).

13 H. P. Lin and C. Y. Mou, *Accounts of Chemical Research,* Structural and morphological control of cationic surfactant-templated mesoporous silica, **35** (11), 927 (2002).

14 Q. S. Huo, R. Leon, P. M. Petroff, and G. D. Stucky, *Science,* Mesostructure Design with Gemini Surfactants - Supercage Formation in a 3-Dimensional Hexagonal Array, **268** (5215), 1324 (1995).

15 Q. S. Huo, D. I. Margolese, and G. D. Stucky, *Chemistry of Materials,* Surfactant control of phases in the synthesis of mesoporous silica-based materials, **8** (5), 1147 (1996).

16 A. Leonard, J. L. Blin, M. Robert, P. A. Jacobs, A. K. Cheetham, and B. L. Su, *Langmuir,* Toward a better control of internal structure and external morphology of mesoporous silicas synthesized using a nonionic surfactant, **19** (15), 5484 (2003).

17 Q. R. Chen, Y. Sakamoto, O. Terasaki, and S. A. Che, *Microporous and Mesoporous Materials,* Synthesis of silica mesoporous crystals with controlled structure and morphology using gemini surfactant, **105** (1-2), 24 (2007).

18 W. L. Huang, K. M. Liang, and S. R. Gu, *Journal of Non-Crystalline Solids,* Effect of HCl in a two-step sol-gel process using TEOS, **258** (1-3), 234 (1999).

19 M. D. Curran and A. E. Stiegman, *Journal of Non-Crystalline Solids,* Morphology and pore structure of silica xerogels made at low pH, **249** (1), 62 (1999).

20 D. G. Choi and S. M. Yang, *Journal of Colloid and Interface Science,* Effect of two-step sol-gel reaction on the mesoporous silica structure, **261** (1), 127 (2003).

21 X. G. Cui, W. C. Zin, W. J. Cho, and C. S. Ha, *Materials Letters,* Nonionic triblock copolymer synthesis of SBA-15 above the isoelectric point of silica (pH=2-5), **59** (18), 2257 (2005).

22 D. H. Chen, Z. Li, Y. Wan, X. J. Tu, Y. F. Shi, Z. X. Chen, W. Shen, C. Z. Yu, B. Tu, and D. Y. Zhao, *Journal of Materials Chemistry,* Anionic surfactant induced mesophase transformation to synthesize highly ordered large-pore mesoporous silica structures, **16** (16), 1511 (2006).

23 P. Yuan, S. Yang, H. N. Wang, M. H. Yu, X. F. Zhou, G. Q. Lu, J. Zou, and C. Z. Yu, *Langmuir,* Structure transition from hexagonal mesostructured rodlike silica to multilamellar vesicles, **24** (9), 5038 (2008).

24 M. Singh, C. Ford, V. Agarwal, G. Fritz, A. Bose, V. T. John, and G. L. McPherson, *Langmuir,* Structural evolution in cationic micelles upon incorporation of a polar organic dopant, **20** (23), 9931 (2004).

25 J. M. Sun, D. Ma, H. Zhang, C. L. Wang, X. H. Bao, D. S. Su, A. Klein-Hoffmann, G. Weinberg, and S. Mann, *Journal of Materials*

Chemistry, Phase evolution in the alkane-P123-water-TEOS quadru-component system: a feasible route to different complex mesostructured materials, **16** (16), 1507 (2006).

26 K. Cui, Q. Cai, X. H. Chen, Q. L. Feng, and H. D. Li, *Microporous and Mesoporous Materials,* Mophologies of vesicular silica templated by cationic surfactant with the auxiliary of diethyl ether, **68** (1-3), 61 (2004).

27 H. Q. Yin, S. Lei, S. B. Zhu, J. B. Huang, and J. P. Ye, *Chemistry-a European Journal,* Micelle-to-vesicle transition induced by organic additives in catanionic surfactant systems, **12** (10), 2825 (2006).

28 P. Schmidt-Winkel, W. W. Lukens, D. Y. Zhao, P. D. Yang, B. F. Chmelka, and G. D. Stucky, *Journal of the American Chemical Society,* Mesocellular siliceous foams with uniformly sized cells and windows, **121** (1), 254 (1999).

29 P. Schmidt-Winkel, W. W. Lukens, P. D. Yang, D. I. Margolese, J. S. Lettow, J. Y. Ying, and G. D. Stucky, *Chemistry of Materials,* Microemulsion templating of siliceous mesostructured cellular foams with well-defined ultralarge mesopores, **12** (3), 686 (2000).

30 P. Schmidt-Winkel, C. J. Glinka, and G. D. Stucky, *Langmuir,* Microemulsion templates for mesoporous silica, **16** (2), 356 (2000).

31 J. Fan, C. Z. Yu, L. M. Wang, B. Tu, D. Y. Zhao, Y. Sakamoto, and O. Terasaki, *Journal of the American Chemical Society,* Mesotunnels on the silica wall of ordered SBA-15 to generate three-dimensional large-pore mesoporous networks, **123** (48), 12113 (2001).

32 D. H. W. Hubert, M. Jung, P. M. Frederik, P. H. H. Bomans, J. Meuldijk, and A. L. German, *Advanced Materials,* Vesicle-directed growth of silica, **12** (17), 1286 (2000).

33 G. S. Attard, J. C. Glyde, and C. G. Goltner, *Nature,* Liquid-Crystalline Phases as Templates for the Synthesis of Mesoporous Silica, **378** (6555), 366 (1995).

34 M. Templin, A. Franck, A. DuChesne, H. Leist, Y. M. Zhang, R. Ulrich, V. Schadler, and U. Wiesner, *Science,* Organically modified aluminosilicate mesostructures from block copolymer phases, **278** (5344), 1795 (1997).

35 A. Monnier, F. Schuth, Q. Huo, D. Kumar, D. Margolese, R. S. Maxwell, G. D. Stucky, M. Krishnamurty, P. Petroff, A. Firouzi, M. Janicke, and B. F. Chmelka, *Science,* Cooperative Formation of Inorganic-Organic Interfaces in the Synthesis of Silicate Mesostructures, **261** (5126), 1299 (1993).

36 Q. S. Huo, D. I. Margolese, U. Ciesla, D. G. Demuth, P. Y. Feng, T. E. Gier, P. Sieger, A. Firouzi, B. F. Chmelka, F. Schuth, and G. D. Stucky, *Chemistry of Materials,* Organization of Organic-Molecules with Inorganic Molecular-Species into Nanocomposite Biphase Arrays, **6** (8), 1176 (1994).

37 D. Y. Zhao, J. L. Feng, Q. S. Huo, N. Melosh, G. H. Fredrickson, B. F. Chmelka, and G. D. Stucky, *Science,* Triblock copolymer syntheses of mesoporous silica with periodic 50 to 300 angstrom pores, **279** (5350), 548 (1998).

38 H. Djojoputro, X. F. Zhou, S. Z. Qiao, L. Z. Wang, C. Z. Yu, and G. Q. Lu, *Journal of the American Chemical Society,* Periodic mesoporous organosilica hollow spheres with tunable wall thickness, **128** (19), 6320 (2006).

39 E. P. Barrett, L. G. Joyner, and P. P. Halenda, *Journal of the American Chemical Society,* The Determination of Pore Volume and Area Distributions in Porous Substances .1. Computations from Nitrogen Isotherms, **73** (1), 373 (1951).

40 H. P. Lin, S. T. Wong, C. Y. Mou, and C. Y. Tang, *Journal of Physical Chemistry B,* Extensive void defects in mesoporous aluminosilicate MCM-41, **104** (38), 8967 (2000).

41 E. Prouzet, F. Cot, C. Boissiere, P. J. Kooyman, and A. Larbot, *Journal of Materials Chemistry,* Nanometric hollow spheres made of MSU-X-type mesoporous silica, **12** (5), 1553 (2002).

42 P. T. Tanev and T. J. Pinnavaia, *Science,* Biomimetic templating of porous lamellar silicas by vesicular surfactant assemblies, **271** (5253), 1267 (1996).

43 M. U. Martines, E. Yeong, M. Persin, A. Larbot, W. F. Voorhout, C. K. U. Kubel, P. Kooyman, and E. Prouzet, *Comptes Rendus Chimie,* Hexagonal mesoporous silica nanoparticles with large pores and a hierarchical porosity tested for HPLC, **8** (3-4), 627 (2005).

44 H. N. Wang, Y. H. Wang, X. F. Zhou, L. Zhou, J. W. Tang, J. Lei, and C. Z. Yu, *Advanced Functional Materials,* Siliceous Unilamellar Vesicles and Foams by Using Block-Copolymer Cooperative Vesicle Templating, **17**, 613 (2007).

45 S. Ruthstein, V. Frydman, S. Kababya, M. Landau, and D. Goldfarb, *Journal of Physical Chemistry B,* Study of the formation of the mesoporous material SBA-15 by EPR spectroscopy, **107** (8), 1739 (2003).

46 S. Ruthstein, V. Frydman, and D. Goldfarb, *Journal of Physical Chemistry B,* Study of the initial formation stages of the mesoporous material SBA-15 using spin-labeled block co-polymer templates, **108** (26), 9016 (2004).

47 K. Flodstrom, H. Wennerstrom, C. V. Teixeira, H. Amenitsch, M. Linden, and V. Alfredsson, *Langmuir,* Time-resolved in situ studies of the formation of cubic mesoporous silica formed with triblock copolymers, **20** (23), 10311 (2004).

48 M. Antonietti and S. Forster, *Advanced Materials,* Vesicles and liposomes: A self-assembly principle beyond lipids, **15** (16), 1323 (2003).

Chapter 5 Synthesis of nitrogen doped porous carbon materials

5.1. Introduction

Porous carbon materials are important in many areas of modern science and technology, including water and air purification, gas separation, catalysis, and energy storage. (1,2) Recently, they are regarded as attractive candidates for hydrogen storage because of a combination of adsorption ability, high specific surface area, pore microstructure, good mechanical stability, and low mass density. The hydrogen storage behaviour of carbonaceous materials with high specific surface area, such as activated carbons, activated carbon fibre, carbon nanotubes, and mesoporous carbons have been investigated and reported.

Most porous carbon materials are primarily microporous (< 2 nm), which makes them well suited for many applications. However, there are numerous potential applications in which materials with carbonaceous surfaces would be attractive but require the presence of larger pores, preferably in the mesopore (2~50 nm) and macropore (> 50 nm) range. These include for instance adsorption of large molecules, catalyst support, chromatographic separations, electrochemical double layer capacitors, and fuel cells. Therefore, there has been a considerable interest in the synthesis of ordered mesoporous and macroporous carbon materials.

Porous carbon materials have been synthesized using various methods. The following represents traditional methods, as following:

1) Chemical activation, physical activation, and a combination of the physical and chemical activation processes. (3-7)
2) Catalytic activation of carbon precursors in the presence of certain metal salts or organometallic compounds. (8-10)
3) Carbonization of polymer blends with one thermally unstable component such as a carbonizable polymer and a pyrolyzable polymer. (11-14)
4) Carbonization of a polymer aerogel or cryogel synthesized under supercritical drying conditions. (15-17)

Although many porous carbon materials have been developed using the above-mentioned methods, the synthesis of porous carbon materials with a very narrow pore size distribution has been very challenging. Over the last two decades, the technique of template carbonization has been developed, and many kinds of rigid and designed inorganic templates have been employed in an attempt to synthesize carbons with uniform pore sizes.

In 1986, Knox and his co-workers(18) reported that silica gel can be impregnated with polymer precursors that can be polymerized to form a continuous network surrounding the silica particles. The carbonization of the polymer coating and the subsequent dissolution of the silica gel template rendered a mesoporous carbon with

a rigid structure featuring also some micropores. Since then, many porous carbon materials with uniform pore sizes having micropores, mesopores, or macropores have been synthesized using various inorganic templates.

Mallouk's group (1997) (19) synthesized phenol formaldehyde polymers by making use of the acidity of the zeolite framework inside various zeolite, and then carbonized the polymer/zeolite composites to obtain porous carbons. Phenol was infiltrated into the narrow pores of the zeolite by the vapor-phase infiltration method. These carbons consisted of both micropores and a considerable amount of mesopores. Later, Kyotani's group (20) reported successful synthesis of uniformly sized and ordered microporous carbon materials using zeolite Y as a template through a two step carbonization method.

Ryoo and his coworkers (21) successfully synthesized an ordered mesoporous carbon designated as CMK-3 using hexagonally ordered mesoporous silica SBA-15 as a template. The ordered structure of the CMK-3 carbon was the exact inverse replica of the SBA-15 silica without the structural transformation during the removal of the silica template. CMK-3 type ordered mesoporous carbon was also synthesized by the infiltration of the carbon precursor via adsorption in the vapor phase and using p-toluene sulfonic acid impregnated SBA-15 as a template. (22)

For the synthesis of macroporous carbon materials with core-shell structures, spherical submicrometer sized silica particles have been used as templates. The pore size of the resulting macroporous carbon materials could be easily controlled by varying the particle size of the silica spheres. Zakhidov et al.(23) synthesized various structured macroporous carbon materials using synthetic silica opals, which were made by the self-assembly of uniform sized silica spheres as templates and by the infiltration of a phenolic resin as carbon precursor.

Liu and coworkers (24) presented the preparation of monodisperse silica poly divinylbenzene (SiO_2/PDVB) and silica poly(ethyleneglycol dimethacrylate) (SiO_2/PEGDMA) core shell hybrid microspheres by encapsulation of the 3-methacryloxy-propyltrimethoxysilane (MPS) modified silica cores during the distillation precipitation polymerization of divinylbenzene (DVB) or ethyleneglycol dimethacrylate (EGDMA) in neat acetonitrile in the absence of any stabilizer or surfactant. This is a two stage reaction, in which the silica core with diameter of 238 nm was prepared according to the Stober method in the first stage. Silica particles were used as seeds in the second stage of reaction for the growth of core shell hybrid microspheres. Further, the corresponding polyDVB and polyEGDMA hollow microspheres having a well defined size and controlled shell thickness (9-33 nm) were developed after selective removal of the silica core in hydrofluoric acid. From their results, the shell thickness of the resultant polyEGDMA hollow microspheres

could be controlled by the amount of EGDMA monomer during the encapsulation of polyEGDMA over MPS modified silica core.

Recently, carbon cryogels have attracted much more attention as an activated carbon. Carbon cryogels can be synthesized through the sol-gel polycondensation of resorcinol with formaldehyde in a slightly basic aqueous solution followed by freeze drying and pyrolysis in an inert atmosphere. Carbon cryogels possess high surface areas and large mesopore volumes and their mesoporosity can be controlled by varying the amounts of the reactants, catalyst and water used in the sol-gel polycondensation. Feaver and co-workers reported the successful synthesis of carbon crygels. (25) In their work, carbon crygels have pores ranging from 2 to 20 nm in diameter and with a pore volume of 0.70 cm^3/g, and a surface area of 300 m^2/g.

While there is no doubt that silica templates play a vital role in the formation of replicated porous carbon materials, carbon precursors can greatly influence the final contents and surface properties. Generally, porous carbon materials were produced using sucrose ($C_{12}H_{22}O_{11}$), furfuryl alcohol ($C_5H_6O_2$), glucose ($C_6H_{12}O_6$), phenol (C_6H_6O), and resorcinol ($C_6H_6O_2$) as carbon precursor. As reported in literature, the synthesis of mesoporous carbon CMK-3 was performed using sucrose as the carbon source. (21) However, the presence of other elements in carbon precursors has been considered to produce novel porous carbon materials with designable and functional structure and surface properties.

There is considerable interest in research on the synthesis and characterization of nitrogen doped carbon nanostructures because of their new application as electrode materials for double layer capacitors and catalytic materials for proton exchange membrane fuel cells. (26) However, there are some challenges in its commercialization. One of the main problems is the production cost of component materials, for instance membranes, bipolar plates and carbon supported platinum and its alloys.

Carbon is an ideal support for electrocatalysts for fuel cell due to its high electronic conductivity, corrosion resistance, surface properties, easy reclaim of precious catalytic metals and the low cost. Moreover, it is generally believed that metal catalysts should be deposited on porous nanostructure materials in order to increase the specific surface area, which is the prerequisite to obtain an acceptable catalytic performance. (27,28) The combined physical and electrochemical properties of, porous carbon materials make them the stand out candidate among other materials.

Graphite nanofibers, (29) carbon nanotubes, (30) carbon nanohorns (31) and carbon nanocoils (32,33) have shown promising results towards fuel cell electrode reactions. But in terms of activity, cost and durability, current catalysts still need great improvement to meet the target requirements. It is found that the surface chemistry and the structure of the support materials can greatly influence the activity of the resultant catalysts. (34,35) This is because the interaction between the support and

metal catalyst can modify the electric structure of catalytic metals which in turn changes the catalytic activity, and the durability of the resultant catalysts depends on the metal-support interaction and the durability of the support materials. Moderate nitrogen content in the carbon matrix apparently produced a beneficial effect on capacitance behavior of the porous electrodes in acidic medium based on its faradaic reaction. (36-38)

There are two methods often used in producing nitrogen doped porous carbon materials. (35) One is doping directly during the synthesis procedure, and the other is post treatment of pre-synthesized carbon materials with nitrogen containing precursor. In recent years, many efforts are devoted on the template growth of nitrogen doped carbon materials. Xia and Mokaya (39) reported well ordered porous nitrogen doped carbon materials that possess graphitic pore walls prepared via chemical vapor deposition and pyrolysis with the pure silica SBA-15 or other mesoporous silica as solid templates. Hou et al (40) reported a nitrogen containing microporous carbon with a highly ordered structure synthesized by using zeolite Y as a template.

In this chapter, spherical silica particles were chosen as templates to synthesize macroporous carbon materials which have large pore space for impregnating guest materials. Particularly, porous carbon materials presented in this chapter have been produced using melamine formaldehyde resin as nitrogen containing carbon

precursor and silicate colloidal spheres as hard templates prepared via a sol-gel polymerization method. The carbon precursor used in this process is commercially available and very cheap, which will be favorable in the preparation of porous carbon materials on a large scale. The resultant porous carbon materials show high specific surface areas and high pore volume, large pore size, and moderate content of nitrogen. It is anticipated that these prominent features can provide a new nanoscaffold for loading AB and influence the hydrogen release performance of AB confined in nanostructured scaffolds.

5.2. Experimental

Chemicals:

Chemicals including tetraethyl orthosilicate (TEOS, Reagent Plus 99%), ethanol (absolute AR.), aqueous ammonia (25wt% NH_3 in water), formaldehyde (36 wt% HCHO solution in water), melamine ($C_3H_6N_6$, purum, >99%), hydrochloric acid (2.0mol/L HCl solution in water), hydrofluoric acid (35wt% HF solution in water) were purchased from SIGMA-ALDRICH and were used as received without further purification. Aerosil 200 and Aerosil 300 were purchased from EVONIK DEGUSSA. Deionized water was used in all experiments.

Characterization:

The morphology and microstructure of the synthesized samples were characterized by N_2 absorption-desorption isotherms and scanning electron microscopy (SEM).

The BET surface areas and textural structure were measured using an automated adsorption analyzer Micromeritics Tristar ASAP 3000 system. The samples were degassed at 196 °C overnight on a vacuum line prior to analysis. The SEM photomicrograph of the samples was taken in a JEOL 6400 microscope with Pt coating.

The surface chemistry of samples was determined using a Kratos Axis ULTRA X-ray Photoelectron Spectrometer (XPS) incorporating a 165mm hemispherical electron energy analyser. The incident radiation was Monochromatic Al Kα X-rays (1486.6eV) at 150W (15kV, 10ma) and at 45 degrees to the sample surface. Photoelectron data was collected at a take-off angle of theta = 90^{o}. Survey (wide) scans were taken at an analyser pass energy of 160eV and multiplex (narrow) high resolution scans at 20eV. Survey scans were carried out over 1200-0eV binding energy range with 1.0eV steps and a dwell time of 100ms. Narrow high-resolution scans were run with 0.05ev steps and 250ms dwell time. Base pressure in the analysis chamber was $1.0x10^{-9}$ torr and during sample analysis $1.0x10^{-8}$ torr. Atomic concentrations were calculated using the CasaXPS version 2.3.14 software and a linear baseline with Kratos library Relative Sensitivity Factors (RSFs).

5.2.1 Synthesis of spherical silica particles

Silica spheres were prepared according to the Stöber method,(41) a system of chemical reactions based on the fact that silica particles can be produced by chemical

reaction of tetraesters of silicie acid (tetraalkyl silicates) with certain solutions. The procedure involves ammonic catalyzed hydrolysis of TEOS in ethanol at room temperature, which leads to the precipitation of monodisperse spherical silica particles. The desired diameter of the silica particles from 150-450 nm can be controlled by careful variation of reagent conditions, such as the concentrations of water, ammonia and TEOS.

At the beginning of each preparation, ethanol, aqueous ammonia solution and water were mixed in sealed bottles in the desired concentrations of ammonia and water. Subsequently the siliceous solution was added and the bottles were put on a magnetic stirrer. The total amount of solution in each test varied between 50 mL and 100 mL. The condensation reaction generally started within 15 min and the total reaction time was varied between 12 hours and 24 hours.

In a typical synthesis, 6.24 g TEOS was first dissolved in 50 mL ethanol. 5.4 g ammonia, 4.0 g water with 50 mL ethanol were added to the mixture and stirred for 24 hours at room temperature. The siliceous products can be collected by centrifugation and washed with deionized water. The obtained silica precipitate was dried at room temperature in air and then was dispersed in deionized water with concentration of 5.0 g/100mL for further use.

5.2.2 Synthesis of nitrogen doped porous carbon materials

In our study, porous carbon materials were derived using melamine formaldehyde resin (MF) as nitrogen-containing carbon precursor and silicate colloid as a silica source via the sol-gel polymerization induced colloid aggregation method.

Monodisperse functional silica/polymer core-shell composite materials with silica as core and polymer as shell can be prepared by a two stage reaction. The silica core with different diameter was synthesized in the first stage. The polymer shell was then coated onto the silica core particles by sol gel polymerization. Carbonization by pyrolysis under an inert atmosphere resulted in the formation of carbon silica composite. After being dissolved in an HF solution, the silica template was removed and a porous carbon material was produced.

The silica samples with particle sizes of about 450 nm, 320 nm, 230 nm, and 150 nm were obtained in the above synthesis. Spherical silica materials with the particle size of 12 nm and 7 nm are commercial fumed silica Aerosil 200 and Aerosil 300 which have been used in our work as small size silica template.

In a typical synthesis, 3.15 g (25 mmol) melamine and 5.0 ml (66 mmol) formaldehyde solution (36 wt%) were firstly added into 12.5 ml deionized water and stirred at 85 °C to obtain a clear solution. After 20 minutes under stirring, the resulting precursor solution was cooled down to 40 °C and poured into 30 ml silica

colloid solution at 40 °C under magnetic stirring. After that, pH value of the mixtures was adjusted to 4.5 by addition of hydrochloric acid solution (2.0mol/L) and the mixtures were kept at a static condition for 20 hours to obtain the MF/silica composites. These composites were collected by filtration, washed with deionized water and ethanol, and dried in air at room temperature. In order to prepare the porous carbon materials, the MF/silica composites were firstly cured at 180 °C for 24 hours in air, then carbonized at up to 900 °C for 5 hours under a nitrogen flow in tube furnace to obtain the carbon/silica composites. The heating rate was 3°C/min. Finally, 20 wt% HF solution was used to etch the silica template at room temperature. The final porous carbon materials dispersed in a liquid was collected by filtration and washed with deionized water and dried at room temperature in air.

5.3 Results and discussion

5.3.1 Silica particles

In this procedure, ammonia is used as a morphological catalyst to induce the formation of spherical particles. The concentration of ammonia in the solution also influences the size of the particle formed. Our results are consistent with those from literature. SEM images of spherical silica particles with uniform size are shown in Figure 5.1, representing four silica samples obtained under comparable conditions. When the ammonia concentration is 1.8 mol/L, 1.3 mol/L, 0.8 mol/L, and 0.3 mol/L, the mean diameters of silica spheres are 450, 320, 230 and 150 nm, respectively. It is found that, as ammonia concentration increases, larger particle size obtained. When

the ammonia concentration decreases to a certain level, such as 0.1 mol/L in our experiments, almost no spherical particles can be obtained except few irregular small particles are observed under the electron microscopy.

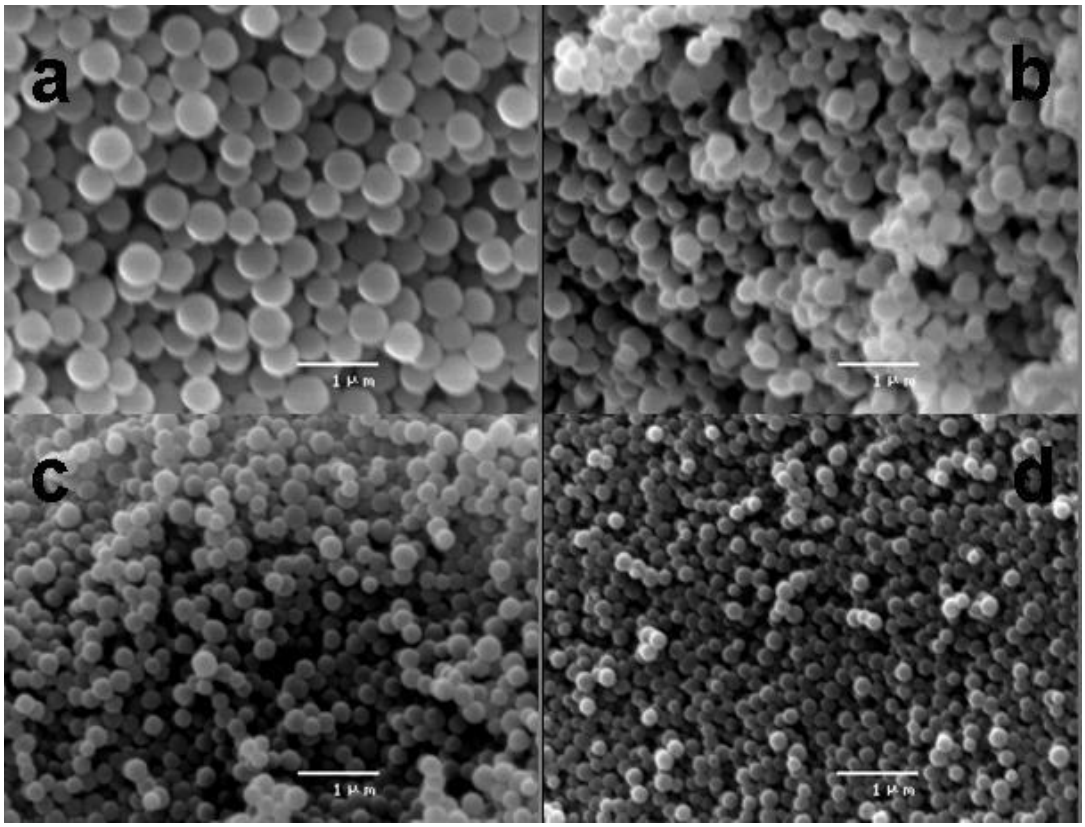

Figure 5.1 SEM images of four spherical silica samples obtained in our experimental systems, with ammonia concentration a: 1.8 mol/L, b: 1.3 mol/L, c: 0.8 mol/L, and d: 0.3 mol/L.

During the reaction process after mixing TEOS with the other reactants, an increasing opalescence in the mixture solution can be observed as a function of reaction time, suggestive of the hydrolysis of TEOS to form silicic acid and the condensation of silicic acid to form condensed silica species. In order to avoid the

kinetic influence of reaction time on the particle size of silica spheres, the precipitates after 12 and 24 hours were collected by centrifugation and observed under SEM, showing inconspicuous differences in particle size for the four ammonia concentrations under investigation. Therefore, a reaction time of 24 hour was chosen in our experiments.

5.3.2 Porous carbon

A series of porous carbon materials have been synthesized under different experimental conditions and using various silica template of different particle size. SEM images displaying typical morphologies of porous carbon samples are shown in Figure 5.2. It can be seen that all presented porous carbon samples contain plenty of voids as well as open micropores. A loosely packed nanoframe constructs the whole material.

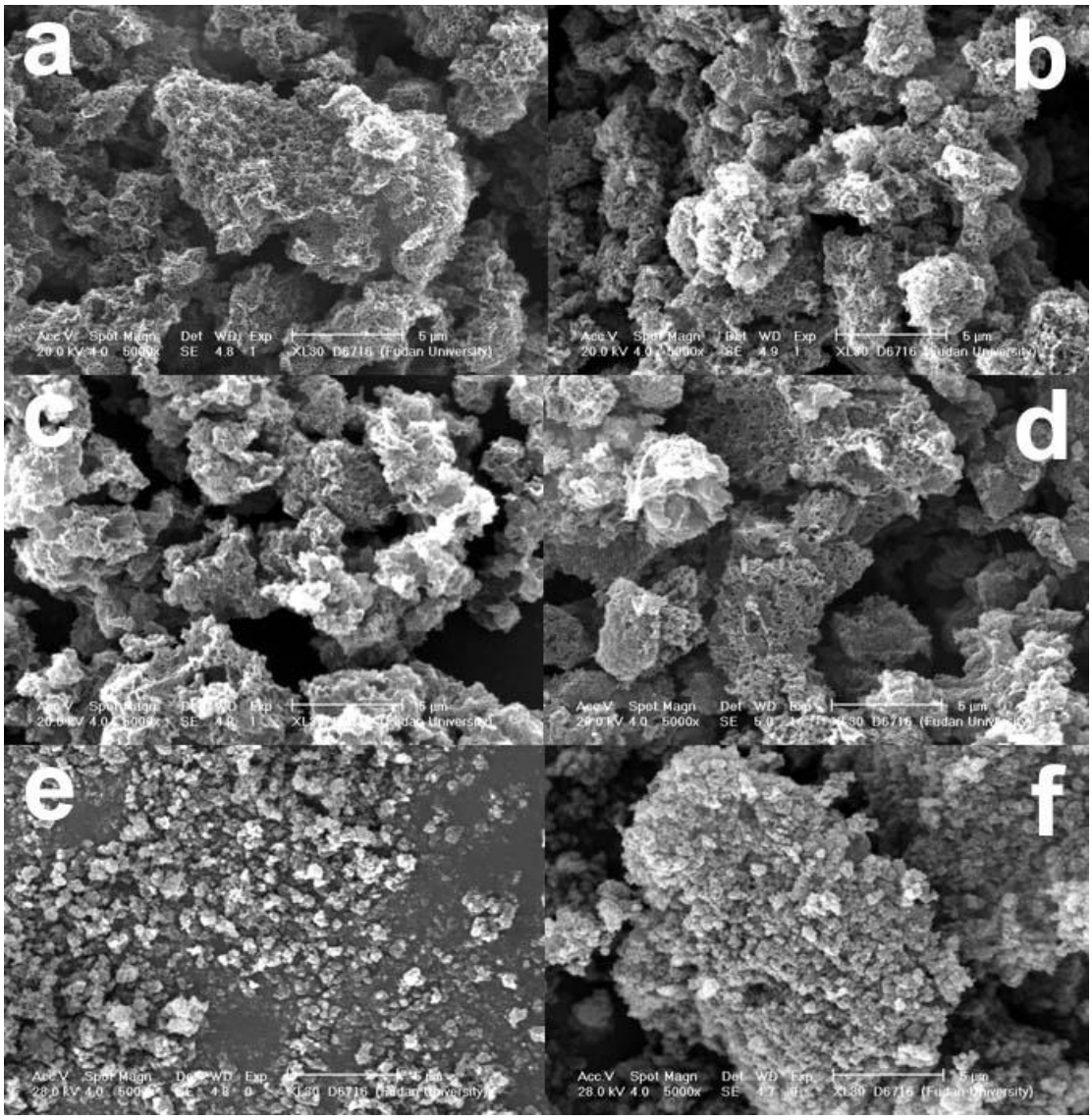

Figure 5.2 SEM microphotographs of porous carbon samples synthesized with different silica templates (images a-f corresponding to Samples S1-S6 in Table 5.1)

Nitrogen sorption isotherm analyses can provide detailed information about the surface area and pore volume of the porous carbon materials. The values of surface area and pore volume of these samples were shown in Table 5.1.

Table 5.1: Structural characteristics of porous carbon synthesized at different conditions

Sample ID	Silica particle size (nm)	Carbon surface area (m^2/g)	Carbon pore volume (cm^3/g)
S1	450	737	1.43
S2	320	355	0.92
S3	230	453	1.03
S4	150	652	1.52
S5	12	505	1.30
S6	7	642	1.55

Nitrogen adsorption/desorption data of porous carbon materials shown in Figure 5.3 exhibit Type II isotherms and the capillary condensation steps occur at a relative pressure about $P/P_0 > 0.45$, indicative of porous materials consisting large voids or hollow particles with porous walls.

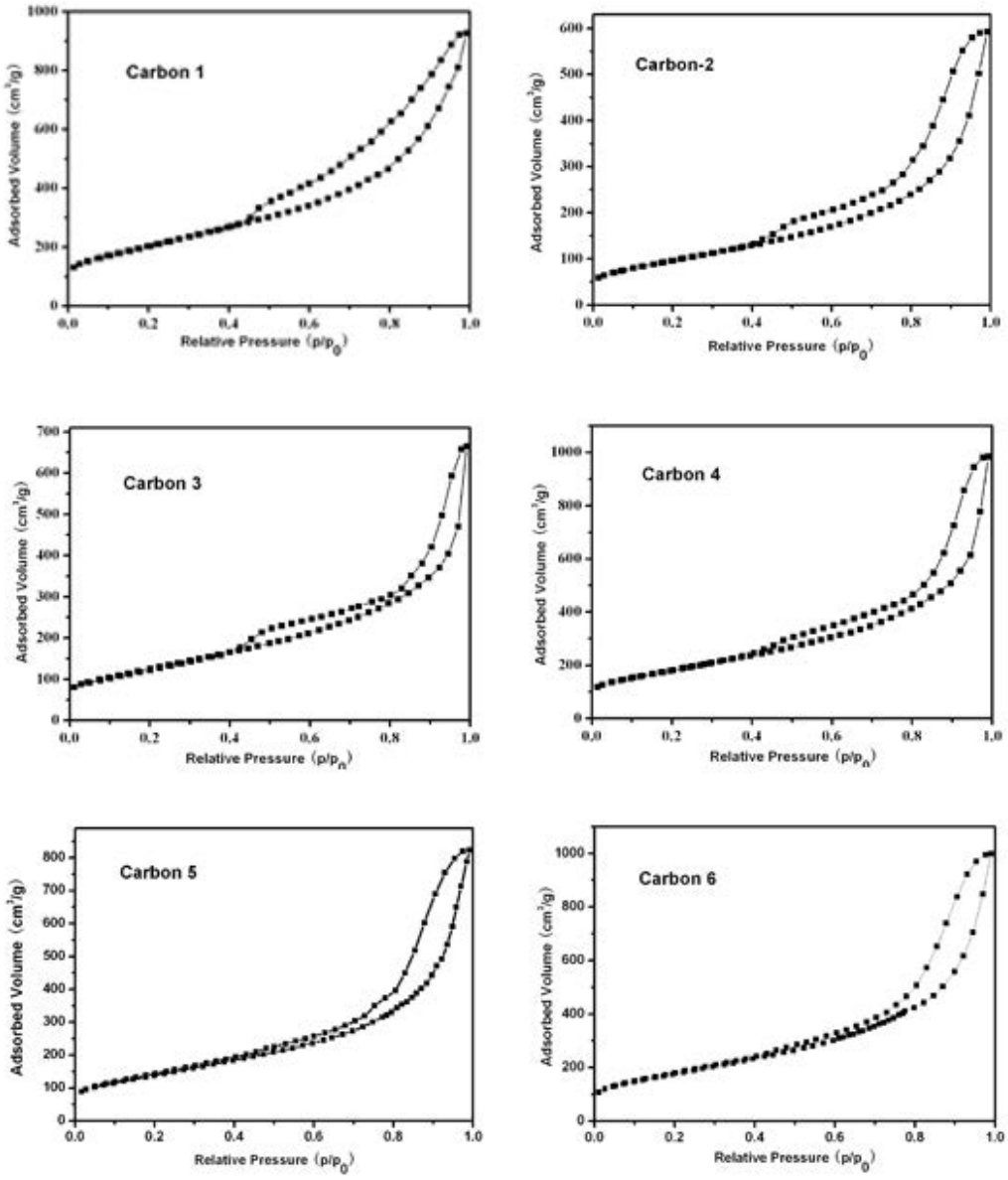

Figure 5.3 Nitrogen sorption isotherms of porous carbon samples S1-S6

The XPS result of one selected porous carbon sample (Sample 4) is shown in Figure 5.4. It shows that the nitrogen contents of Sample is 5.09 wt%. As reported previously, the performances of porous carbon materials are greatly influenced by the surface functional groups. The porous carbon materials obtained in our approach have moderate content of nitrogen, which can be used to entrap AB for hydrogen

storage. The performance of the nitrogen-doped porous carbons in the storage of hydrogen will be discussed in detail in the next chapter.

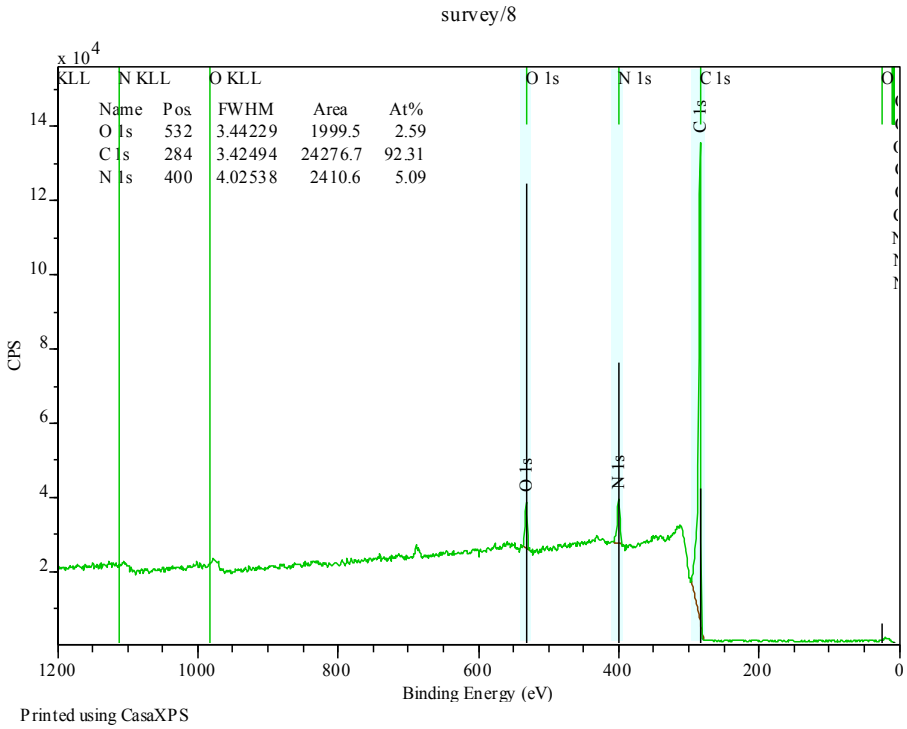

Figure 5.4 The XPS results of porous carbon S4

5.4 Conclusions

In this chapter, silica spheres with controlled diameters have been successfully synthesized. By using a series of silica particles as hard templates, N-doped porous carbon materials were prepared. These porous carbon materials have high pore volumes, adjustable pore sizes, and moderate content of nitrogen in the pore walls. It is anticipated that these porous carbon materials may be used as nano-scaffolds for loading AB and possess improved hydrogen release performance.

References

1 S. Subramoney, *Advanced Materials,* Novel nanocarbons - Structure, properties, and potential applications, **10** (15), 1157 (1998).

2 T. Kyotani, *Carbon,* Control of pore structure in carbon, **38** (2), 269 (2000).

3 Z. H. Hu, M. P. Srinivasan, and Y. M. Ni, *Advanced Materials,* Preparation of mesoporous high-surface-area activated carbon, **12** (1), 62 (2000).

4 Y. Zou and B. X. Han, *Energy & Fuels,* High-surface-area activated carbon from Chinese coal, **15** (6), 1383 (2001).

5 A. Ahmadpour and D. D. Do, *Carbon,* The preparation of active carbons from coal by chemical and physical activation, **34** (4), 471 (1996).

6 T. Y. Zhang, W. P. Walawender, L. T. Fan, M. Fan, D. Daugaard, and R. C. Brown, *Chemical Engineering Journal,* Preparation of activated carbon from forest and agricultural residues through CO2 activation, **105** (1-2), 53 (2004).

7 T. Yang and A. C. Lua, *Journal of Colloid and Interface Science,* Characteristics of activated carbons prepared from pistachio-nut shells by physical activation, **267** (2), 408 (2003).

8 H. Marsh and B. Rand, *Carbon,* Process of Activation of Carbons by Gasification with Co2 .2. Role of Catalytic Impurities, **9** (1), 63 (1971).

9 H. Tamai, T. Kakii, Y. Hirota, T. Kumamoto, and H. Yasuda, *Chemistry Of Materials,* Synthesis of extremely large mesoporous activated carbon and its unique adsorption for giant molecules, **8** (2), 454 (1996).

10 A. Oya, S. Yoshida, J. Alcanizmonge, and A. Linaressolano, *Carbon,* Formation of Mesopores in Phenolic Resin-Derived Carbon-Fiber by Catalytic Activation Using Cobalt, **33** (8), 1085 (1995).

11 N. Patel, K. Okabe, and A. Oya, *Carbon,* Designing carbon materials with unique shapes using polymer blending and coating techniques, **40** (3), 315 (2002).

12 J. Ozaki, N. Endo, W. Ohizumi, K. Igarashi, M. Nakahara, A. Oya, S. Yoshida, and T. Iizuka, *Carbon,* Novel preparation method for the production of mesoporous carbon fiber from a polymer blend, **35** (7), 1031 (1997).

13 A. Oya and N. Kasahara, *Carbon,* Preparation of thin carbon fibers from phenol-formaldehyde polymer micro-beads dispersed in polyethylene matrix, **38** (8), 1141 (2000).

14 J. AlcanizMonge, D. CazorlaAmoros, A. LinaresSolano, A. Oya, A. Sakamoto, and K. Hoshi, *Carbon,* Preparation of general purpose carbon fibers from coal tar pitches with low softening point, **35** (8), 1079 (1997).

15 R. W. Pekala, *Journal Of Materials Science,* Organic Aerogels from the Polycondensation of Resorcinol with Formaldehyde, **24** (9), 3221 (1989).

16 R. W. Pekala and D. W. Schaefer, *Macromolecules,* Structure of Organic Aerogels .1. Morphology and Scaling, **26** (20), 5487 (1993).

17 R. W. Pekala, C. T. Alviso, F. M. Kong, and S. S. Hulsey, *Journal of Non-Crystalline Solids,* Aerogels Derived from Multifunctional Organic Monomers, **145** (1-3), 90 (1992).

18 J. H. Knox, B. Kaur, and G. R. Millward, *Journal of Chromatography,* Structure and Performance of Porous Graphitic Carbon in Liquid-Chromatography, **352**, 3 (1986).

19 S. A. Johnson, E. S. Brigham, P. J. Ollivier, and T. E. Mallouk, *Chemistry Of Materials,* Effect of micropore topology on the structure and properties of zeolite polymer replicas, **9** (11), 2448 (1997).

20 Z. X. Ma, T. Kyotani, and A. Tomita, *Chemical Communications,* Preparation of a high surface area microporous carbon having the structural regularity of Y zeolite, (23), 2365 (2000).

21 S. Jun, S. H. Joo, R. Ryoo, M. Kruk, M. Jaroniec, Z. Liu, T. Ohsuna, and O. Terasaki, *Journal Of The American Chemical Society,* Synthesis of new, nanoporous carbon with hexagonally ordered mesostructure, **122** (43), 10712 (2000).

22 A. B. Fuertes and D. M. Nevskaia, *Journal Of Materials Chemistry,* Template synthesis of mesoporous carbons from mesostructured silica by vapor deposition polymerisation, **13** (7), 1843 (2003).

23 A. A. Zakhidov, R. H. Baughman, Z. Iqbal, C. X. Cui, I. Khayrullin, S. O. Dantas, I. Marti, and V. G. Ralchenko, *Science,* Carbon structures with three-dimensional periodicity at optical wavelengths, **282** (5390), 897 (1998).

24 G. Y. Liu, H. Zhang, X. L. Yang, and Y. M. Wang, *Polymer,* Facile synthesis of silica/polymer hybrid microspheres and hollow polymer microspheres, **48** (20), 5896 (2007).

25 A. Feaver, S. Sepehri, P. Shamberger, A. Stowe, T. Autrey, and G. Z. Cao, *Journal Of Physical Chemistry B,* Coherent carbon cryogel-ammonia borane nanocomposites for H-2 storage, **111** (26), 7469 (2007).

26 T. Maiyalagan, B. Viswanathan, and U. Varadaraju, *Electrochemistry Communications,* Nitrogen containing carbon nanotubes as supports for Pt - Alternate anodes for fuel cell applications, **7** (9), 905 (2005).

27 F. Rodriguez-Reinoso, *Carbon,* The role of carbon materials in heterogeneous catalysis, **36** (3), 159 (1998).

28 A. T. Bell, *Science,* The impact of nanoscience on heterogeneous catalysis, **299** (5613), 1688 (2003).

29 E. S. Steigerwalt, G. A. Deluga, D. E. Cliffel, and C. M. Lukehart, *Journal Of Physical Chemistry B,* A Pt-Ru/graphitic carbon nanofiber nanocomposite exhibiting high relative performance as a direct-methanol fuel cell anode catalyst, **105** (34), 8097 (2001).

30 Y. Y. Shao, G. P. Yin, H. H. Wang, Y. Z. Gao, and P. F. Shi, *Journal Of Power Sources,* Multi-walled carbon nanotubes based Pt electrodes prepared with in situ ion exchange method for oxygen reduction, **161** (1), 47 (2006).

31 T. Yoshitake, Y. Shimakawa, S. Kuroshima, H. Kimura, T. Ichihashi, Y. Kubo, D. Kasuya, K. Takahashi, F. Kokai, M. Yudasaka, and S. Iijima, *Physica B-Condensed Matter,* Preparation of fine platinum catalyst supported on single-wall carbon nanohorns for fuel cell application, **323** (1-4), 124 (2002).

32 S. H. Joo, S. J. Choi, I. Oh, J. Kwak, Z. Liu, O. Terasaki, and R. Ryoo, *Nature,* Ordered nanoporous arrays of carbon supporting high dispersions of platinum nanoparticles, **412** (6843), 169 (2001).

33 T. Hyeon, S. Han, Y. E. Sung, K. W. Park, and Y. W. Kim, *Angewandte Chemie-International Edition,* High-performance direct methanol fuel cell electrodes using solid-phase-synthesized carbon nanocoils, **42** (36), 4352 (2003).

34 P. H. Matter, E. Wang, and U. S. Ozkan, *Journal of Catalysis,* Preparation of nanostructured nitrogen-containing carbon catalysts for the oxygen reduction reaction from SiO2- and MgO-supported metal particles, **243** (2), 395 (2006).

35 C. P. Ewels and M. Glerup, *Journal Of Nanoscience And Nanotechnology,* Nitrogen doping in carbon nanotubes, **5** (9), 1345 (2005).

36 V. V. Strelko, V. S. Kuts, and P. A. Thrower, *Carbon,* On the mechanism of possible influence of heteroatoms of nitrogen, boron and phosphorus in a carbon matrix on the catalytic activity of carbons in electron transfer reactions, **38** (10), 1499 (2000).

37 H. J. Burch, J. A. Davies, E. Brown, L. Hao, S. A. Contera, N. Grobert, and J. F. Ryan, *Applied Physics Letters,* Electrical conductance and breakdown in individual CNx multiwalled nanotubes, **89** (14), 3 (2006).

38 M. Terrones, *Annual Review Of Materials Research,* Science and technology of the twenty-first century: Synthesis, properties and applications of carbon nanotubes, **33**, 419 (2003).

39 Y. D. Xia and R. Mokaya, *Advanced Materials,* Synthesis of ordered mesoporous carbon and nitrogen-doped carbon materials with graphitic pore walls via a simple chemical vapor deposition method, **16** (17), 1553 (2004).

40 P. X. Hou, H. Orikasa, T. Yamazaki, K. Matsuoka, A. Tomita, N. Setoyama, Y. Fukushima, and T. Kyotani, *Chemistry Of Materials,* Synthesis of nitrogen-containing microporous carbon with a highly ordered structure and effect of nitrogen doping on H2O adsorption, **17** (20), 5187 (2005).

41 W. Stober, A. Fink, and E. Bohn, *Journal of Colloid and Interface Science,* Controlled Growth Of Monodisperse Silica Spheres In Micron Size Range, **26** (1), 62 (1968).

Chapter 6 Ammonia borane confined within porous silica and carbon for hydrogen storage

6.1. Introduction

The physical and chemical properties of hydrogen make it an important potential synthetic energy for our future economy and society. In order to utilize hydrogen for transportation, it becomes obvious that vehicular hydrogen storage needs drastic improvement to be practical. The Department of Energy (DOE) of the United States has set capacity benchmark levels of above 6.0 wt% and a volumetric density of 63 kg H_2 m^{-3} by the year 2010, and a target of 9 wt% hydrogen by 2015, under moderate pressure and temperature for an onboard hydrogen storage and delivery system. Moreover, the onboard hydrogen storage system needs to operate at an acceptable working efficiency and condition. To date, few materials meet the long-term gravimetric requirements and provide rapid hydrogen release at a temperature between -20 and 85°C. Thus it is very important to explore new materials that have light weight and can store a high percentage of hydrogen with desirable delivery characteristics.

Hydrogen storage materials that release H_2 by chemical thermolysis without producing by-products or contaminants are a promising option. One material which has attracted much attention is ammonia borane NH_3BH_3 (AB), owing to its remarkable stoichiometric hydrogen content (~19.6 wt %), moderate temperatures

for thermal decomposition, the exothermic nature of decomposition process, as well as the fact that it is thermally stable at ambient temperatures for store and transport. The thermal decomposition of solid AB includes the following three steps. (1)

$$NH_3BH_3 \rightarrow NH_2BH_2 + H_2 \quad <120℃ \qquad (1)$$

$$NH_2BH_2 \rightarrow NHBH + H_2 \quad >120℃ \qquad (2)$$

$$NHBH \rightarrow NB + H_2 \quad >500℃ \qquad (3)$$

The first and second reactions release 6.5 and 6.9 wt% of hydrogen below 200^{o}C, with the formation of polyaminobrane $(NH_2BH_2)_x$ and polyiminoborane $(NHBH)_x$, respectively. The third reaction can release 7.3 wt% of hydrogen. However, it is impractical for hydrogen fuel purpose because of the very high decomposition temperature (>500^{o}C). During the thermal decomposition process, besides hydrogen, highly volatile products, involving borazine ($N_3B_3H_6$), monomeric (BH_2NH_2) and ammonia (NH_3), are also generated with different heating rates. (2)

With both protic N-H and hydridic B-H bonds and a strong B-N bond, three H atoms per main group element, and a low molecular weight (30.7 g/mol), AB has the potential to meet the stringent gravimetric and volumetric hydrogen storage capacity targets needed for transportation applications. Although AB is a strong candidate for on-board hydrogen storage, there are still some obstacles limiting its practical application. The major challenges are the slow dehydrogenation kinetics;

irreversibility and formation of volatile materials (trace borazine and ammonia). (3) In order to eventually satisfy all of the economic and technical requirements for use as a sustainable energy source, the AB system has to be able to release most of the available hydrogen at an appropriate rate, must produce a minimum of volatile by-products. An economically viable method for the regeneration of AB will also have to be developed before it can be used at the commercial scale.

Recently, much attention has been received to solve these problems. Nanostructured materials have the great potential for hydrogen storage because of their unique features such as adsorption on the surface, inter- and intra- grain boundaries, and bulk absorption. Nanostructured and nanoscale materials strongly influence the thermodynamics and kinetics of hydrogen absorption and dissociation by decreasing the H_2 dessociation temperature, increasing the diffusion rate and decreasing the required diffusion length. (4,5) Additionally, the materials at the nanoscale offer the possibility of tailoring material parameters independently of their bulk counterparts.

Experimental results on nanoscaled AB systems have clearly demonstrated improvements in the reaction kinetics and/or thermodynamics of hydrogenation and dehydrogenation. As mentioned in the previous chapter, Autrey and co-workers (4) found that the kinetics of hydrogen release was significantly enhanced at low temperatures (50 ºC) for a hybrid material, ammonia borane infused in a nanoporous silica, hexagonally ordered mesoporous silica SBA-15, and that the hydrogen purity

is increased. There are two notable effects resulting from the nanostructure of AB in the SBA-15 scaffold. First, the temperature threshold for hydrogen release is much lower than the temperature threshold for neat AB. Second, the yield of the side product, borazine, is significantly lower than that from neat solid state AB. These findings opened a new approach to on-board hydrogen storage by combining hydrogen-rich materials with nanoscaffolds.

Carbon AB nanoconfinement also offers promising alternative due to a number of potential benefits, e.g. a percolated carbon network serves as a thermal conduction pathway, adjustable pore diameter provides size confinement for hydride particles, and the carbon framework provides the powder with required mechanical strength with minimal added weight. Feaver et al. (5) studied coherent carbon cryogel AB nanocomposites for hydrogen storage and found a hydrogen release reaction with an appreciable reduction in the dehydrogenation temperature to < 90 ºC as well as the suppression of borazine release. Particularly, as nano supports, the large pore size of 2 to 30 nm within the ordered mesoporous carbons are beneficial to mass transfer.

Recently, the release of hydrogen from AB by catalysis attracted much attention. In particular, catalysis of AB dehydrogenation by some metals (such as palladium and rhodium, (6-8) iridium, (9) cobalt and nickel (10-12)) presented notable improvements. Yao et al. (1) reported a new catalytic strategy using lithium and nanostructure confinement in mesoporous carbon (CMK-3) for the thermal

decomposition of AB. AB loaded on the 5% Li/CMK-3 framework released ~7 wt% of hydrogen at around 60 ºC, and entirely suppressed borazine and ammonia emissions that were harmful for proton exchange membrane fuel cells. The results suggest that the use of functional porous carbons with modified surface as scaffolds may enhance the properties of a solid state hydrogen storage material.

Despite the demonstrated effectiveness of concerted kinetic and thermodynamic improvements of the hydrides, the nano engineering approach is plagued by the capacity penalties imposed by the use of foreign scaffolds or metal catalysts. It will be desirable to directly synthesize porous carbons with functional surface that can enhance the hydrogen release behavior of AB, in the absence of impregnated catalysts. Moreover, the influences of the nanostructure parameters on the hydrogen release of AB, such as the pore diameters of the scaffolds, are not systematically reported. A deep understanding on the correlation between the hydrogen release behavior and the pore structure as well as wall composition of scaffolds will be important for the optimization of an AB/scaffold composite system for practical applications.

In this chapter, AB is encapsulated within two porous silica samples with tunable pore sizes and one N-doped porous carbon. The hydrogen release behaviour of AB in the three AB/scaffold systems is further investigated.

6.2 Experimental

6.2.1 Synthesis

Chemicals:

Chemicals including ammonia borane (assay 97%) and methanol (99%) were purchased from SIGMA-ALDRICH and were used as received without further purification.

Synthesis:

Encapsulation of AB within nanostructured frameworks such as porous silica and carbon materials has been prepared using a wet impregnation approach. Nanostructured scaffolds are the materials prepared in our previous work, including silica-1 from chapter 3, which has a helical structure and a pore diameter of 1.8 nm; silica 2 from chapter 4, which is the vesicular structure with a pore diameter of 18 nm, and a porous carbon from chapter 5, which was obtained using 320 nm silica particles as hard templates.

For a typical AB impregnation process, 500 mg AB was dissolved in 5 ml methanol and the same amount of nanoscaffold material was added to the solution under stirring. The methanolic solution appeared to fill the internal channels and open-window porous scaffold through a capillary action. The solvent were removed under vacuum to obtain the solid AB/nanoscaffold materials with an internal coating of

ammonia borane. After the AB impregnation process, the samples were named as AB/Silica-1, AB/Silica-2, and AB/Carbon, respectively.

6.2.2 Characterization

The impregnated samples were characterized by nitrogen absorption-desorption isotherms. The thermal analysis was determined by temperature programmed decomposition using a RGA MS system. All thermal analyses were made from room temperature to 300°C at a heating rate of 1 °C/min under Argon gas flow and the signal response is 3s. The surface chemistry of samples was determined with a Kratos Axis ULTRA X-ray Photoelectron Spectrometer (XPS) incorporating a 165mm hemispherical electron energy analyser. The incident radiation was Monochromatic Al Kα X-rays (1486.6eV) at 150W (15kV, 10ma) and at 45 degrees to the sample surface. Photoelectron data was collected at a take-off angle of theta = 90^{o}. Survey (wide) scans were taken at an analyser pass energy of 160eV and multiplex (narrow) high resolution scans at 20eV. Survey scans were carried out over 1200-0eV binding energy range with 1.0eV steps and a dwell time of 100ms. Narrow high-resolution scans were run with 0.05ev steps and 250ms dwell time. Base pressure in the analysis chamber was $1.0x10^{-9}$ torr and during sample analysis $1.0x10^{-8}$ torr. Atomic concentrations were calculated using the CasaXPS version 2.3.14 software and a linear baseline with Kratos library Relative Sensitivity Factors (RSFs).

6.3 Results and discussion

6.3.1 Nitrogen sorption isotherms

Nitrogen sorption isotherms of mesoporous Silica-1 and Silica-2 before and after loaded with AB are presented in Figure 6.1. Mesoporous Silica-1 has a BET surface area of 573 m^2/g and a pore volume of 0.46 cm^3/g (see Table 6.1). However, after loading with AB, the AB/Silica-1 composite has a much decreased BET surface area of 21 m^2/g and a very low pore volume of 0.032 cm^3/g. The surface area and pore volume for mesoporous Silica-2 are 321 and 1.12 cm^3/g, respectively, which also decrease to 53 m^2/g and 0.143 cm^3/g for the AB/Silica-2. It is concluded that after loaded with AB, the surface area and pore volume are greatly reduced in both silica samples.

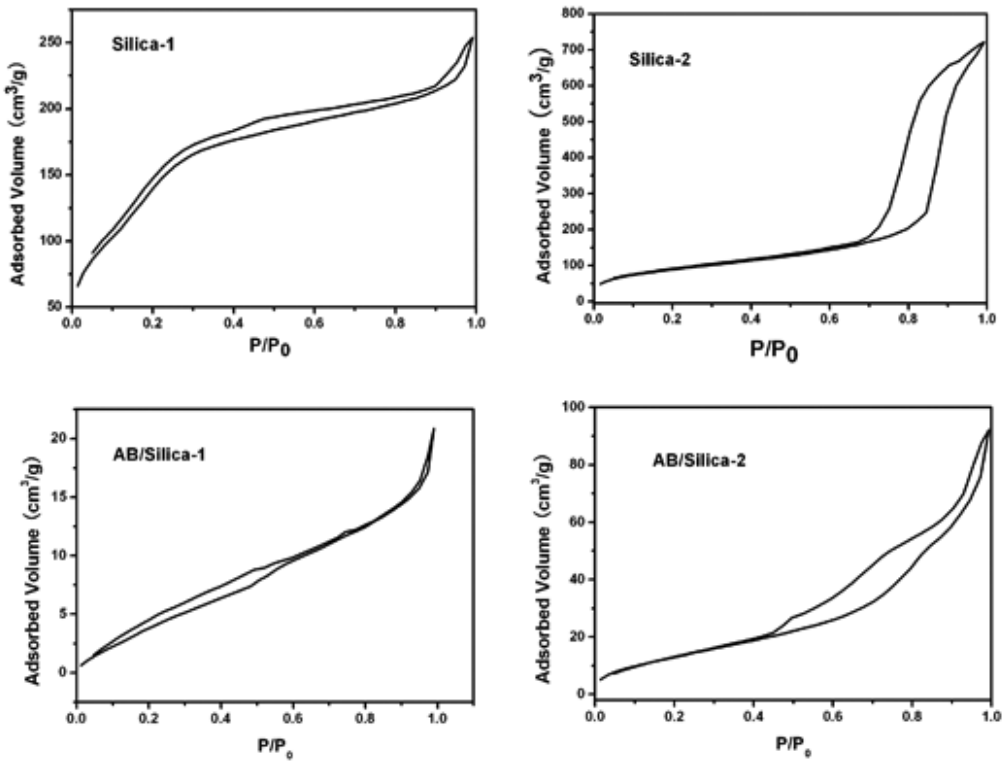

Figure 6.1 Nitrogen sorption isotherms of Silica-1 and Silica-2 before and after AB loading

Table 6.1 Physicochemical property of silica and carbon before and after AB loading

Sample ID	Pore size (nm)	Surface area (m^2/g)	Pore volume (cm^3/g)
Silica-1	1.8	573	0.46
AB/Silica-1	1.8	21	0.032
Silica-2	18	321	1.12
AB/Silica-2	8.0	53	0.14
Carbon	-	355	0.92
AB/Carbon	-	47	0.043

The pore size distribution curves of both silica samples before and after loading with AB are shown in Figure 6.2. It is shown that after impregnation of AB, although the pore volume is greatly decreased in both samples, the pore size is almost the same for AB/Silica-1 compared with the pure silica sample before loading, indicating that at least part of the pores in silica-1 were not impregnated with AB, probably due to its ultrasmall pore size and inhomogeneous distribution of AB. On the contrary, the pore size of AB/Silica-2 is decreased from 18 nm in pure silica sample to 8 nm. The shrinkage of the pore size in AB/Silica-2 can be regarded as another support for the loading of AB into nanopores.

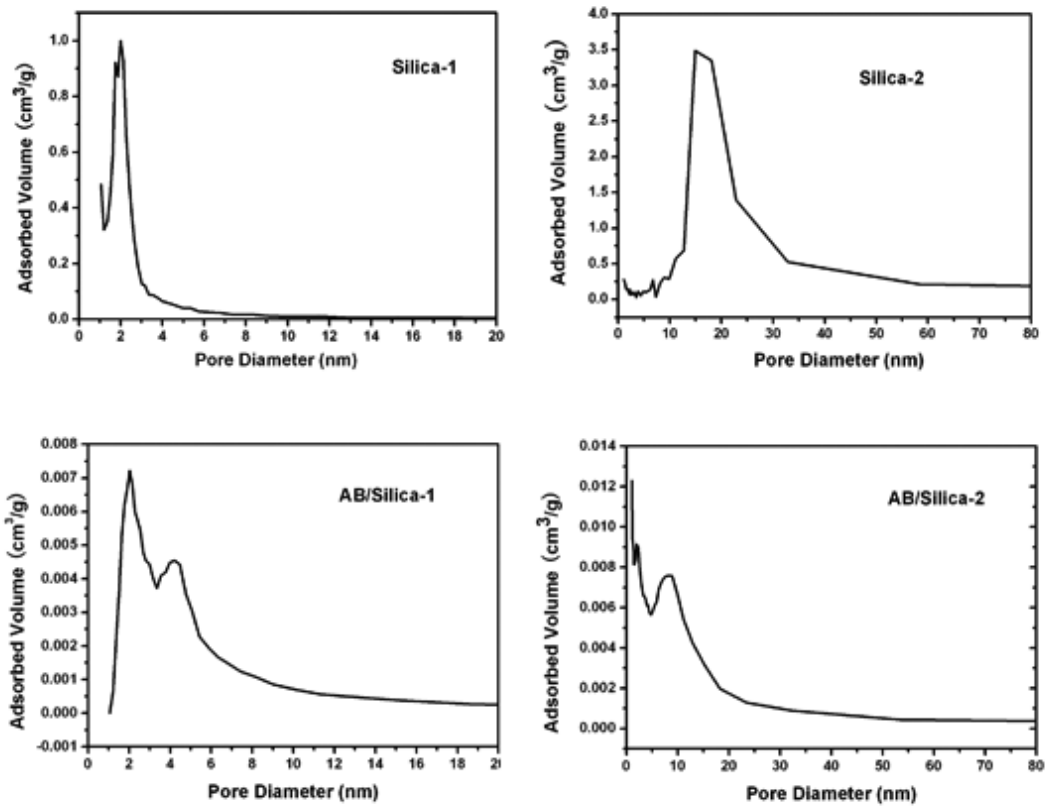

Figure 6.2 Pore size distribution curves of Silica-1 and Silica-2 before and after loading with AB

Nitrogen sorption isotherms of porous carbon before and after loaded with AB are presented in Figure 6.3. In the case of porous carbon, the BET surface area and pore volume are decreased from 355 m^2/g and 0.92 cm^3/g (before loading) to 47 m^2/g and 0.043 cm^3/g (after loading), respectively. The large pore should be impregnated with AB as the capillary condensation step at high relatively pressure is not observed. For a direct comparison, the pore size, pore volume and surface area of mesoporous Silica-1 and Silica-2 as well as porous carbon before and after loading with AB are listed in Table 6.1.

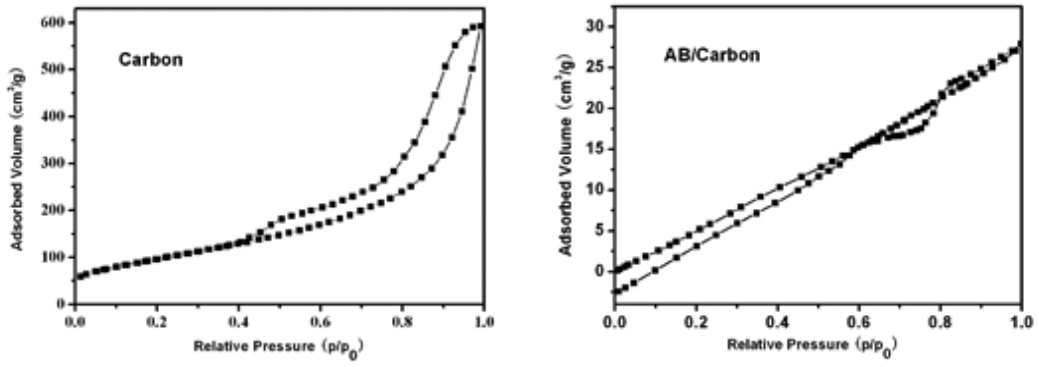

Figure 6.3 Nitrogen sorption isotherms of porous carbon before and after loading with AB

6.3.2 X-ray photoelectron spectroscopy

The surface properties of AB/nanocomposites were further investigated by X-ray photoelectron spectroscopy (XPS). Figure 6.4 shows the B 1s XPS results of AB /Silica-2 and AB/carbon. The peaks at 187.8 eV and 190.8 eV in the XPS pattern are attributed to B-H and B-O bonds, respectively. The formations of B-O bonds suggest the interaction of AB with the Si-OH group at the surface. In the case of AB/carbon system, the O is from the OH group located at the surface of carbon due to the synthesis procedure. Comparing AB/Silica-2 and AB/Carbon materials, it is shown the relative peak intensity of B-O versus B-H is much higher in AB/Silica-2, suggesting that OH group density is much less in the case of AB/Carbon material.

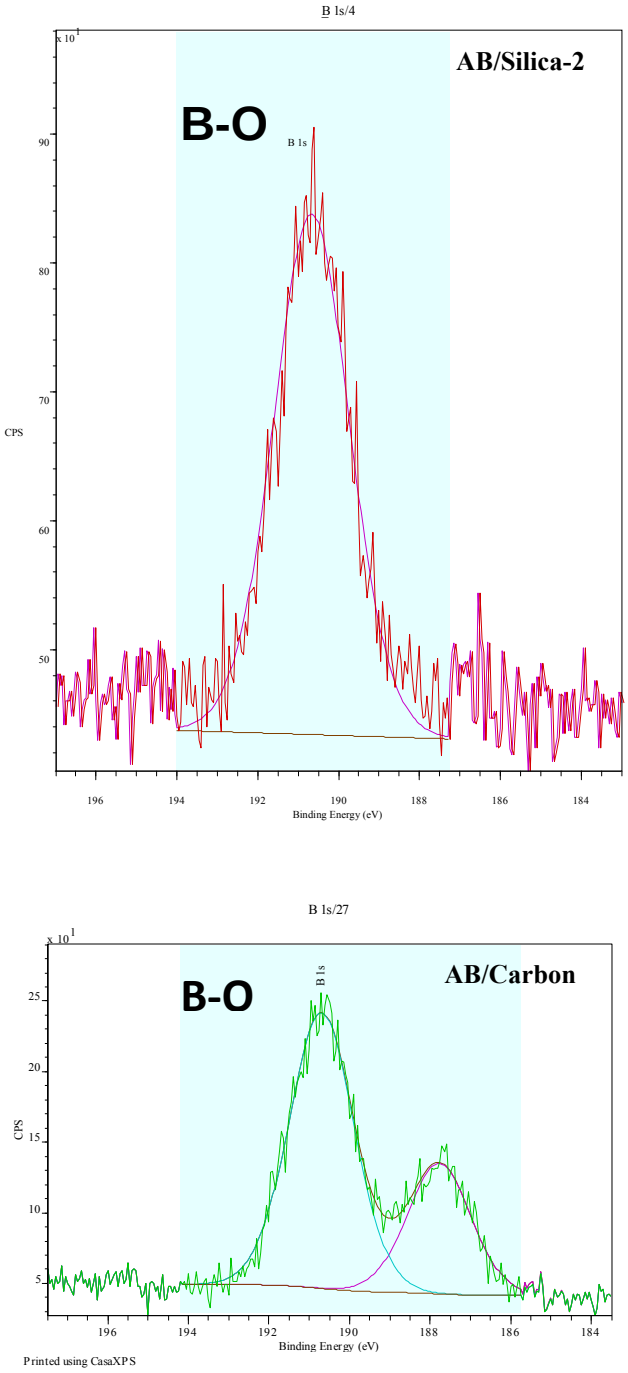

Figure 6.4 The B 1s XPS results of AB/Silica-2 and AB/Carbon

6.3.3 Thermal decomposition performance

The thermal decomposition performances of AB, AB/Silica-1 and AB/Silica-2 (two silicas with the same composition but different pore sizes), and AB/Carbon, have

been measured by thermogravimetry (TG) combined with mass spectroscopy. The TG curve of AB loaded in Silica-1 is measured and shown in Figure 6.5. For comparison, the TG curve of neat AB is also shown in this figure. Below 150 °C, the weight loss from neat AB is 29.12% and AB/Silica-1 is 30.23%. This is much larger than the theoretical hydrogen release capacity in neat AB via two steps of reaction, which is 13.4 wt% in total. This observation can be attributed to the formation of volatile products other than hydrogen gas from AB. Moreover, it can be seen that AB loaded in Silica-1 has a similar decomposition behavior to that of neat AB. This is in accordance with the nitrogen sorption analysis results. As Silica-1 has a small mean pore diameter of 1.8 nm, it is very likely that only very limited amount of AB entered the nanopores. Most of the AB that is associated with the silica particles must be deposited on the surface thus showing a similar decomposition behavior to that of neat AB. This result suggests that nanoporous silica with small pore diameters is not a good candidate for loading AB.

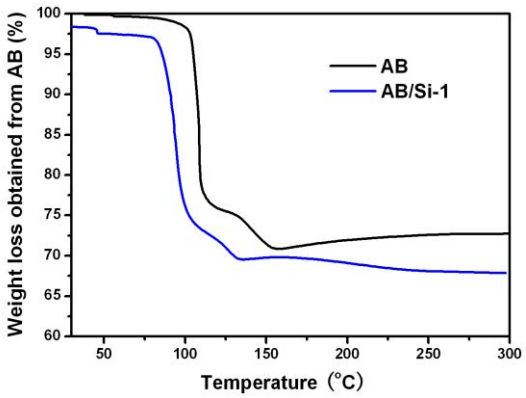

Figure 6.5 Thermogravimetric results of neat AB and AB/Silica-1

The TG curve of AB loaded in Silica-2 is shown in Figure 6.6. It is seen different from that for AB/Silica-1, the weight loss from AB/Silica-2 is ~ 20% below 150 °C, much smaller than that from neat AB and AB/Silica-1. Importantly, the decomposition behavior can be seen to be very different from that of neat AB. To understand clearly, the products of the decomposition were sent to a mass spectroscopy for analysis. The mass spectra of the products are shown in Figure 6.7. The figure shows that, below 150 °C, the main release product is hydrogen with a small amount of ammonia while the release of borazine cannot be detected from our measurement. The release of ammonia explains the observation that the weight loss from AB/Silica-2, which is ~ 20%, is higher than the theoretical amount of hydrogen that can be released from AB, which is ~ 13.4%.

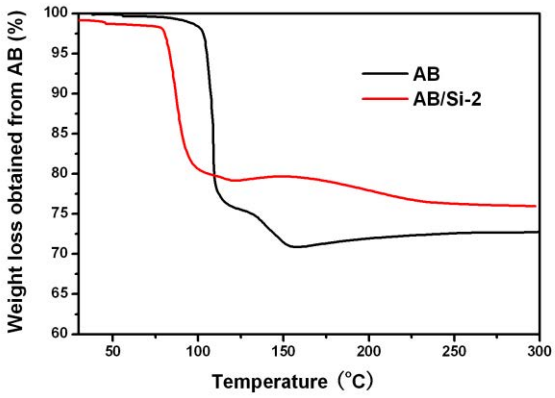

Figure 6.6 Thermogravimetric results of neat AB and AB/Silica-2

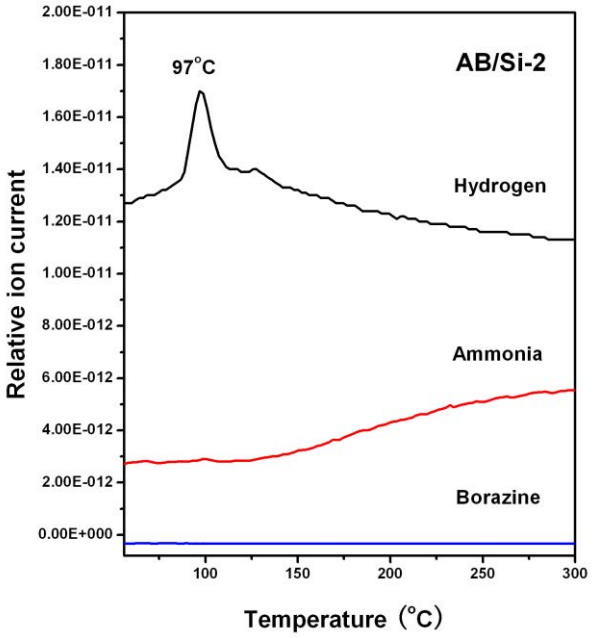

Figure 6.7 The MS result of AB/Silica-2

Figure 6.8 compares the hydrogen release behavior from neat AB and AB/Silica-2. It can be seen that neat AB starts to decompose at above 100°C and has two release peaks at around 110°C and 150°C, respectively. This is consistent with results from literature.(4) Compared with neat AB, the decomposition of AB loaded in nanostructured Silica-2 shows an almost one-step process for the release of hydrogen, the second peak at relatively higher temperature is greatly reduced. Moreover, compared with neat AB, AB/Silica-2 releases hydrogen at a lower temperature with a desorption peak at 97 °C, almost 13 °C lower compared to neat AB. It is also noted that compared with neat AB, the release of ammonia is greatly suppressed,(1) although a little amount of ammonia is still detected (Figure 6.7).

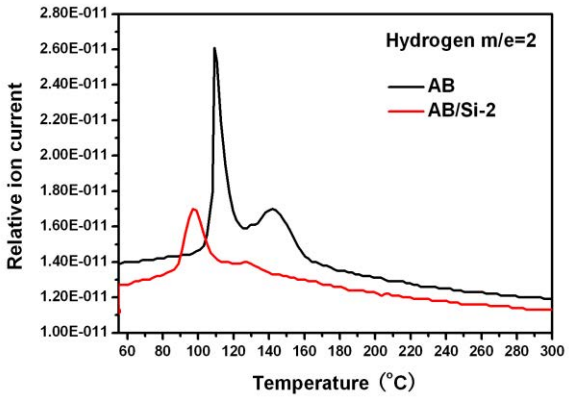

Figure 6.8 The MS results of neat AB and AB/Silica-2

The products released from AB loaded in the porous carbon material are shown in Figure 6.9. The mass spectra suggest that neither ammonia nor borazine can be detected, indicating that the unnecessary byproducts from AB decomposition has been totally suppressed. It is noted that when AB is loaded in a mesoporous carbon, CMK-3, the release of ammonia and borazine was detected as reported in a previous literature,(1) showing the advantage of N-doped carbon composition in our material. The release of hydrogen appears with the first desorption peak at 90 °C, about 20 °C lower than that of neat AB. From Figure 6.9, the total amount of hydrogen released is measured to be 6 wt%.

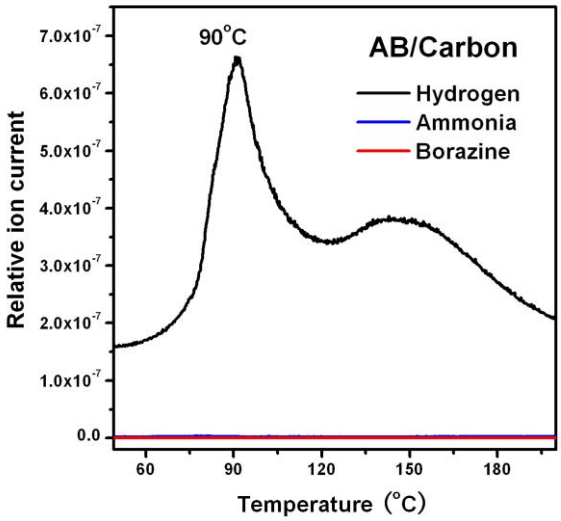

Figure 6.9 The MS result of AB/Carbon

6.4 Conclusions

In this chapter, the hydrogen release behaviour of AB encapsulated within two porous silicas with tunable pore sizes and one N-doped porous carbon has been studied. In the case of porous silicas as nanoscaffolds, when the pore diameter is too small, such as 1.8 nm (Silica-1), AB cannot be efficiently impregnated into the nanopores and the thermal decomposition of AB is associated with the formation of volatile by-products. In the case of a large pore Silica-2 (18 nm), it is a relatively better candidate compared to Silica-1 with small pore because the formation of most by-products is suppressed and the first hydrogen desorption peak is lowered by 13 °C compared to neat AB. However, a small amount of released ammonia is still observed, thus Silica-2 is not an ideal candidate. In the case of a macroporous N-doped carbon material, the total amount of hydrogen released is 6 wt%, while the formation of both ammonia and borazine are suppressed. More importantly, the first

release peak of hydrogen is 90 °C, about 20 °C lower than that of neat AB, which is better than a pure carbon material CMK-3 and equivalent to a Li-CMK-3 material.(1) Our results have shown that in addition to the influence of pore size, the composition of the host material is another important factor. It is anticipated that highly porous N-doped carbon materials with further optimized pore parameters will be ideal candidates for AB immobilization and hydrogen storage.

References

1 L. Li, X. Yao, C. H. Sun, A. J. Du, L. N. Cheng, Z. H. Zhu, C. Z. Yu, J. Zou, S. C. Smith, P. Wang, H. M. Cheng, R. L. Frost, and G. Q. M. Lu, *Advanced Functional Materials,* Lithium-Catalyzed Dehydrogenation of Ammonia Borane within Mesoporous Carbon Framework for Chemical Hydrogen Storage, **19** (2), 265 (2009).

2 F. Baitalow, J. Baumann, G. Wolf, K. Jaenicke-Rossler, and G. Leitner, *Thermochimica Acta,* Thermal decomposition of B-N-H compounds investigated by using combined thermoanalytical methods, **391** (1-2), 159 (2002).

3 T. B. Marder, *Angewandte Chemie-International Edition,* Will we soon be fueling our automobiles with ammonia-borane?, **46** (43), 8116 (2007).

4 A. Gutowska, L. Y. Li, Y. S. Shin, C. M. M. Wang, X. H. S. Li, J. C. Linehan, R. S. Smith, B. D. Kay, B. Schmid, W. Shaw, M. Gutowski, and T. Autrey, *Angewandte Chemie-International Edition,* Nanoscaffold mediates hydrogen release and the reactivity of ammonia borane, **44** (23), 3578 (2005).

5 A. Feaver, S. Sepehri, P. Shamberger, A. Stowe, T. Autrey, and G. Z. Cao, *Journal of Physical Chemistry B,* Coherent carbon cryogel-ammonia borane nanocomposites for H-2 storage, **111** (26), 7469 (2007).

6 C. A. Jaska, K. Temple, A. J. Lough, and I. Manners, *Journal Of The American Chemical Society,* Transition metal-catalyzed formation of boron-nitrogen bonds: Catalytic dehydrocoupling of amine-borane adducts to form aminoboranes and borazines, **125** (31), 9424 (2003).

7 C. A. Jaska and I. Manners, *Journal Of The American Chemical Society,* Heterogeneous or homogeneous catalysis? Mechanistic studies of the rhodium-catalyzed dehydrocoupling of amine-borane and phosphine-borane adducts, **126** (31), 9776 (2004).

8 T. J. Clark, K. Lee, and I. Manners, *Chemistry-A European Journal,* Transition-metal-catalyzed dehydrocoupling: A convenient route to bonds between main-group elements, **12** (34), 8634 (2006).

9 M. C. Denney, V. Pons, T. J. Hebden, D. M. Heinekey, and K. I. Goldberg, *Journal Of The American Chemical Society,* Efficient catalysis of ammonia borane dehydrogenation, **128** (37), 12048 (2006).

10 Q. Xu and M. Chandra, *Journal Of Power Sources,* Catalytic activities of non-noble metals for hydrogen generation from aqueous ammonia-borane at room temperature, **163** (1), 364 (2006).

11 T. Umegaki, J. M. Yan, X. B. Zhang, H. Shioyama, N. Kuriyama, and Q. Xu, *Journal Of Power Sources,* Hollow Ni-SiO2 nanosphere-catalyzed hydrolytic dehydrogenation of ammonia borane for chemical hydrogen storage, **191** (2), 209 (2009).

12 R. J. Keaton, J. M. Blacquiere, and R. T. Baker, *Journal Of The American Chemical Society,* Base metal catalyzed dehydrogenation of ammonia-borane for chemical hydrogen storage, **129** (7), 1844 (2007).

Chapter 7 Conclusions and Recommendations

7.1 Conclusions

Several strategies have been developed to synthesize porous silica and carbon materials with controlled pore size and composition as new candidates for hydrogen storage.

Firstly, a facile but effective method to synthesize helical mesostructures with small pore size and adjustable pitch size has been developed. The influence of trifluoroacetic acid, acetic acid and their salts in the synthesis of helical mesoporous materials has been systematically investigated. Helical mesostructures have been successfully obtained when CF_3COO^- anions are used as additives with an additive/CTAB molar ratios range of 0.1-0.375 for the CF_3COOH/CTAB templating system and a relatively wider molar ratio of additive/CTAB 0.1-0.5 for the CF_3COONa/CTAB system. The pitch sizes of the helical mesostructures can be finely controlled by varying the additive/CTAB ratios. Our results further indicate that in order to synthesize helical mesostructures in a wide synthesis window, i.e. a wider range of additive/CTAB ratios, the perfluorinated salt with a short fluorocarbon chain is necessary.

Secondly, an approach to synthesize large pore siliceous materials with desired structures and pore diameters through the addition of TMB has been explored. It is demonstrated that a change in the TMB addition time to a nonionic block copolymer templating system can cause a phase transformation from multilamellar vesicles to an ordered hexagonal mesostructure. While previously TMB was used to facilitate the formation of a microemulsion template or as a swelling agent for mesostructured materials, it is used in our work as an agent to change the packing parameter of cooperatively self-assembled mesostructured or vesicular materials. A significant implication of our work is that, through simple manipulation of the addition sequence as well as the addition time of organic cosolvents, the self-assembly processes can be tuned among microemulsion templating, cooperative vesicular templating and cooperative liquid crystal templating, from which complex inorganic materials with controlled and tunable pore structures can be obtained with the same synthesis system. This finding may pave the way for a simple approach to the synthesis of versatile porous materials with different structures, which have potential applications in catalysis, immobilization and controlled release of large biomolecules.

Thirdly, the classical Stöber method has been adopted to prepare silica spheres with controlled particle size, which are then used as the templates to synthesize macroporous carbon materials with large and open pore space. Meanwhile, melamine formaldehyde resin has been introduced as a nitrogen containing carbon precursor to adjust the surface chemistry in the final products. The obtained porous carbon

materials in our work show high specific surface areas and pore volume, large pore size, and moderate content of nitrogen.

Finally, the influence of pore structure and composition of nanoporous materials on the hydrogen release behavior of AB being loaded in the nanoporous scaffolds has been studied. It is shown that in the case of a small pore (~ 2 nm), AB cannot be efficiently impregnated into the pore channels, and the thermal decomposition of AB is associated with the formation of volatile by-products. In the case of a large pore Silica-2 (18 nm), it is a relatively better candidate compared to the small pore silica because the formation of most by-products is suppressed and the first hydrogen desorption peak is lowered by 13 °C compared to neat AB. However, a small amount of released ammonia is still observed. In the case of a macroporous N-doped carbon material, the total amount of hydrogen released is 6 wt%, while the formation of both ammonia and borazine are suppressed. More importantly, the first release peak of hydrogen is 90 °C, about 20 °C lower than that of neat AB, which is better than pure carbon material and equivalent to a Li-CMK-3 material. Our results show that in addition to the influence of pore size, the composition of the host material is another important factor. It is anticipated that highly porous N-doped carbon materials with further optimized pore parameters will be ideal candidates for AB immobilization and hydrogen storage.

7.2 Recommendations

Through this systematic study, several new methods have been developed to finely tune the morphology, pore structure and wall composition of nanoporous materials. More importantly, I have arrived at several important conclusions concerning the influence of the pore diameter and wall composition of nanoporous materials on the thermal decomposition behavior of AB confined in nanoporous scaffolds. However, due to the time limit of this research, there are several imperfect aspects that should be further improved. Recommendations for the improvements based on the current project as well as potential directions for improving understanding or extending the applications of the nanostructure confined AB system are outlined below.

1. The observation that N-doped macroporous carbon can improve the thermal decomposition performance of AB appears very promising and implies a new mechanism, which needs further investigation. A reasonable comparison could be made among a series of carbon materials with the same pore architectures, but controlled N content, as well as silica porous materials with the same macroporous structure.

2. It will be interesting to investigate the performance of hydrogen release of AB confined in porous N-doped carbon materials with systematically tunable pore sizes, especially in the mesopore range. In my experiments, I used the surfactant

templating approach to synthesize mesoporous N-doped carbon, but failed. Other approaches should be designed to obtain such a nanoporous substrate to obtain optimized hydrogen release performance.

3. Other structure parameters, such as the particle size, pore topology, pore volume as well as surface properties should be systematically manipulated and studied for their influence on the AB loading and subsequent thermal decomposition behaviors.